UNIVERSITY OF OKLAHOMA

GRADUATE COLLEGE

ROLLING-TYPE ISOLATION: AN EXPERIMENTAL CHARACTERIZATION AND NUMERICAL PARAMETRIC STUDY

A THESIS

SUBMITTED TO THE GRADUATE FACULTY

in partial fulfillment of the requirements for the

Degree of

MASTER OF SCIENCE

By

COREY D. CASEY
Norman, Oklahoma
2017

ROLLING-TYPE ISOLATION: AN EXPERIMENTAL CHARACTERIZATION AND NUMERICAL PARAMETRIC STUDY

A THESIS APPROVED FOR THE
SCHOOL OF CIVIL ENGINEERING AND ENVIRONMENTAL SCIENCE

BY

Dr. P. S. Harvey Jr., Chair

Dr. J.-S. Pei

Dr. R. W. Floyd

To my loving parents and siblings who are so much responsible for any success of my own. You have encouraged and supported me in my many endeavours throughout the years. Thank you for always believing in me. To my mother who taught me how to learn for the first twelve years of my schooling and to my father who taught me to work hard and be committed to a goal.

Acknowledgements

I want to first thank Dr. Wei Song of the Department of Civil, Construction and Environmental Engineering at the University of Alabama. This work would not have been possible without his expertise, as well as allowing us to use the equipment and shake table at the Large Scale Structures Laboratory. I would also like to thank Collin Sewell for overseeing the testing in the Large Scale Structures Laboratory, and Blair M. Butler and Kenneth J. Aldrich for help with data collection.

I also want to thank Don Hubbard of WorkSafe Technologies, Inc. for providing the ISO-Base units and Robert Sotelo (WorkSafe) for assisting with assembly of the ISO-Base units. I would also like to Roger Segroves of Panduit Corporation for providing the server cabinets that were tested. Don and Roger's input on the typical operating conditions of these systems is gratefully acknowledge.

I want to thank the National Science Foundation for their partial sponsorship of this work. This material is based upon work partially supported by the National Science Foundation under Grant No. NSF-CMMI-1663376. Any opinions, findings, and conclusions or recommendations expressed in this material are those of the authors and do not necessarily reflect the views of the National Science Foundation.

Additionally, I would like to thank my committee members, Dr. Jin-Song Pei and Dr. Royce W. Floyd, for their willingness to serve on my committee. They have challenged me and helped me to grow personally and professionally.

Finally, I would like to thank my Advisor, Dr. P. Scott Harvey. His mentorship has

helped me grow as a student, an engineer, and a person. His door has always been open for me to come in and ask questions and to learn more about any and everything. The opportunity to work with Dr. Harvey has been a wonderful experience.

Contents

List of Figures

List of Tables

Abstract

Building contents and nonstructural components are known to be vulnerable during seismic events. Of particular concern is computer and network equipment that is critical in the post-earthquake recovery process. A solution for mitigating the seismic hazard to such systems is rolling-type isolation systems (RISs), but the characterization of RISs with realistic loading conditions and system setups is not well documented. An experimental parametric case study was performed varying the mass eccentricity, the number of cabinets, and the damping to simulate in-service conditions. A series of free response tests was performed using an abrupt shake table displacement (pulse) along with forced response tests utilizing the VERTEQ-II Zone-4 waveform. An array or string potentiometers and accelerometers measured the longitudinal, transverse, and rotational responses of the systems. Supplementally damped systems were found to have increased rotations when a mass eccentricity was present. The increase in system size and mass reduced the overall rotations due to an increased restoring moment arm and higher mass moment of inertia. Increased damping decreased the displacement demand on the isolator but increased the overall accelerations slightly. However, the systems without the supplemental damping had such large displacements that impacts were experienced causing excessively high accelerations. Durability was an issue for lightly damped systems due to increased contact stress between the ball and concave rolling surface.

A physics-based mathematical model was developed for the prediction of the re-

sponse of multi-unit RIS arrays with mass eccentricity. The model was first calibrated to the experimental free response tests and then validated with the forced response tests. The validated model was then used to perform a numerical parametric case study. Configurations with one, two, four and eight cabinets were modeled, and the eccentricity was varied. The VERTEQ-II waveform was applied in both the front-to-back and side-to-side directions under varying ground motion scaling. Impacts are predicted at lower ground motion scaling with larger mass eccentricity due to the initiation of rotations. The ground motion scaling for which impacts occur is increased due to the systems higher resistance to rotations from increased number of isolated cabinets. Finally, capacity design curves for the impact point were determined, which can be used to establish the required configuration (number of cabinets and eccentricity) for a given ground motion intensity.

Chapter 1

Introduction

1.1 Overview

Degradation of human well-being through loss of life and economic impact associated with past major seismic events is well documented. Over the past century, advances in building science related to structural resilience have brought about an era of construction where buildings are less vulnerable to the effects of seismic excitations (Chopra, 2012). A growing concern, however, is that of nonstructural components such as system critical lifelines, emergency response communications, and utility backup systems. These systems can vary widely in size, functionality, and structural housing making it difficult to produce design guidelines that can fully protect such equipment. A rapidly expanding solution has been that of component isolation, similar to structural isolation. Rolling-type isolation platforms have a wide array of applications due to their simple implementation and low profile which contains the ability to isolate in any horizontal direction without the need for springs in the orthogonal directions and the ease of incorporating supplemental damping through treatment of the rolling surfaces. Despite the advantages of rolling isolation, there is a dearth of experimental characterization tests or analytical models for real world systems under typical operating conditions taking into consideration mass eccentricity, increased platform size and system mass, or systems containing supplemental damping.

1.2 Motivation

In 1994, a magnitude (M) 6.7 earthquake hit the metropolitan area of Los Angeles, California resulting in 33 causalities, 7000 injured, 20000 homeless, and $20 billion of damage (Merriman and Williams, 1994). Despite the Northridge earthquake being a moderately sized earthquake, it is the fifth costliest natural disaster in United States (U.S.) history. Seismic events all around the world have resulted in loss of life and high economic damage. A 2008 Federal Emergency Management Agency (FEMA) report estimated the yearly economic damage in the U.S. alone to be $5.3 billion with the majority of the risk being in the states of California, Oregon, Washington, Hawaii, and Alaska (FEMA, 2008). The risk associated with a major earthquake easily reaches the hundreds of billion dollar range for high seismic metropolitan areas on the west coast such as Los Angeles, San Francisco, and Seattle, but also for low seismic metropolitan areas on the east coast such as New Jersey and New York.

The enormous risk associated with earthquakes is well documented and, because of this, much research has gone into determining earthquake behavior and how to mitigate the extreme hazards that they pose. The seismic response of any structure or component of a structure begins with soil behavior, then moves into soil-structure mechanics, and finally into structural dynamics. Many sources exist on each of these topics, quantitatively defining results and qualitatively defining general behavior (Boulanger et al., 1999; Irwin and Barnes, 1975; Tena-Colunga and Abrams, 1996; Légeron et al., 2005). Despite extensive research into behavior and mitigation of seismic hazards, the fact remains that earthquakes are unpredictable and the ground and structure motions that result are highly nonlinear through the continuum of the soil, soil-structure interface, and the structure itself.

Methods stemming from research and practice proven design have been implemented into design codes such as ASCE 7 (ASCE, 2010) and Eurocode 8 (European

Committee for Standardization, 2004) that have produced many modern buildings in the U.S., Europe, and other developed regions around the world that can withstand seismic loads that would otherwise result in collapse and loss of human life. However, a growing concern in the field of seismic mitigation is that of nonstructural components and the difficulty of evaluating such systems within structures due to complex dynamics from the coupling with the superstructure (Singh et al., 2006a,b). Figure 1.1 shows damage sustained to nonstructural components during the Northridge earthquake. Case studies on the performance of medical facilities during the 1994 Northridge, 1995 Kobe, and the 1999 Chi-Chi earthquakes showed that failure of nonstructural components had drastic effects on the emergency response of these facilities (Filiatrault and Sullivan, 2014; Cimellaro et al., 2010). A case study on the performance of nonstructural components during the Northridge earthquake showed that many buildings suffered from extensive damage to heating, ventilation, and air conditioning (HVAC) systems such as diffusers and duct work (McKevitt et al., 1995). The study also revealed that buildings with shelving units had much of their contents fall which potentially caused further injury and delays in response time. Finally, the study documented the damage to electrical systems, in particular, failure of ceramic components (which are very brittle) within transmission stations. In addition to inhibiting hospital response during the Kobe earthquake, enormous economic loss was incurred through port systems including crane and utility line damage (Chang, 2000). Similarly, the San Fernando earthquake of 1971 caused extensive damage to many structures and nonstructural components (Jennings and Housner, 1973). Notably, four hospitals were rendered useless in the emergency response as well as destruction of major electrical transmission equipment.

Various case studies show that the contents of buildings, often times, are major contributors to the damage sustained during earthquakes and key factors in the recover process following seismic events. Building contents can also be high value assets that

Figure 1.1: Examples of nonstructural damage: (a) toppling book cases and (b) damage to gas canisters. Source: McKevitt et al. (1995).

need to be protected despite their little importance to the structure and occupants during and after a seismic event. Some typical building contents and nonstructural components are shown in Figure 1.2. Typical hospitals carts [Figure 1.2(a)] have been shown to be hazardous during seismic events due to their placement in corridors and patient rooms (Shi et al., 2014; Furukawa et al., 2013). Shelving systems [Figure 1.2(b)] can often withstand overturning forces of seismic excitations, but commonly loose their contents and can cause injury during the event and inhibit movement after an event. Valuable assets such as artwork [Figure 1.2(c)] are often vulnerable to damage due to fragile materials. Finally, network equipment [Figure 1.2(d)] often carries valuable data and communication devices which must be protected and maintain functionality during and after an event.

(a)

https://dir.indiamart.com/impcat/crash-cart.html

(b)

https://www.shelving.com/
Teardrop-Pallet-Rack-Starter-Units-p/ir3su36144-p.htm

(c)

https://quatr.us/greeks/
classical-sculpture-ancient-greece.htm

(d)

https://www.cdw.com/shop/products/
PANDUIT-NET-ACCESS-N-TYPE-CABINETS/2898087.aspx

Figure 1.2: Vulnerable building contents: (a) hospital equipment, (b) warehouse shelving, (c) valuable artwork, and (d) network cabinet.

An area not typically evaluated for earthquake hazard is that of major network and computer systems. These systems are often critical for lifeline support and facility communications that must be running during and after catastrophic events (Iwan, 1978; Notohardjono et al., 2004; Gavin and Zaicenco, 2007). Many of these systems, notably computer hard-drives, are extremely sensitive to accelerations, especially those experienced during seismic events (Alhan and Sahin, 2011).

An effective strategy for protecting structures and equipment from major earthquakes is *seismic isolation*. Isolation is the decoupling of an object from a harsh base motion, such as a structure from an earthquake ground motion or a piece of equipment from a resulting floor motion (Figure 1.3). Isolation is the basic concept of shifting

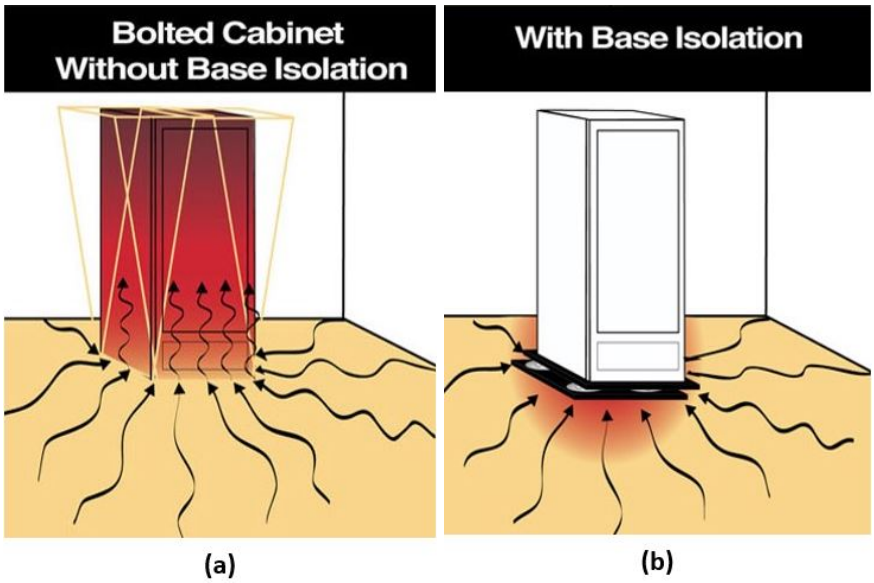

Figure 1.3: Component isolation: (a) Network cabinet without isolation and (b) network cabinet with isolation. Source: WorkSafe Technologies, Inc. (Valencia, CA).

the natural frequency of the structure/component away from the dominate forcing frequency of the earthquake/floor in order to reduce the isolated object's total acceleration response.

Within an isolation system, three primary characteristics contribute to the response: displacement capacity, stiffness, and damping. In perfect isolation, the structure is entirely decoupled from the ground motion and hence does not assume any accelerational response. In order for this to be achieved, the first characteristic, the *displacement capacity* of the isolation bearings, must be at least as high as that of the total ground displacement. Perfect isolation, however, is not feasible in practice due to coupling through stiffness and damping. Additionally, the demand that would be placed on the isolation bearings themselves would be extreme with strong overturning moments and high contact stresses, as well as residual displacement following the ground motion. For this reason, the second characteristic, *stiffness*, is typically included in an isolation system to limit the relative displacement of the structure with respect to the ground or from the equipment with respect to the floor. This inevitably creates some motion relative to

an inertial reference frame. These inertial effects can be damaging and lead to yielding of the structure, loss of operation to components, and adverse occupancy comfort. In order to remove energy from the system, the third characteristic, *damping*, is used as a dissipation mechanism. Effective isolation is a balancing act between these three primary characteristics. The following section will review common isolation systems and the implementation of the three primary characteristics.

1.3 Background

1.3.1 Historic Context

Isolation systems, and in particular, rolling-type isolation systems (RISs), date back to 1870 when Touaillon (1870) filed for a US Patent with the unique idea of setting a building on balls placed in upper and lower bowl-shaped plates that attach to the superstructure and foundation, respectively. The rolling action of the balls allows for the decoupling of the superstructure from the ground motion. Gravity provides the restoring force to recenter the balls in the bowl-shaped surfaces. Seiler (1907) proposed a rolling system for the foundation of a building containing balls inside cylindrical metal casings and received a US Patent. The balls roll on flat (no slope) metal plates which attach to the stone foundation and the superstructure. A US Patent was also issued to Schär (1910) who has a very similar concept as that of Touaillon, but utilizes concave upper and lower rolling surfaces made of cast concrete and includes metal balls to provide the rolling action. Bakker (1933) was granted a US Patent for his design which contains concave surfaces similar to Touaillon, but also includes a series of small balls around the outside with a center ring to provide a balancing surface. The system is also equipped with a mechanically actuated switch to notify of deflection within the system. These early concepts have motivated more modern concepts that are discussed in the following section.

1.3.2 Modern Concepts

Historically, the advantages of isolating structures and components from ground and floor motions were easy to see and more modern designs that meet the criteria of current building codes and qualifications have been proposed. Many isolation systems for large scale structures have been developed and implemented in modern buildings and have proved to be beneficial for seismic hazard mitigation (Kelly, 1997; Symans et al., 2002; Warn and Ryan, 2012; Lin et al., 1990; Tsai, 2015). The focus of this study is on isolation of building contents/nonstructural components and therefore these large scale systems will not be reviewed further. The following focuses on current systems for component isolation.

The concept of isolating an entire floor can be beneficial when considering large scale nonstructural components or critical stations within a building. Cui et al. (2010) proposed a bidirectional spring system which isolated a top subfloor surface above the main superstructure floor. The upper subfloor rolls on the main superstructure floor using casters and the bidirectional springs provided the recentering forces for the system. A subsequent study (Cui et al., 2016) showed that entire floor isolation can be effective, but the study was limited to characterization for eccentric load cases. Liu and Warn (2012) quantified the performance of floor isolation for more general cases with variability in story level as well as variability in material properties of the structure. Lu et al. (2013) performed a series of tests for a polynomial friction pendulum floor isolation system where the shape of the profile was optimized to meet performance criteria under various seismic excitations. Damping has also been added to isolation of entire floor systems and has shown to effectively reduce bearing displacements (Arima et al., 1997; Kaneko et al., 1995).

Other designs have been proposed to meet the localized isolation criteria, such as at specific locations on a floor. A model proposed by Khechfe et al. (2002) used a

single mass block situated on the third floor of a structure which rested on rollers and was guided by rails. The recentering forces were provided by springs that attached to the superstructure at the edges of the floor. Damping was provided by sandwiching a steel plate, which was mounted to the isolated mass, between two stationary visoelastic blocks of material which would be engaged during excitation of the system.

A number of sliding isolation systems have also been proposed. Two systems, that were originally developed for buildings but have application for smaller systems are those of Penkuhn (1967) and Zayas (1987). These systems have an upper plate with a center shaft that connects to a swivel socket (articulated slider) that provides leveling. The contact between the swivel head and the lower concave bowl creates friction which dissipates energy as relative motion input base and the isolated object. Lambrou and Constantinou (1994) performed characterization tests for friction pendulum bearings for the protection of computer and network cabinets through isolation of an entire floor system; the tests simulated real operating conditions and the bearings were shown to be effective for the protection of such equipment. Tsai (2012) showed that long period excitations can create large impacts for typical sliding isolation systems and developed a multiple-friction pendulum system that has multiple concave surfaces and sliding mechanisms to address the various seismic excitations [Figure 1.4(a)]. One sliding mechanism will engage up until a specific point on the curve, at which point the breaking friction of the other will release allowing for further displacement at lower stiffness.

A number of studies have looked at the effects of friction damping on the response of isolation systems. Yang et al. (2011) numerically simulated the response of rolling systems with additional friction damping to evaluate its performance; friction was shown to reduce accelerations when combined with nonlinear restoring forces. Other numerical simulations have been used for parametric analysis of multi-degree-of-freedom struc-

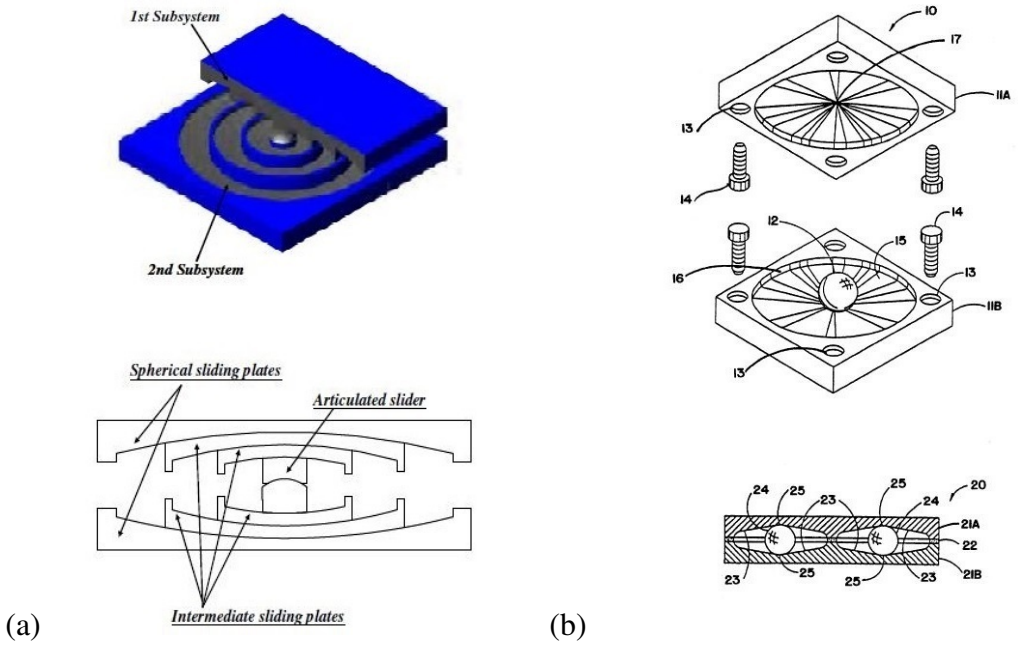

Figure 1.4: Modern isolation bearings: (a) Multiple friction pendulum bearing (Tsai, 2012) and (b) ball-in-cone (Kemeny, 1997).

tures to evaluate the coupling dynamics of the superstructure with that of the isolation system (Zhou et al., 1998; Caliò et al., 2003). Additionally, response optimization of models have been developed in order to asses and improve the reliability of friction pendulum dampers (Jia et al., 2014).

Further work done by Tsai (2012) has shown that friction pendulum bearings offer advantages over typical rolling-type isolation bearings due to having larger contact areas and thus higher damping capabilities. This removes high stress concentration from the system, which all rolling-types suffer from, as well as provides more energy dissipation. However, for application of isolation where the mass is relatively low, high damping forces may not be needed and rolling isolation offers a simple solution. The advantages of RISs are (i) the ability to isolate in any horizontal direction, (ii) the ease of implementing supplemental damping through treatment of the rolling surface, and (iii) the ability to provide recentering forces without the need springs/bearings in the orthogonal directions. All this is contained in a low profile that is simple to implement

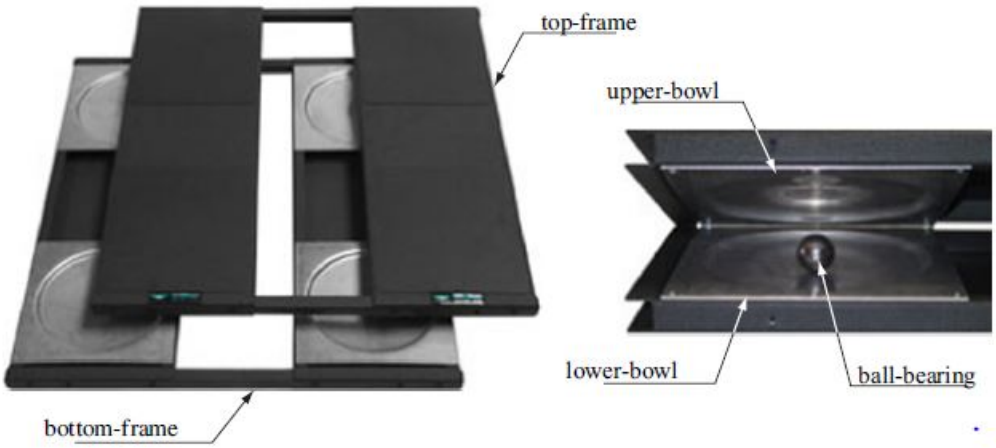

Figure 1.5: Typical rolling-type isolation system (WorkSafe Technologies, Inc., 2011).

making them ideal for network equipment, computer systems, and other nonstructural components.

Kemeny (1997), who acquired a US Patent in 1997, utilized a similar rolling design to Touaillon (1870); Schär (1910), which consists of a ball and cone type design [Figure 1.4(b)]. The difference is that it can use either a constant slope or a parabolic curve shape for the rolling surfaces. The instantaneous slope of these surfaces relates directly to the instantaneous stiffness of the system. This patent for a rolling-type isolation bearing is the basis for many current RISs, such as the ISO-Base seismic isolation platform (WorkSafe Technologies, Inc., 2011), which is shown in Figure 1.5. The system consists of top and bottom steel frames which are decoupled from each other via sets of rolling bearings. A bearing consists of two concave steel surfaces (bowls/dishes) which are attached to the steel frames in a counter-facing orientation. A steel ball is interposed between the rolling surfaces which allows for motion in any horizontal direction. These isolation platforms can easily be expanded to protect multiple pieces of equipment using additional planks, steel connecting bars, and sets of rolling bearings.

1.3.3 Characterization and Modeling

As noted before, isolation systems are characterized by their displacement capacity, stiffness, and damping. Current RISs suffer from limited displacement capability due to geometric constraints of typical operating environments such as compactness of server rooms, equipment anchorage locations, and service lines and cables that must be included (Harvey and Kelly, 2016). Large displacement capacity is needed for low frequency, long disturbances. To overcome this problem, different systems have been proposed to achieve larger displacements. Harvey and Gavin (2014) proposed a stacked system of rolling-type isolation bearings to achieve larger displacement without a larger footprint. This approach, however, produced impacts and therefore high accelerations even when the full displacement capacity was not achieved due to contact between the isolating layers.

One particular characteristic to rolling isolation is the source of stiffness within the system. Typically, gravity provides the restoring forces in these systems due to the low profile and difficulty of using springs or other stiffness devices. The gravitational recentering forces are directly related to the rolling surface profile. Jangid and Londhe (1998) proposed a design with elliptical rods sandwiched between two flat plates with the superstructure resting on the top plate. The change in height coupled with the eccentricity about the center of the rods created the restoring force. A more typical rolling surface is that of Kemeny (1997) who proposed a spherical profile, where a ball is interposed between the upper and lower profiles, as shown in Figure 1.6. The spherical profile can be approximated as a linear stiffness. A spherical-conical profile was also proposed which is a common nominal shape of current RISs.

As noted, the change in the gravitational potential energy associated with a relative vertical displacement between the frames generates the restoring force for the recentering of the frames via the concave surfaces of the rolling bearings. This is apparent from

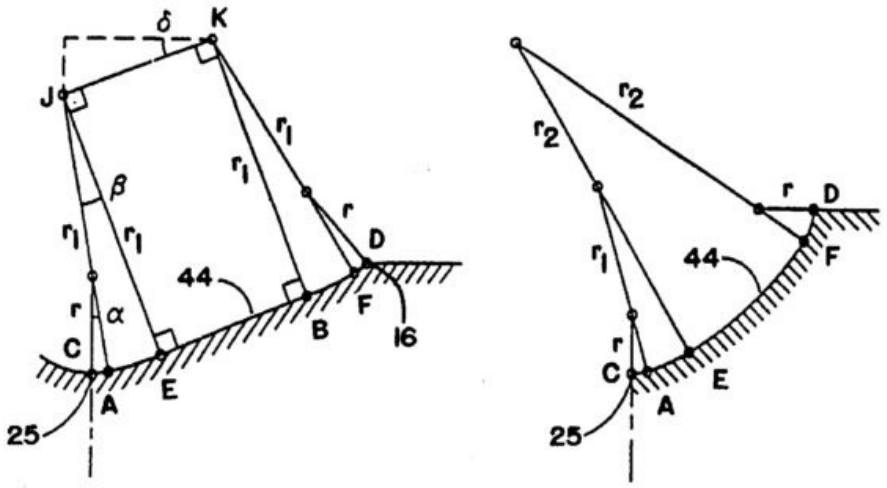

Figure 1.6: Rolling surface profiles (Kemeny, 1997).

the linearized (planar) equations of motion in the absence of damping forces (Harvey, 2015):

$$m\ddot{u} + mgh'(u) = -m\ddot{u}_g \tag{1.1}$$

where m is the isolated mass, u is the displacement across the bearing, and $h(u)$ is the resulting vertical displacement which is governed by the radial profiles η of the lower and upper bowls, $h(u) = 2\eta(u/2)$. The recentering force is $mgh'(u)$, which is equal to the weight of the isolated mass (mg) times the slope of the rolling surface at the ball location [$h'(u) \equiv \eta'(u/2)$]. The shape of the rolling surfaces are therefore highly influential in the response of RISs.

Figure 1.7 demonstrates this concept with a spherical-conical shape. The resulting restoring force with respect to the relative displacement of the upper bowl can be seen in Figure 1.7(b). The restoring force is linear in the spherical region ($u < 25$ mm) and constant over the conical portion ($u > 25$ mm). By manipulating Equation (1.1), the total acceleration sustained by the isolated object can be expressed as $a^t = \ddot{u} + \ddot{u}_g \equiv -gh'(u)$. The theoretical maximum sustained acceleration of the isolated object is,

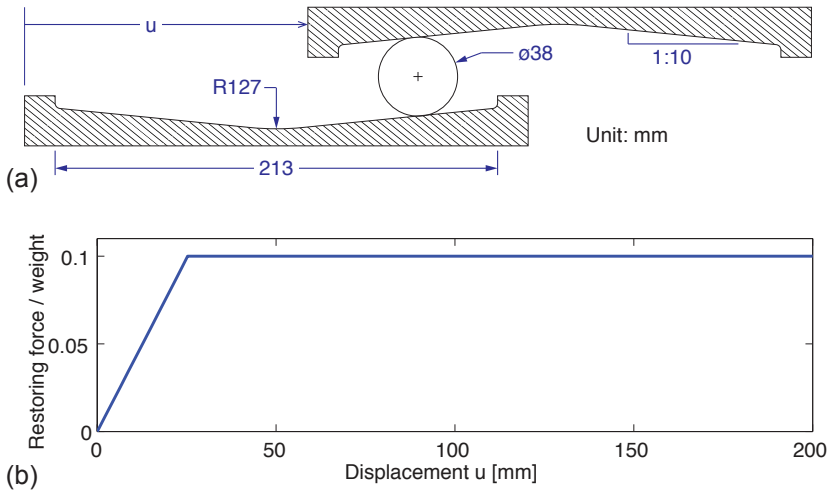

Figure 1.7: Typical rolling surface profile (a) and corresponding restoring force-displacement relationship (b).

therefore, given by $\max|a^{t}| = \max|-gh'(u)|$. For the spherical-conical shape [Figure 1.7(a)], the maximum occurs in the conical region of the profile where the acceleration is simply the slope of the rolling surface multiplied by gravity (e.g., $0.1g$). Therefore, the maximum sustained acceleration can be regulated by prescribing the slope.

In a series of tests performed by Harvey and Gavin (2013), the bowls of a RIS were mapped using a 3D scanner and then the data was used to calibrate a 3D bowl profile, from which the slope of the profile could be determined. The slope of the bowl profile is proportional to the restoring force and the curvature of the bowl profile is equivalent to the stiffness coefficient. Harvey et al. (2014) later showed that the experimental response did not exactly match the analytical response when using the 3D mapped profile. The stresses induced through installment of the bowl and the deflection caused from the isolated mass changed the bowl profile, causing the stiffness behavior to change.

For RISs, damping can easily be introduced through an application of an energy absorbing material to the rolling surface. Elastomeric materials, such as rubber, are commonly used due to the ease of application and the economic availability. A number

of models exist for the characterization of damping in a dynamic system using a rubber material. In an extensive study by Fiore et al. (2016), a mathematical model was derived for the contact interaction between a steel ball and a rubber layer using a Kelvin-Voigt material model. Using this contact model, equations for slip and stick regions for the rolling ball were found. The work found that forces on these regions are highly nonlinear and depend mostly on the velocity of the ball, the radius of the ball, and the thickness of the rubber layer. Foti et al. (2013) proposed a mathematical model for predicting the behavior and damping between a steel cylinder and rubber rolling surface. The study shows that at constant velocity the damping force is nearly linear with the applied vertical load and concludes that the size of the cylinder should be determined by the contact stress at the cylinder rubber interface.

Other research has shown that increasing the coupling of the ground motion and device using increased damping reduces the displacement capacity needed by such systems. Such systems use elastomers as the rolling surface which couples the motions and dissipates energy which mitigates damage (Harvey et al., 2014). Due to the complex nature of damping and dissipative energy, modeling such behavior is difficult. For lightly damped systems, dissipative forces can be modeled as linear with respect to velocity and nonlinear with respect to the applied vertical load. However, for heavily damped systems, using elastomeric rolling surfaces, the dissipative forces are no longer linear with respect to velocity. Harvey et al. (2014) developed a model through a series of experimental tests which accounts for the nonlinearity of the damping with respect to the mass and the velocity. Simulations have shown good agreement with experimental tests. The model is considered simplified as it does not take into account the hysteresis effects of the elastomeric rolling surface and the transients in rolling dynamics.

One of the defining characteristics of rolling isolation is the chaotic nature of these systems. Harvey and Gavin (2013) showed, through a series of experimental and nu-

merical simulations, that these systems exhibit chaotic trajectories that are sensitive to slight perturbations in the initial conditions of the systems, quantified using Lyapunov exponents; these chaotic tendencies are highly sensitive to the shape of the concave rolling surface. This chaotic nature, however, is seen to be less pronounced for forced ground excitations in which the motion is dominate in a particular direction. Despite this, the chaotic nature contributes to the difficulty of analyzing RISs for the dynamics through the kinematics of the upper and lower plates and their interaction through the balls that sit therebetween. The nonlinear interaction of the biaxial translations and rotational motion add an additional level of complexity to modeling these systems. Using Newtonian mechanics, it is difficult to arrive at the basic equations of motion. For this reason, the state variables and equations were derived using an energy approach and solved using Lagrange's equation. Numerical simulations using these equations of state have shown accurate results (Harvey and Gavin, 2013). This work developed expressions for potential and kinetic energy using the shapes of the rolling surfaces and the kinematics of the platforms and balls. In later work by Harvey et al. (2014), the method for determining the potential energy function was revised. The change in shape of the rolling surfaces from pre-installment to post-installment was considered different enough that an experimental free response tests were used to derive the potential energy function based on the displacement and acceleration data. The advantage of this method is that the dynamic effects on the shape are already included from the experimental data.

1.4 Proposed Study

The review of the literature in the previous section shows the effectiveness of RISs for the protection of structures and components for a range of applications. Previous numerical and experimental studies have assessed the performance of such systems through variation of stiffness, damping, and excitation level. Additionally, these studies have

explored a range of isolation devices such as friction pendulum bearings and rolling bearings. The literature shows a number of experimental characterization studies under realistic operating conditions, but these have traditionally been basic setups with no eccentricity and a single piece of equipment (cabinet). This thesis extends the current research by performing an experimental case study and numerical parametric study under realistic operating conditions that will vary eccentricity and number of cabinets, as well as the damping.

1.4.1 Mass Eccentricity

Many past studies have considered either rigid masses or a basic single cabinet setup with no eccentricity in the loading direction. However, real systems in normal operating conditions do not resemble rigid masses and likely will have some eccentricity in one of the orthogonal directions that will be engaged during excitation. Additionally, the eccentricity value is often not known prior to field setup due to room configuration, cable routing, and existing hardware. For this reason a performance evaluation over a range of eccentricity values is needed. From rigid body dynamics, the mass eccentricity is directly tied to the rotational response of a body. Rotation in RISs influences the displacement response. Due to the complex nature of RISs, many analytical models simply do not account for mass eccentricity. To determine the effect of mass eccentricity on the response of RISs, an experimental case study was conducted to distinguish its effect; the experimental setup and results are discussed in Chapters 2 and 3, respectively. A physics based mathematical model that includes mass eccentricity is proposed in Chapter 4 and used to further explore the effects of mass eccentricity through numerical simulations in Chapter 5.

1.4.2 Ganged Cabinets

One of the advantages of RISs is the ease of expandability. These systems can be readily "ganged" together to accommodate multiple cabinets or pieces of equipment. With multiple platforms ganged together, the aspect ratio of these systems changes and therefore their dynamics change. These changes are hard to experimentally characterize due to the size limitation of many shake tables as well as limitation in payload capacity. In Chapters 2 and 3, the effects of an expanded array platform is explored through an experimental case study of one and two cabinet systems. The mathematical model presented in Chapter 4 is an extension of existing models (Harvey and Gavin, 2013; Harvey et al., 2014) to account for ganged configurations. The mathematical model facilitates the numerical study of an arbitrary number of cabinets that are difficult to test experimentally. Finally, in Chapter 5 the model is calibrated from the free response tests and then used to assess the performance of ganged systems including up to eight cabinets.

1.4.3 Supplemental Damping

A number of sources in the literature have explored the effects of rolling surfaces treatment to add additional damping and energy dissipation to a system. However, limited case studies with parametric variation of the rolling surface under realistic operating conditions have been explored. In this study, two treatments of the rolling surfaces are used in the experimental setup described in Chapter 2. Then, the effects of increased damping—with and without a mass eccentricity and with increasing array size—are explored in Chapter 3.

1.5 Summary

Past earthquakes have caused extensive damage to buildings and nonstructural components. The loss of life, breakdown of critical facilities, and economic impact make the safety and functionality of earthquake design critical. A growing concern is that of nonstructural components which have been shown to be susceptible to earthquake damage. Network and computer equipment is one area of concern due to critical communications that they support and the vast wealth of information stored on them. One method that has proved to be an effective solution for the protection of nonstructural components is that of base isolation. A common type of isolation that is easy to implement is rolling-type isolation. The characteristics of RISs have been previously explored through experimental and numerical studies. Results show that displacement capacity is a critical parameter and estimation of demand must be accurately predicted. Displacements can be controlled through modification of the stiffness and damping, which limit displacements and removes harmful vibrations from a system. The literature shows limited experimental trials that consider mass eccentricity, number of cabinets, and level of damping under realistic operating conditions. This thesis explores these effects through an experimental case study and a numerical parametric study.

Chapter 2

Experimental Setup

2.1 Overview

Chapter 1 outlined the risk associated with seismic hazards and included various case studies of damage from past earthquakes. The case studies showed building contents and nonstructural components were major contributors to the damage and inhibited response of critical facilities and lifelines. A review of the literature showed isolation, using rolling-type bearings, improves the performance of building contents and nonstructural components when subjected to seismic excitations. However, limited tests have been performed to characterize rolling-type isolation systems (RISs) with computer and network equipment under real operating conditions with varying mass eccentricity, array sizes and number of cabinets, and supplemental damping. This chapter will outline the experimental setup for the case study that will be discussed in Chapter 3 for characterization of a RIS and network cabinet setup under earthquake excitations.

2.2 Setup and Testing

2.2.1 Experimental Overview

In order to perform an experimental case study for a RIS, accurate system setup and measurement is essential. A setup that proved to be very effective for the experimental

testing for seismic performance of nonstructural components was performed by Nikfar and Konstantinidis (2017). The setup utilized string potentiometers which measured the displacement of a shake table and a hospital equipment cart in the direction of the ground motion shaking to accurately measure the relative displacement of the table and cart. The string potentiometers were attached to rigid supports that sat just off the shake table and provided the fixed reference frame for the measurements.

Harvey and Gavin (2013) detailed an experimental setup that could properly capture the necessary state variables to fully define a RIS. The setup consisted of a RIS with four steel balls under the four corners. Three string potentiometers were used: two in parallel to measure the displacement in the transverse direction and the rotation of the isolation system and another one that measured the displacement in the longitudinal direction. A similar configuration was used in this study as described in Section 2.2.5.

2.2.2 Rolling-type Isolation Platform

As shown previously (Section 1.3.2, a number of RISs exist that use either balls, cylinders, or elliptical rolling bearings. The isolation platform used in this study (ISO-Base™) was manufactured and supplied by WorkSafe Technologies, Inc. (Valencia, CA). In this experimental study, a single platform system and a double (or "ganged") platform system were considered (Figures 2.1).

The rolling surface profiles considered in this study (Figure 1.7) have a 127-mm (5-in.) radius at the center and a constant 1:10 slope over the outer portion. This conical profile is commonly used because the peak sustained accelerations are (theoretically) limited to be equal to the slope times gravitational acceleration (Equation 1.1). Figure 1.7(b) shows the restoring force's relationship with displacement u. Note that the bowls have a lip at approximately 203 mm of displacement, which retards the bearing's motion. Impacts of the ball with the lip result in large forces and spikes in accelerations that are harmful to the isolated equipment.

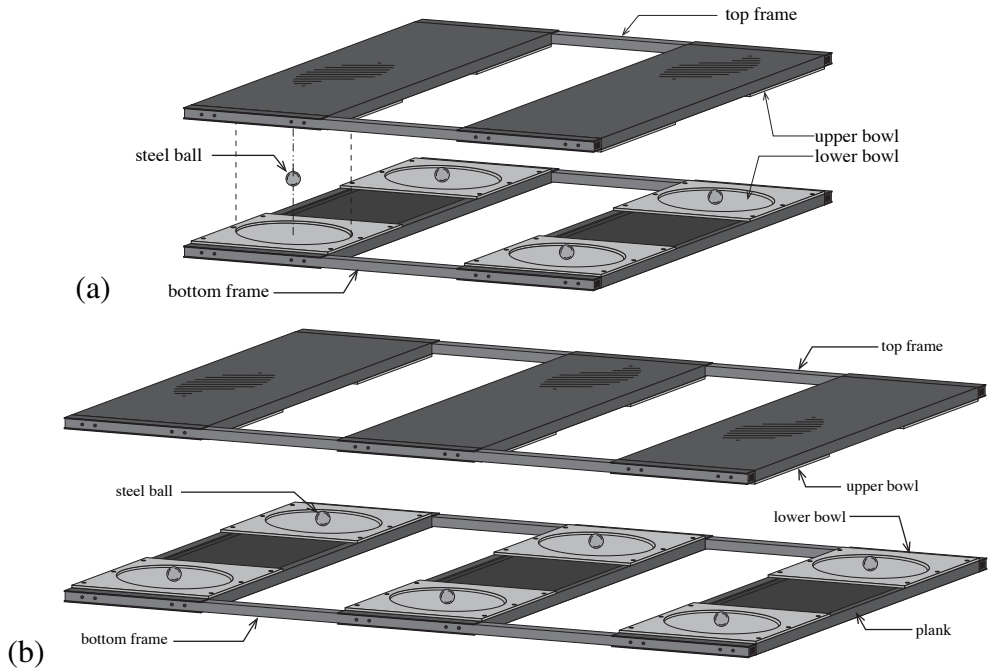

Figure 2.1: Overview of rolling isolation platform: (a) single and (b) double (or ganged) configurations.

Two different rolling dishes were utilized to vary the dissipative forces: bare steel dishes [Figure 2.2(a)] and damped dishes [Figure 2.2(b)]. The former results in very light damping which is optimal for acceleration attenuation performance, but may result in excessive displacements. The latter uses the same steel dishes with an elastomeric damping liner (QuakeCoat™, Worksafe Technologies, Inc., Valencia, CA) to introduce additional rolling resistance. This increased damping helps to reduce peak displacements at the expense of decreasing the acceleration attenuation performance.

Note that this experimental research focused on investigating fundamental behavior as opposed to validating a specific design procedure. Because the rolling surfaces had set geometric properties, parametric variation was provided by the rolling surface treatment (bare steel versus elastomeric lined), the loading condition (single versus ganged cabinets), and the seismic excitation direction and amplitude. The following section gives additional details on the specifics of the test setup that aimed to obtain a broad

(a) (b)

Figure 2.2: Rolling surfaces: (a) bare steel dish and (b) elastomeric lined dish.

range of operating conditions that are typically observed in the field.

2.2.3 Specimen Assembly and Setup

The isolated object(s) used in this study were typical server and network cabinets (42RU Dynamic Cabinets, Panduit, Tinley Park, IL). Two cabinet configurations were considered: a *Single* isolated cabinet [Figure 2.3(a)] and two *Ganged* isolated cabinets [Figure 2.3(b)]. The cabinet(s) were mounted to the isolation platform using the recommended manufactures attachment bracket as seen in Figure 2.4(a). The isolation platform was placed direction onto the table with no attachment as specified by the manufacture. Safety straps (seen in Figure 2.3) were used to prevent tipping of the cabinets upon excessive input ground motion. The straps were configured such that the influence on the response could be assumed negligible.

The overall dimensions of a single cabinet were 700-mm-wide $\times$ 1200-mm-deep $\times$ 2026-mm-tall as seen in Figure 2.5. Each cabinet had a frame mass of approximately 205 kg. Four (4) 125-kg trays were used to simulate typical servers and components installed in the cabinet [Figures 2.4(c) and (d)]. The overall mass of a loaded single cabinet was 705 kg with the center of mass (C.G.) located 122 mm from the geometric center in the front-to-back direction (X) and at a height of 740 mm from the bottom of the wheels; the center of mass was centered in the side-to-side direction (Y). Two (2)

(a) (b)

Figure 2.3: Overview of rolling isolated cabinet(s): (a) single cabinet configuration and (b) ganged cabinet configuration.

11.3-kg steel blocks were mounted to the top of the cabinets [Figure 2.4(b)] to simulate the mass of network cables that are typically mounted to the top of such systems in normal operation. This was determined by Panduit based on typical cabinet setup.

For a single cabinet isolation platform, the design contains two 273-mm-wide planks that were attached together via square tube bars. The bowls of the rolling bearings attached to recesses in the planks. For a ganged cabinet isolation platform, the design contains two 273-mm-wide plank as in the single platform that sit on the ends, along with larger plank that was 324-mm wide which sits between the two outside planks. The larger planks allows for two cabinets to bear on the surface therefore carrying twice the load. The same square-tube bars connect the planks. The bowls for the larger plank attached to recesses as in the smaller planks.

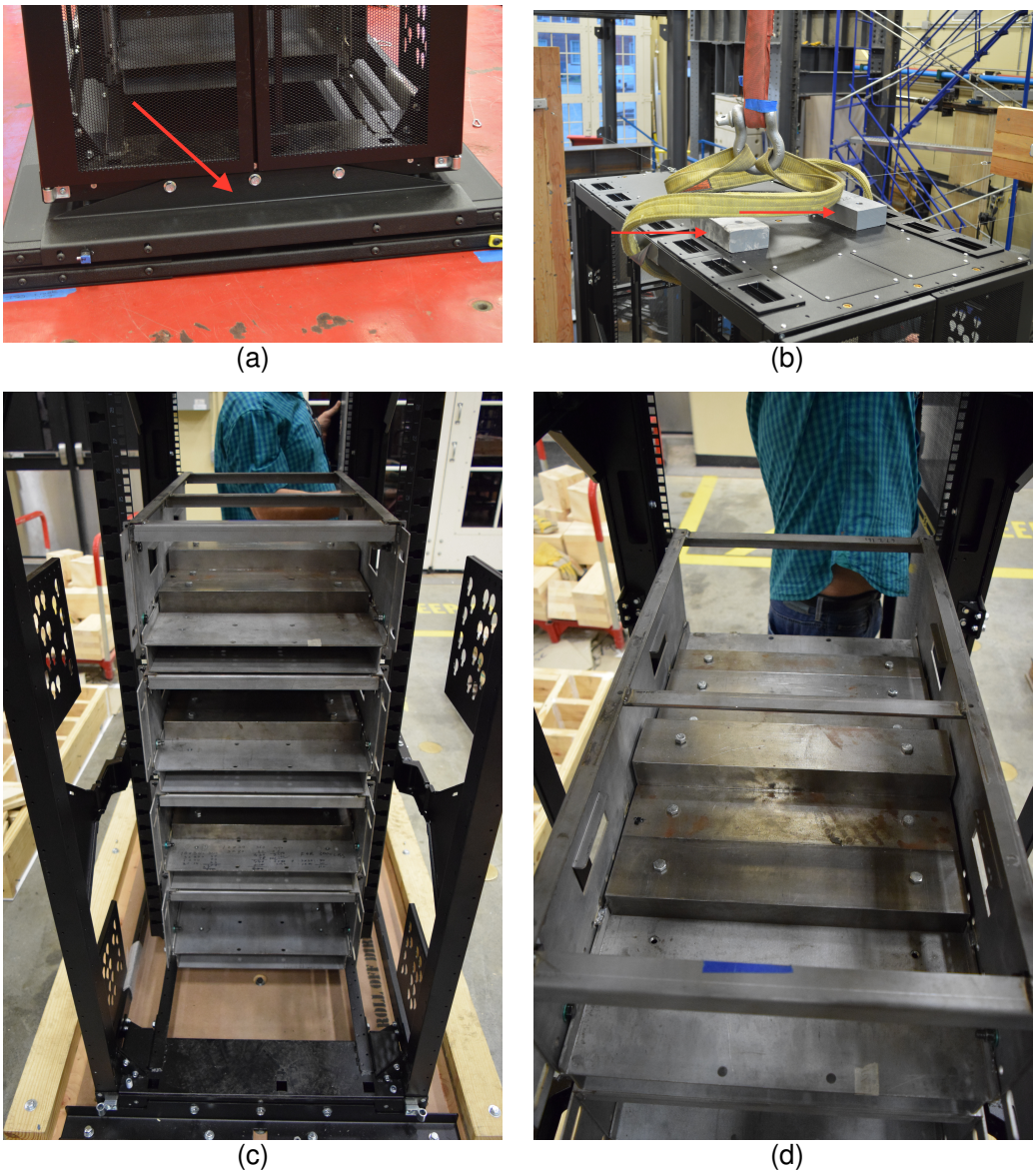

Figure 2.4: Attachment and shelf structure in 42RU Dynamic Cabinet used to simulate weight of mounted equipment: (a) mounting bracket, (b) simulated cabling, (c) equipment trays, and (d) mass attached to equipment trays.

2.2.4 Input Program and Test Protocol

Unidirectional characterization tests for the rolling isolation platforms were performed using both impulsive and seismic input motions. The tests were performed on the high-performance, uniaxial earthquake simulation table at the Large Scale Structures Labora-

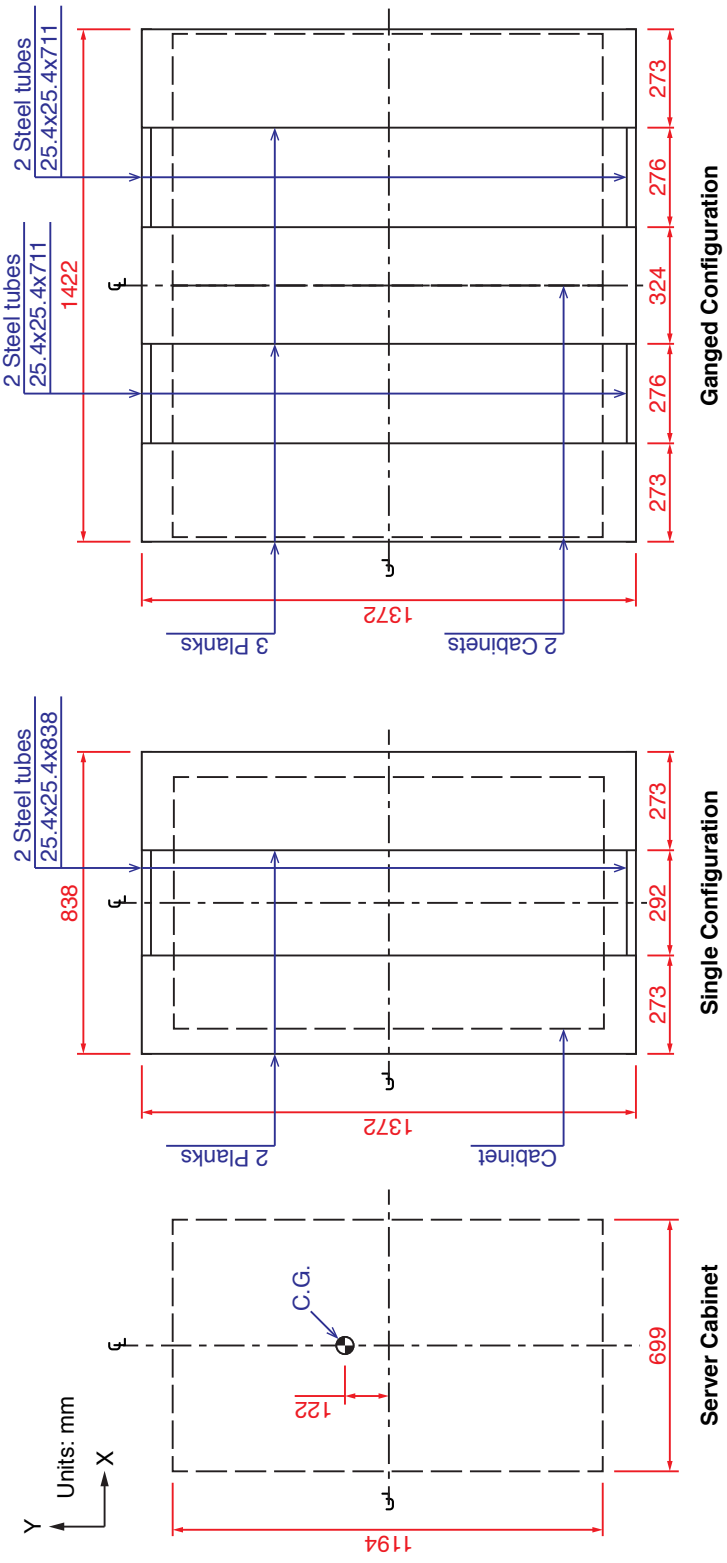

Figure 2.5: Plan dimensions of server cabinet and single and ganged configurations.

tory at the University of Alabama in Tuscaloosa, Alabama. With 2725 L/min hydraulic supply, the table is capable of reproducing ground motions with peak acceleration of 1.2g under the maximum payload of 18,144 kg. For the considered tests, payloads were well below the maximum capacity allowing for higher peak accelerations.

For the impulse tests, the shake table was given an abrupt displacement which initiated a relative displacement in the isolator resulting in a free response motion that was measured. Nominal table displacements of 10, 15, and 20 cm were used at a table velocity of 75 cm/s. The 20 cm displacement corresponds to the bearing displacement capacity.

For the seismic tests, the VERTQ-II Zone-4 waveform was utilized (Telcordia Technologies, 2012). This synthesized waveform is representative of a typical floor motion within a building and captures the variability in earthquake ground motion, building type, and soil site conditions. Figure 2.6(a) shows the acceleration time history for the input motion. The time history shows the maximum accelerations in excess of 1.5g which is quite high for a peak acceleration of a ground motion.* Figures 2.6(b) and 2.6(c) show the time histories for the velocity and displacement of the ground motion. Figure 2.6(d) shows the Test Response Spectrum (TRS) for a system with 2%-damping as well as the Zone-4 Required Response Spectrum (RRS) specified in the Telcordia Technologies GR-63-CORE standard. The input motion has low acceleration response at frequencies below 1 Hz, then has a quick ramp up to high accelerations (3g - 5g) which remain from 1 to 10 Hz, and then has a slow ramp down to moderate accelerations (2g) at approximately 15 Hz. The seismic input was scaled at 25, 50, 75, 100, and 125% in order to characterize the nonlinear response of the system.

Both the pulse tests and the seismic tests were conducted along orthogonal axes of the test specimen. Referring to Figure 2.5, the tests were conducted in the X and

*For comparison, the Northridge, Kobe, and Chi-Chi earthquakes had peak accelerations of 1.7g, 0.8g, and 1.0g, respectively.

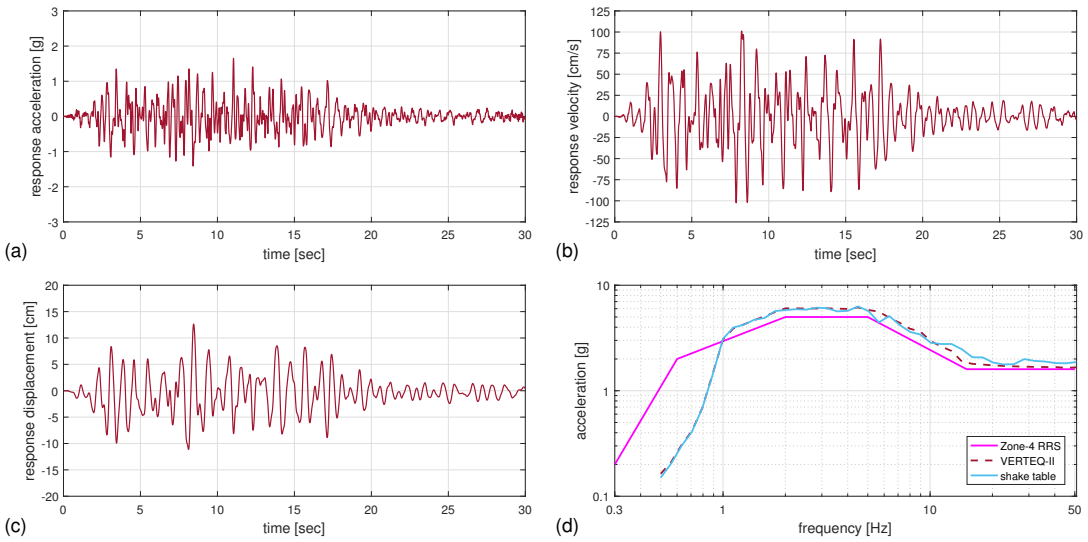

Figure 2.6: Ground motion waveform — (a) acceleration $\ddot{u}_g(t)$, (b) velocity $\dot{u}_g(t)$, and (c) displacement $u_g(t)$ — and (d) 2%-damped response spectrum.

Y directions, which will be referred to hereinafter as *front-to-back* and *side-to-side*, respectively. It should be noted that the former corresponds to a concentric loading through the center of mass, while the latter corresponds to an eccentric center of mass (relative to the center of stiffness) and should therefore result in larger rotations.

The sequence of test setups was conducted in a manner to be efficient in transitioning between configurations. The following sequence was followed:

1. Single cabinet, Damped dishes, Front-to-back (X)
2. Single cabinet, Damped dishes, Side-to-side (Y)
3. Ganged cabinets, Bare steel dishes, Front-to-back (X)
4. Ganged cabinets, Bare steel dishes, Side-to-side (Y)
5. Ganged cabinets, Damped dishes, Side-to-side (Y)
6. Ganged cabinets, Damped dishes, Front-to-back (X)
7. Single cabinet, Bare steel dishes, Front-to-back (X)

8. Single cabinet, Bare steel dishes, Side-to-side (Y)

The tests that were conducted are presented in Table 2.1. For a given setup (e.g., Single cabinet, Front-to-back, Damped dishes), the input motion tests were conducted in the order shown (reading down the column).

2.2.5 Instrumentation

The objective of the characterization tests was to capture the acceleration-displacement behavior of the RIS. Here, *acceleration* indicates the total acceleration of the shake table and top frame of the isolation platform relative to an inertial reference frame, and *displacement* is the displacement of the table relative to the strong floor or of the top frame of the isolation platform relative to the shake table.

An array of accelerometers and string potentiometers were deployed to measure the acceleration and displacement responses. Figure 2.7 shows the sensor layout used for the single cabinet configuration under front-to-back loading as a representative example.

Accelerometers

To measure the accelerations of the table, isolation system, and cabinet, six accelerometers (sixteen channels) were used. A uniaxial accelerometer (7290E-R-D-10, Endevco, Meggitt Sensing Systems, Irvine, CA) measured the table's acceleration (not shown in Figure 2.7).

To measure the accelerations in the isolation platform and cabinet, five (5) triaxial accelerometers (356A17, PCB Piezotronics, Depew, NY) were used: two (2) were located at the bottom of the cabinet, one (1) was located at mid height of the cabinet, and two (2) were located at the top of the cabinet. The locations of these accelerometers and be seen in Figure 2.8.

The accelerometers at the bottom of the cabinets were mounted directly to the isolation platform and used to capture the longitudinal (direction of shaking), transverse

Table 2.1: Summary of the tests conducted under different configurations.

Input motion		Damped dishes		Bare steel dishes	
Name	Scaling	Single cabinet	Ganged cabinets	Single cabinet	Ganged cabinets
VERTEQ-II	100	X / Y	X / Y	X / Y	X / Y
Pulse	50	X / Y	X / Y	X / –	X / –
Pulse	75	X / Y	X / Y	X / –	X / –
Pulse	100	X / Y	X / Y	– / –	– / –
VERTEQ-II	25	X / Y	X / Y	– / –	X / –
VERTEQ-II	50	X / Y	X / Y	– / –	X / –
VERTEQ-II	75	X / Y	X / Y	– / –	X / –
VERTEQ-II	100	X / Y	X / Y	– / –	– / –
VERTEQ-II	125	X / Y	– / –	– / –	– / –

X, Y, and – indicate front-to-back, side-to-side, and not tested, respectively.

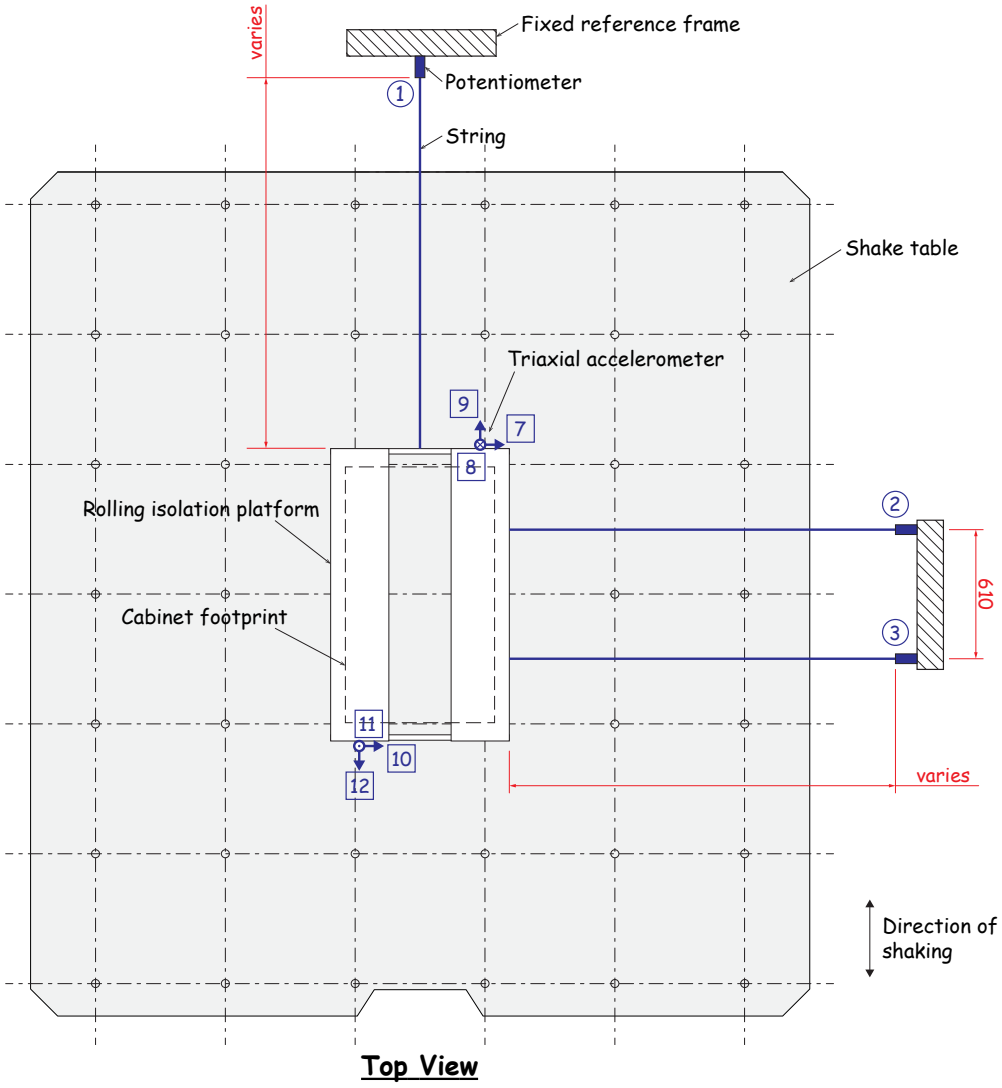

Figure 2.7: Sensor layout for experimental tests. Single cabinet in front-to-back (X) loading is shown as a reference

(perpendicular to shaking), and vertical components of the platform's acceleration; the locations of these accelerometers can be seen in Figure 2.7. These accelerometers were attached on opposite corners of the top frame, centered on the center line of the outer planks. The average of the parallel measurements taken with these accelerometers was used for the longitudinal and transverse translational accelerations in the isolation system.

The other three triaxial accelerometers (not shown in Figure 2.7) were used to measure the cabinet's acceleration. Because the focus of this thesis is on the isolation platform's response, these measurements are not presented or discussed hereinafter.

All accelerometers were mounted using hot glue which provided good attachment, but also provided slight damping to filter out unwanted high frequency vibrations in the system.

String Potentiometers

To measure the displacement of the shake table and isolation platform, one linear variable differential transformer (LVDT) and three string potentiometers (string pots) were used, respectively. The table displacement was measured using the LVDT (244.50S, MTS, Eden Prairie, MN) that was integrated into the shake table setup and measured the hydraulic-piston movement.

Three string pots (P510-30-S10-D05-10C, UniMeasure, Corvallis, OR) were arranged so as to capture the longitudinal, transverse, and rotational response of the isolation platform. One was aligned with the axis of the table (longitudinal direct), shown in Figure 2.7 by the number 1. The other two string pots (channels 2 and 3) were offset concentrically about the center of isolation platform by 610 mm and were configured to measure the displacement in the transverse direction to permit the rotation to be measured (see Section 2.3).

An additional three string pots (P510-30-S10-D05-10C, UniMeasure, Corvallis,

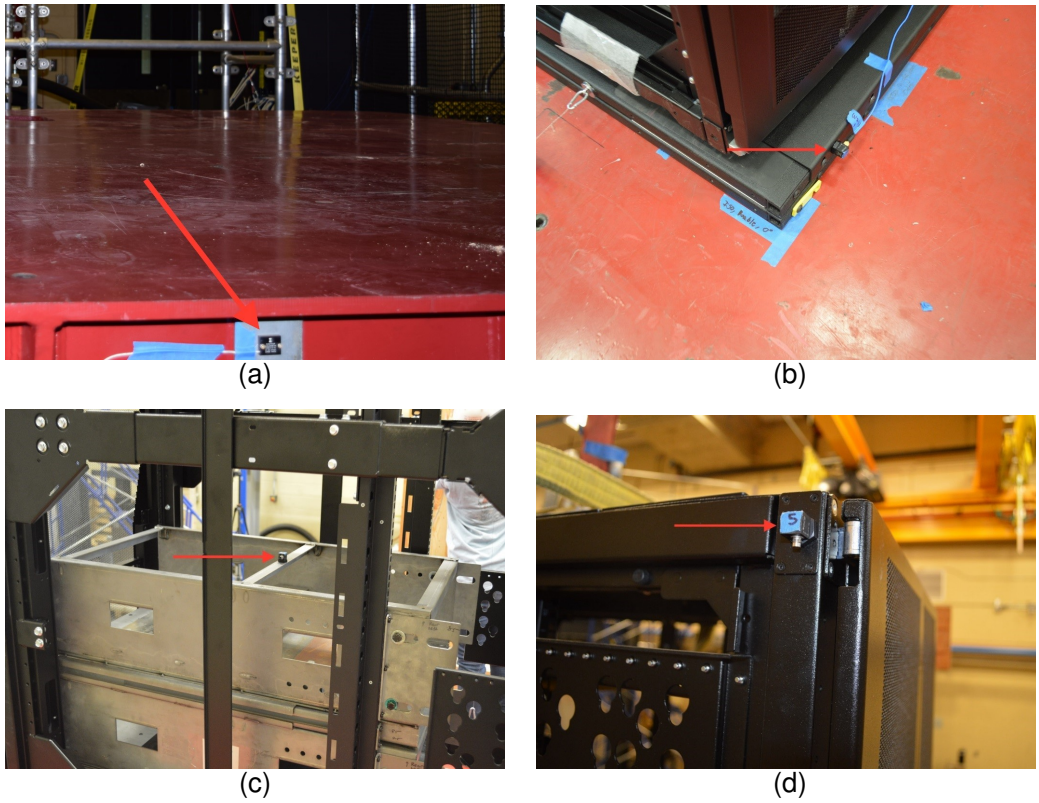

Figure 2.8: Accelerometer attachment locations: (a) table, (b) bottom of cabinet, (c) middle of cabinet, and (d) top of cabinet.

OR) were arranged so as to capture the longitudinal, transverse, and rotational response at the top of the cabinet. These were used to measure the relative drift in the cabinet. Because the focus of this thesis is on the isolation platform's response, these measurements are not presented or discussed hereinafter.

All the string pots were mounted to stationary reference frames fixed to the strong floor (see Figure 2.9). Piano wire was used to add additional length to the strings such that their initial travel was approximately half of their capacity. The free ends of the wire were attached to top frame of the isolation platform using strong magnets in case of over extension to prevent damage to the sensor. The initial lengths of the strings (plus piano wire) at zero platform displacement varied depending on the cabinet configuration and test orientation.

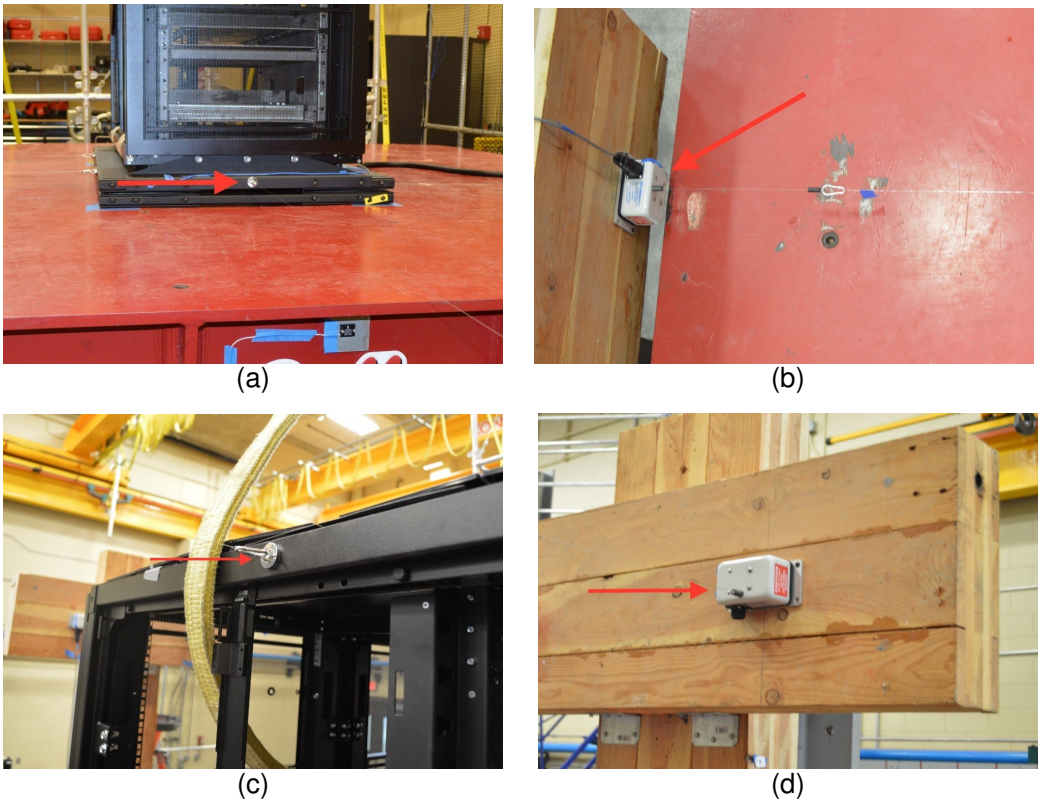

Figure 2.9: String potentiometer attachment locations: (a) bottom cabinet attachment, (b) bottom sensor wall mount, (c) top cabinet attachment, and (d) top sensor wall mount.

In the longitudinal direction (channel 1), the initial string length was 2108 and 2356 mm for the single cabinet configuration in the front-to-back (X) and side-to-side (Y) loading directions, respectively, and 2108 and 2089 mm for the ganged configuration in the X and Y loading directions, respectively.

In the transverse direction (channels 2 and 3), the initial string length was 1372 and 1132 mm for the single cabinet configuration in the X and Y loading directions, respectively, and 1080 and 1099 mm for the ganged configuration in the X and Y loading directions, respectively.

2.3 Data Acquisition and Processing

For each test, eleven channels of data† were collected using Simulink (Mathworks, Natick, MA). Each data channel was sampled at 4096 Hz. The raw data signals from all the devices were multiplied by their respective sensitivity to get the voltage signals into engineering units. These acceleration and displacement records were then post-processed in Matlab (Mathworks, Natick, MA) using the procedures described below.

Accelerations

The longitudinal acceleration of the isolation platform was obtained by averaging the accelerations in the two accelerometers in the longitudinal direction; for example, in the setup shown in Figure 2.7, channels 9 and 12 would be averaged after reversing the direction (sign) of one of these channels, e.g., $a^{\mathrm{t}}_{\mathrm{long}} = (a_9 - a_{12})/2$. The same process was followed for the accelerations in the transverse direction; the two accelerometers in that respective direction (e.g., channels 7 and 11) were averaged.

Displacements

The LVDT directly measures the table displacement u_{g} in the longitudinal direction.

As previously discussed, the displacement measurements taken with the string pots had an arbitrary initial offset due to varying platform geometries (and orientations) and the thin metal wires used. So, the initial displacement was subtracted from each channel's measurement to bring the initial measurement to zero. The string lengths and the transverse displacement and rotation are related through the nonlinear kinematics of the system (Harvey and Gavin, 2013), which requires solving the simultaneous nonlinear equations to determine the location of the isolation system at every point in time. To avoid this computationally expensive calculation, a small angle assumption was used to

†Additional sensors were installed on the cabinet (three triaxial accelerometers and three string potentiometers), but, because the focus of this paper is on investigating fundamental behavior of the isolation platform, data from these sensors will not be reported or discussed further.

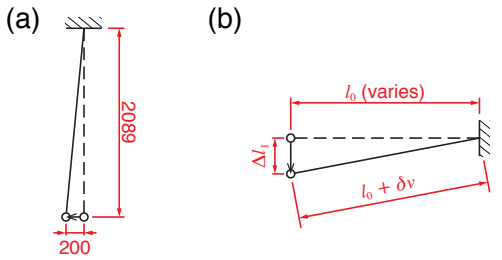

Figure 2.10: String potentiometer geometry for calculating platform displacements: (a) critical longitudinal case (units: mm); (b) geometry for determining correction term δv for transverse case.

permit simplified calculation (vector addition and multiplication) of the displacements and rotation. The procedure is described here.

First, consider the longitudinal direction. The longitudinal platform displacement u was taken to be the difference in the change in length of the longitudinal string pot Δl_1 and the table displacement u_g:

$$u(t) \approx \Delta l_1(t) - u_g(t) \tag{2.1}$$

There is inherent error in this assumption should there be a transverse displacement or rotation in the system. The most sensitive (critical) case is for the shortest initial string length of 2089 mm with a table displacement of 130 mm (peak ground displacement for the VERTEQ-II waveform) toward the potentiometer, a transverse displacement of 200 mm (capacity of rolling bearings), and no longitudinal platform displacement, as shown in Figure 2.10(a). Equation (2.1) gives 10.2 mm of longitudinal platform displacement, whereas there is in fact zero displacement. Note that this is only 5% of the bearings displacement capacity, and this is a highly conservative (or worst case) scenario because most of the motion will be in the longitudinal direction and its unlikely these assumptions would actually occur simultaneously.

Next, consider the transverse direction. Due to the predominant longitudinal motion and shorter initial string lengths in the transverse direction, a correction was applied to

obtain a more accurate result. Namely, the transverse displacement v was taken to be

$$v(t) \approx \frac{\Delta l_2 + \Delta l_3}{2} - \delta v \tag{2.2}$$

The correction term δv is found from the quadratic equation:

$$(\delta v)^2 + 2 l_0 \delta v - (\Delta l_1)^2 = 0 \tag{2.3}$$

where l_0 is the initial transverse string length. When the system is subject to a longitudinal displacement only [see Figure 2.10(b)], the correction in the transverse direction is exact. Yet, when the system is subject to a longitudinal displacement and a rotation, a slight error in the transverse measurements Δl_2 and Δl_3 occur. However, assuming small angles for the transverse strings, the error in the measurements is appreciably small and the final result is taken to be accurate.

Finally, to determine the rotation of the platform, the difference in the two transverse displacement measurements were used:

$$\theta = \arcsin\left(\Delta l_2 - \Delta l_3\right)/s \tag{2.4}$$

where s is the separation distance between potentiometers 2 and 3. The same error in Δl_2 and Δl_3 from rotation is also assumed to be appreciably small and the result is taken to be accurate.

2.4 Summary

Isolation has shown to be an effective technique for the protection of building contents and nonstructural components. A dearth of research exists in the characterization of RISs under real operating conditions and system setups, including eccentricity with respect to the loading direction, array size and number of cabinets, and addition of supplemental damping. An experimental case study was performed to characterize and quantify system behavior through variation of eccentricity, array size and mass, and

supplemental damping. Two different sized rolling isolation system were considered which consisted of platforms with spherical-conical rolling surfaces with steel balls interposed therebetween. Typical network cabinets loaded with dummy masses, in order to simulate equipment trays and cabling, were used. An array of string potentiometers and accelerometers were deployed in order to capture the system response. The data was collected using Simulink and processed using Matlab. A correction factor was used for the transverse displacement due to the error resulting from the motion in the longitudinal direction. The rotation in the system was captured through the measurement of two respective displacements in a single axis. Free response tests were performed using abrupt table displacements of 10, 15, and 20 cm. Finally, forced response tests were performed using the VERTEQ-II Zone-4 time history with 25, 50, 75, 100, and 125 % ground motion scaling. The results of the free and forced response tests are presented in Chapter 3.

Chapter 3

Experimental Results

3.1 Overview

Chapter 2 outlined an experimental setup for testing a rolling-type isolation system (RIS) consisting of a rolling platform with computer network equipment mounted to the platform. The system was configured with an array of string potentiometers and accelerometers in order to measure the displacements and accelerations. This chapter will outline the results for the free and forced response tests which were performed using an abrupt table displacement and the VERTEQ-II waveform, respectively.

3.2 System Characterization

In order to characterize the RIS, a series of experimental free response tests were performed while varying the different system characteristics. The tests performed utilized an abrupt displacement (pulse) from the shake table to excite the system in a controlled manner and then the free response was measured. The (effective) period T of the system was found by locating successive peaks in the displacement response. To obtain the theoretical damping ratio ζ in the RIS, log decrement was used. Assuming a linear response of a viscously damped system, the decrement δ over n cycles of motion is

$$\delta = \frac{1}{n} \ln \frac{u(t)}{u(t + nT)} \equiv \frac{2\pi\zeta}{\sqrt{1 - \zeta^2}} \tag{3.1}$$

Rearranging terms, the damping ratio is found from the following equations:

$$\zeta = \frac{1}{\sqrt{1 + (2\pi/\delta)^2}} \tag{3.2}$$

Table 3.1 shows the estimated natural periods and damping ratios for the configurations tested.

3.2.1 Bare Steel Dishes

Pulse tests were performed on the single and ganged cabinet configurations with bare steel dishes in the front-to-back orientation only. The abrupt table motion was performed at a speed of 75 cm/s and two different levels of table displacements were used: 10 and 15 cm. Figures 3.1 and 3.2 show the free response results for the single and ganged cabinets with bare steel dishes in the front-to-back orientations, respectively, for a 15-cm table displacement. Figures 3.1 and 3.2 show the (a) longitudinal and transverse displacements, (b) longitudinal and transverse accelerations, (c) rotation, and (d) acceleration-displacement responses for the single and ganged cabinets, respectively, with bare steel dishes in the front-to-back orientation. The tests for the 10-cm table displacement (not shown) exhibited similar results for the displacements and accelerations,

Table 3.1: Estimated natural period and damping ratio from pulse tests in the X / Y (front-to-back / side-to-side) directions.

Bare steel dishes		
	Single cabinet	Ganged cabinets
Natural Period [sec]	1.84 / –	1.87 / –
Damping Ratio [%]	3.70 / –	4.00 / –
Damped dishes		
	Single cabinet	Ganged cabinets
Natural Period [sec]	1.60 / 1.80	1.60 / 1.62
Damping Ratio [%]	35.7 / 41.2	42.1 / 49.0

Configurations not tested are indicated by '–'.

but with lower amplitudes.

The systems oscillated for 18 – 20 seconds following the impulse, before coming to rest. The ganged cabinet setup (Figure 3.2) shows an increase in the time for the oscillatory motion to decay away. This is expected as the energy associated with the ganged cabinets is higher from having approximately double the mass versus that of the single cabinet and therefore more energy to dissipate during its motion. The time to dissipate this energy, however, is not double due to an increase in the damping and therefore rolling resistance from the higher mass that the steel balls must support.

Both systems also show a decreasing natural period at small displacements as the response decays, which is representative of a softening system; the periods listed in Table 3.1 for the RISs equipped with bare steel dishes were calculated for the first full cycle of motion ($n = 1$).

The free response results for the single cabinet setup in the front-to-back orientation (Figure 3.1) show transverse displacements that begin after about three cycles of motion when small perturbations in the system cause a transition of energy from the longitudinal mode into the transverse and rotational modes. For this reason the longitudinal displacement does not decay away exponentially, but is more linear until small displacements within the rounded bottom surface of the dishes are only present.

Finally, the acceleration displacement plots [Figures 3.1(d) and 3.2(d)] follow the expected theoretical response. The plots are linear in the small displacement regimen where the stiffness is constant and then the hysteric loop flattens out as the displacement becomes large, beyond the rounded concave surface, where the restoring force becomes constant (see Figure 1.7). The elliptical loop at small displacements is indicative of viscous damping, which is expected from lightly damped systems where the rolling resistance is low (Harvey and Gavin, 2013).

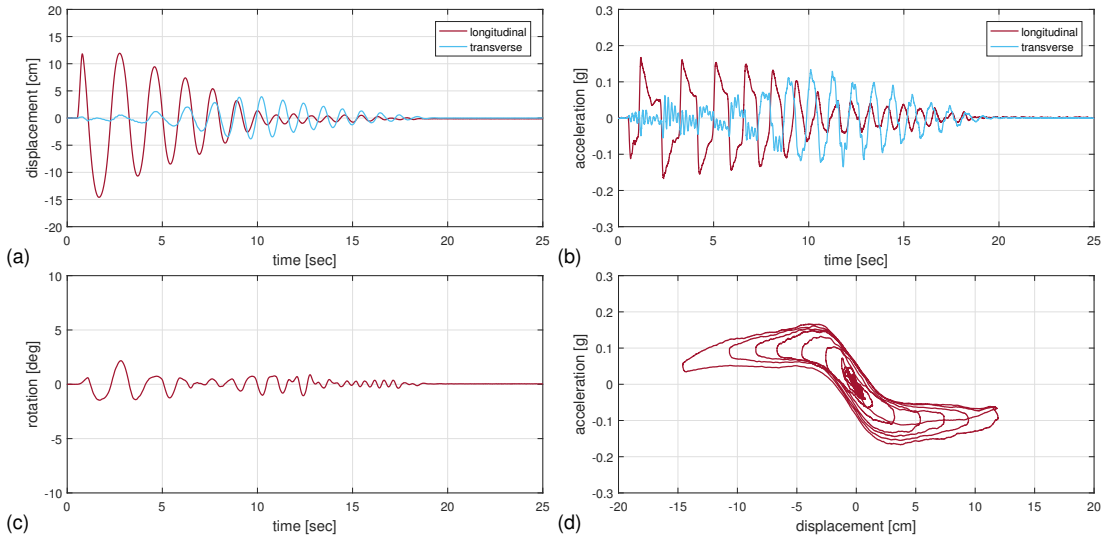

Figure 3.1: Free response results for single cabinet with bare steel dishes in the front-to-back orientation at a 15-cm table displacement: (a) longitudinal and transverse displacement, (b) longitudinal and transverse accelerations, (c) rotation, and (d) acceleration versus displacement.

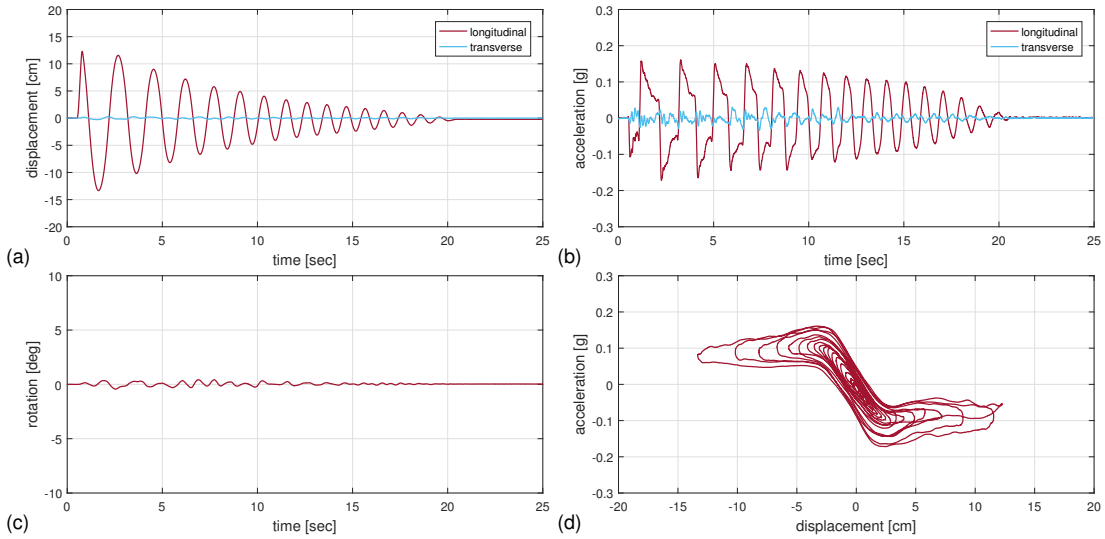

Figure 3.2: Free response results for ganged cabinets with bare steel dishes in the front-to-back orientation at a 15-cm table displacement: (a) longitudinal and transverse displacements, (b) longitudinal and transverse accelerations, (c) rotation, and (d) acceleration versus displacement.

3.2.2 Damped Dishes

Free response characterization tests were also performed for the systems with the damped dishes. An abrupt displacement from the shake table was used to excite the system and then the free response results were measured. The same displacement speed of 75 cm/s was used and three different levels of table displacement were performed; 10 cm, 15 cm, and 20 cm. Figures 3.3, 3.4, 3.5, and 3.6 show the free response results for the single cabinet and ganged cabinets in the front-to-back and side-to-side orientations with a 20-cm table displacement. The tests for the 10 and 15-cm table displacements for all configurations (not shown) exhibited similar results for the displacement and acceleration results, but with reduced amplitudes.

The results show a much quicker dissipation of the oscillatory motion versus that of the bare steel dishes. This is caused from an increase in supplemental damping. The plots also show a much quicker decrease in the natural period at small displacements versus that of the lightly damped system, which is also representative of a softening system; the periods listed in Table 3.1 for the RISs equipped with damped dishes were calculated for the first half cycle of motion ($n = 0.5$).

Different from the bare steel dishes, ganged cabinets with supplemental damping do not take longer to decay away. The damping is so high that energy is dissipated very quickly out of both the single cabinet and the ganged cabinet setups and therefore no difference in the time to cease oscillatory motion is noted.

Unlike the free response results for the bare steel dishes in the front-to-back orientation, transverse displacements for the damped dishes in the front-to-back orientation do not really form, indicating that energy does not transition from the longitudinal mode into the transverse and rotational modes.

The introduction of a mass eccentricity with respect to the loading condition (i.e., side-to-side, Figure 3.5) shows strong correlation with measured rotation. Figure 3.5

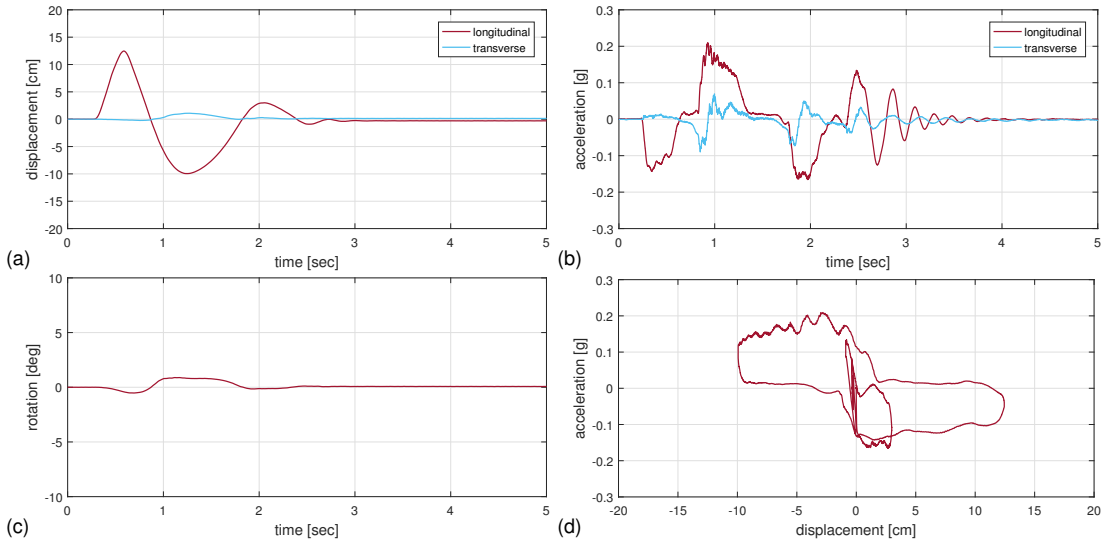

Figure 3.3: Free response results for single cabinet with damped dishes in the front-to-back orientation at a 20-cm table displacement: (a) longitudinal and transverse displacements, (b) longitudinal and transverse accelerations, (c) rotation, and (d) acceleration versus displacement.

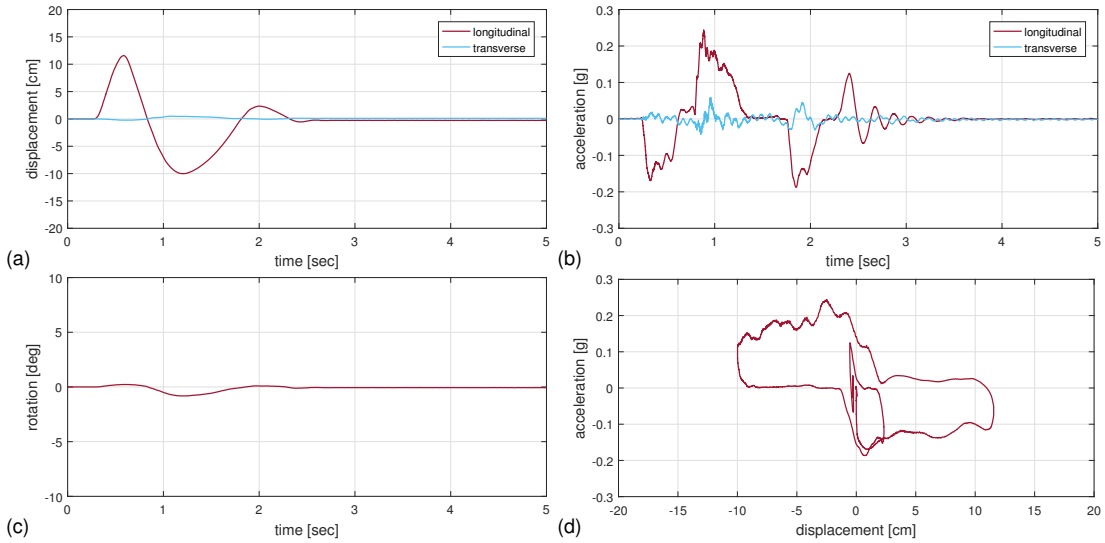

Figure 3.4: Free response results for ganged cabinets with damped dishes in the side-to-side orientation at a 20-cm table displacement: (a) longitudinal and transverse displacements, (b) longitudinal and transverse accelerations, (c) rotation, and (d) acceleration versus displacement.

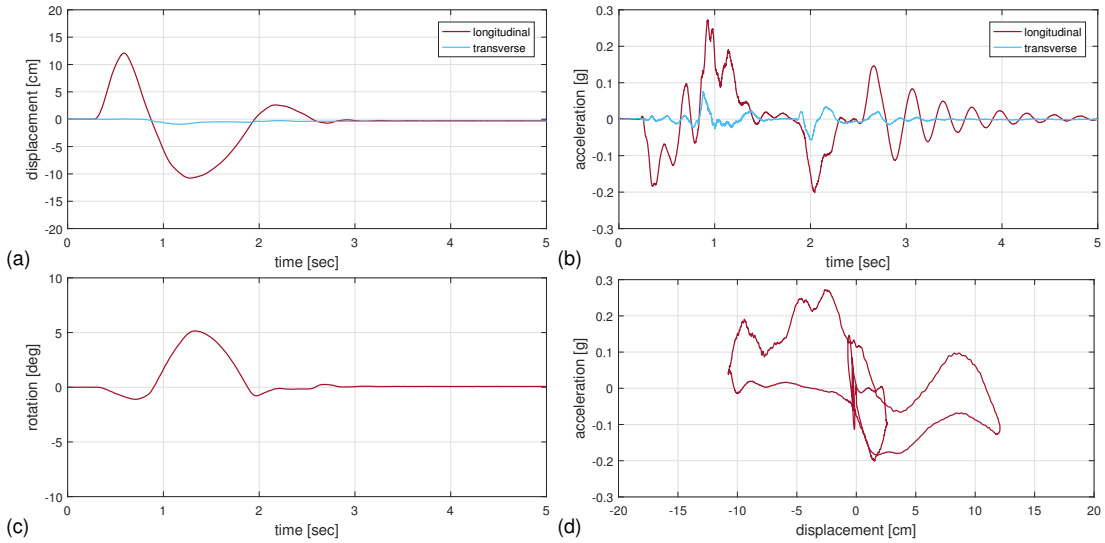

Figure 3.5: Free response results for single cabinet with damped dishes in the side-to-side orientation at a 20-cm table displacement: (a) longitudinal and transverse displacements, (b) longitudinal and transverse accelerations, (c) rotation, and (d) acceleration versus displacement.

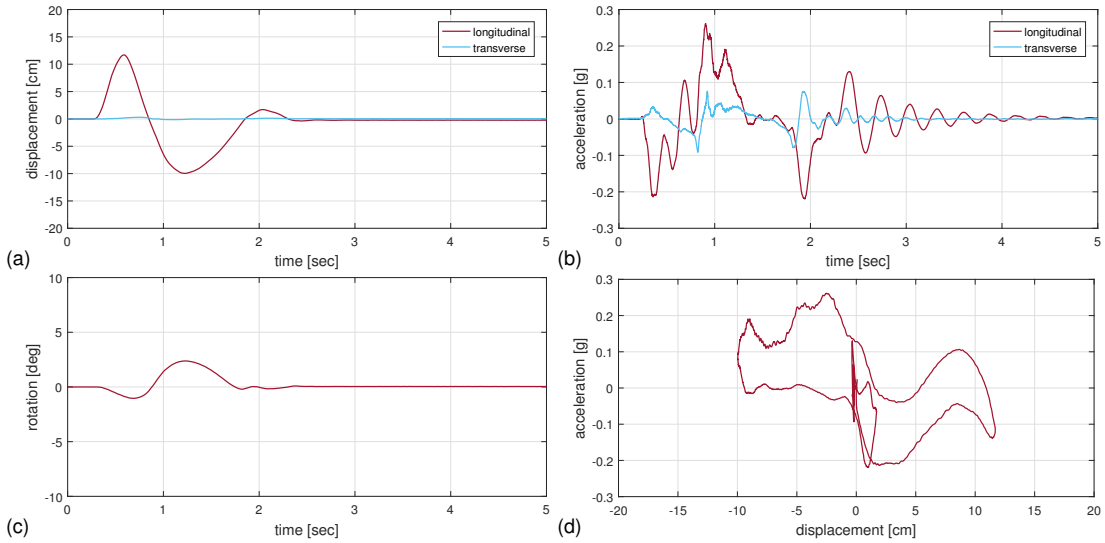

Figure 3.6: Free response results for ganged cabinets with damped dishes in the side-to-side orientation at a 20-cm table displacement: (a) longitudinal and transverse displacements, (b) longitudinal and transverse accelerations, (c) rotation, (d) acceleration versus displacement.

shows a maximum rotation of approximately 5° for the single cabinet setup in the side-to-side orientation. The ganged cabinet setup in the side-to-side orientation (Figure 3.6) shows similar results with a maximum rotation of approximately 3°.

The acceleration-displacement plots for the damped rolling surfaces [Figures 3.3(d), 3.4(d), 3.5(d), and 3.6(d)] follow the same pattern as that of the lightly damped setups but with a more rectangular shape following that of a coulomb friction damping model.

3.3 Forced Response Results

3.3.1 Bare Steel Dishes

Forced response tests were performed with the bare steel dishes for the single and ganged cabinet setups in the front-to-back and the side-to-side orientations. Figures 3.7 and 3.9 show the forced response results for the single cabinet with bare steel dishes in the front-to-back and the side-to-side orientations, respectively, at a ground-motion scaling of 100%. The tests for the ganged cabinet setups (Figures 3.8 and 3.10) exhibited similar results as those of the single cabinet setups. In each case, the rolling balls impacted with the lip/edge of the dishes when the maximum isolator displacement (20 cm) was reached, causing spikes in the acceleration measurements. These points are marked in the figures by the filled circles. At the point of impact, the piezo-electric type accelerometers dropped their charge, and the signals had a lag time in order to begin accurate measurement again. It should be noted that a maximum platform displacement of 20 cm may not be evident in the displacement plots. Some of the tests hit the displacement limit due to a combination of longitudinal, transverse, and rotational displacement occurring at the same time.

As seen in Table 2.1 the full testing regimen was not performed. The reason for this was durability problems experienced for the bare steel dishes. Figure 3.11 shows the adverse affects of repeated tests on a bare steel dish. Excessive rutting can be seen

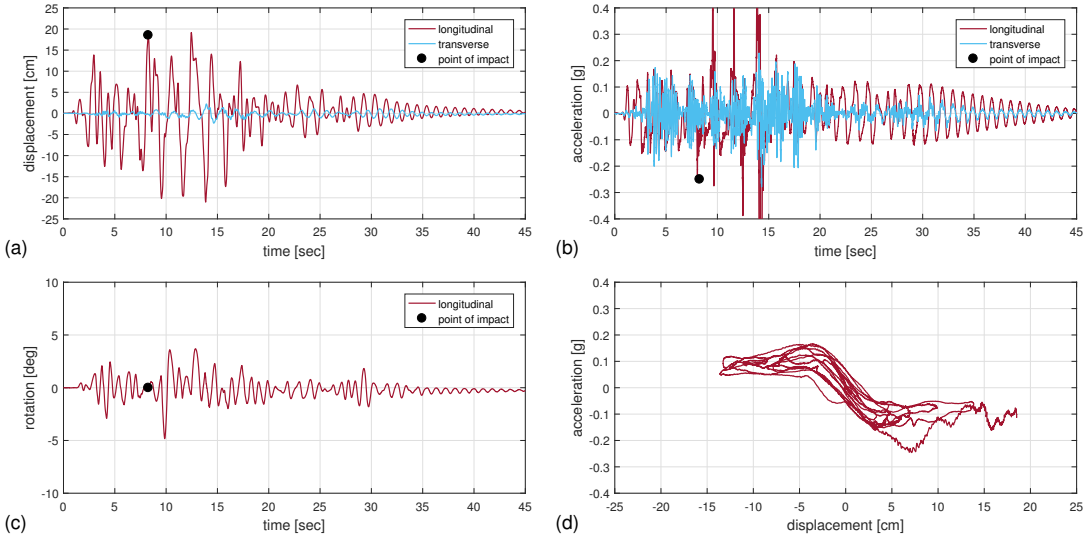

Figure 3.7: Forced response results for single cabinet with bare steel dishes in the front-to-back orientation at 100% ground motion scaling: (a) longitudinal and transverse displacements, (b) longitudinal and transverse accelerations, (c) rotation, (d) acceleration versus displacement.

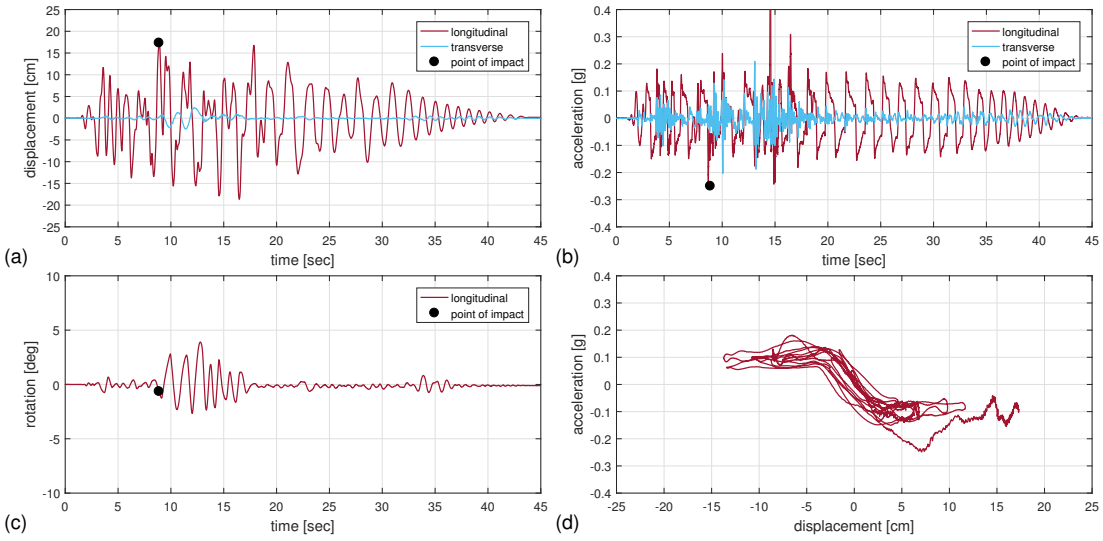

Figure 3.8: Forced response results for ganged cabinets with bare steel dishes in the front-to-back orientation at 100% ground motion scaling: (a) longitudinal and transverse displacements, (b) longitudinal and transverse accelerations, (c) rotation, (d) acceleration versus displacement.

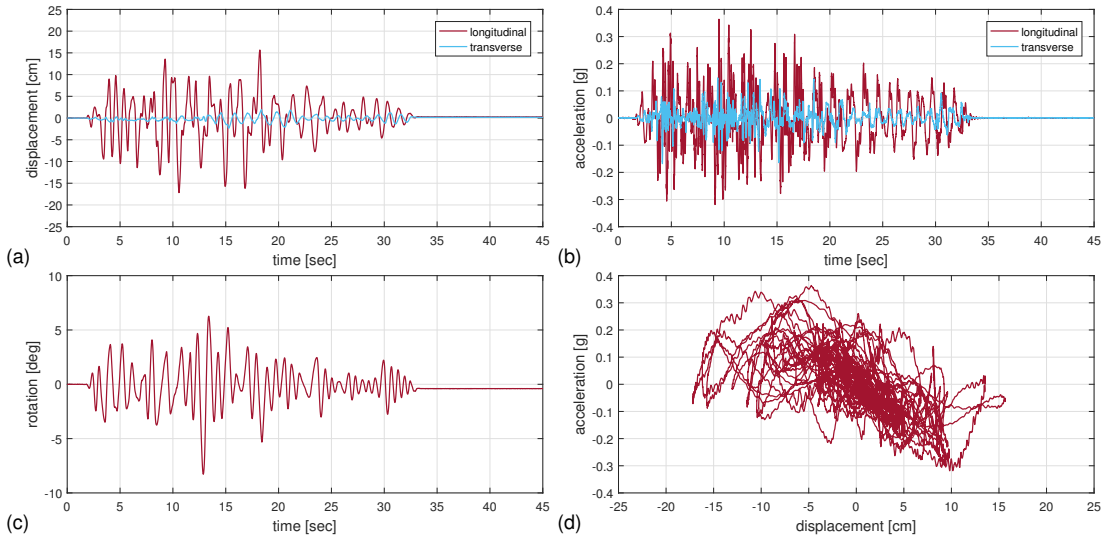

Figure 3.9: Forced response results for single cabinet with bare steel dishes in the side-to-side orientation at 100% ground motion scaling: (a) longitudinal and transverse displacements, (b) longitudinal and transverse accelerations, (c) rotation, (d) acceleration versus displacement.

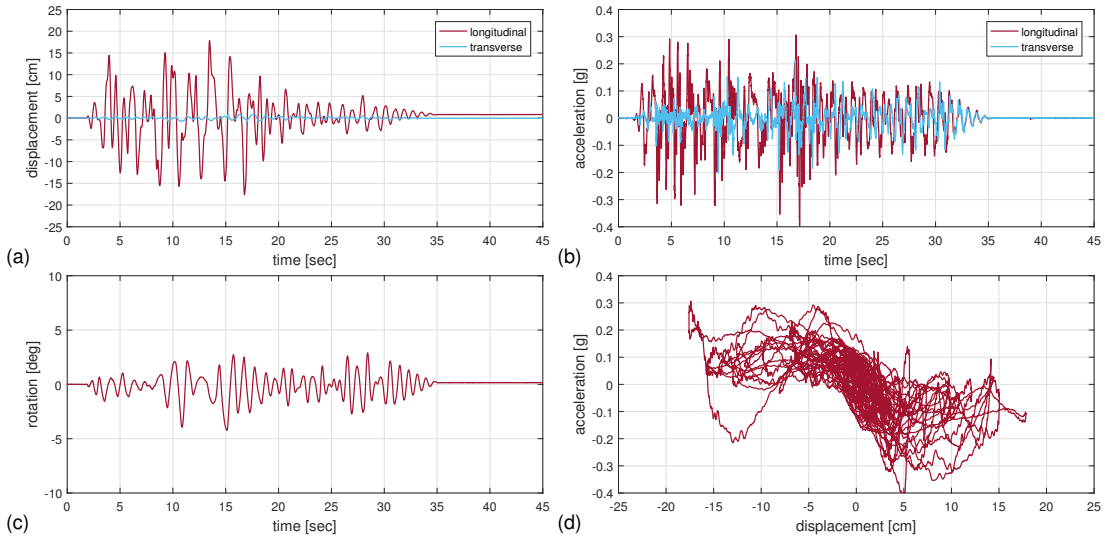

Figure 3.10: Forced response results for ganged cabinets with bare steel dishes in the side-to-side orientation at 100% ground motion scaling: (a) longitudinal and transverse displacements, (b) longitudinal and transverse accelerations, (c) rotation, (d) acceleration versus displacement.

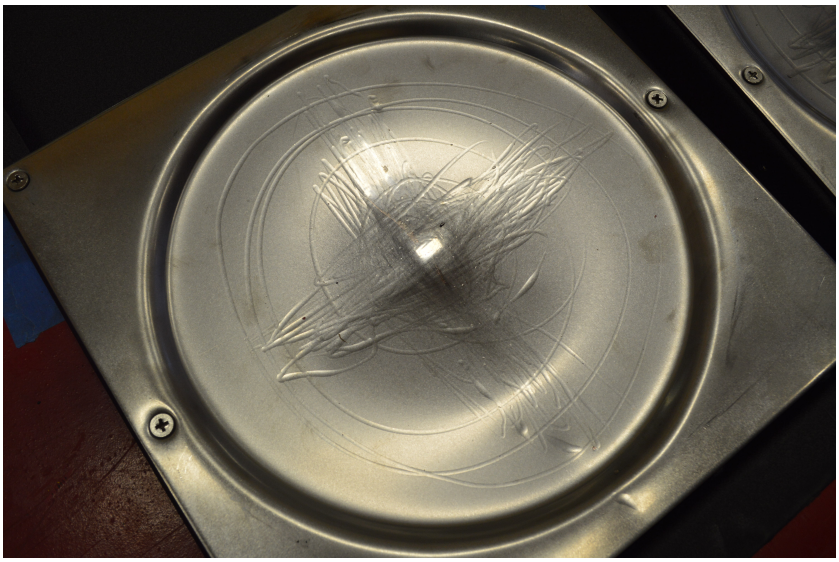

Figure 3.11: Excessive wear on rolling surface of bare steel dish.

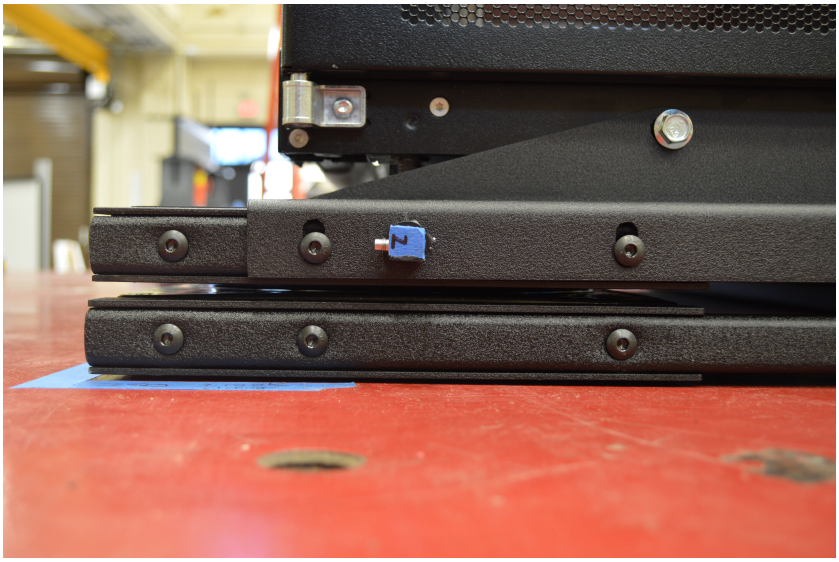

Figure 3.12: Original platform clearance of isolation system.

which was caused from the high contact stress between the rolling ball and the dish. Once rutting occurred, the necessary gap between the top and bottom platforms closed (Figures 3.12 and 3.13), causing platform-to-platform contact which added additional friction to the system and therefore spurious results.

Figure 3.13: Reduced platform clearance of isolation system.

3.3.2 Damped Dishes

Forced response tests were performed with the damped dishes for the single and ganged cabinet setups in the front-to-back and the side-to-side orientations. Figure 3.14 and 3.16 show the time histories for the single cabinet configuration in the front-to-back and side-to-side orientation, respectively. The tests for the ganged cabinet setups (Figures 3.15 and 3.17) exhibited similar results as those of the single cabinet setups. The maximum bearing displacement was not reached in these test.

The durability issues seen in the bare steel dishes did not occur for the elastomeric lined (damped) dishes. The distribution in stress from the lining allowed the steel dish underneath to avoid yielding under the high loads which allowed for the full testing schedule to be completed. With repeat cyclical loading on the damping liner, displacement-acceleration results from the initial test and the final test were plotted to determine if performance of the system changed over the course of the testing period. Figure 3.18 shows acceleration-displacement paths that are nearly identical in shape and magnitude. This is evidence for the high durability of the elastomeric damping

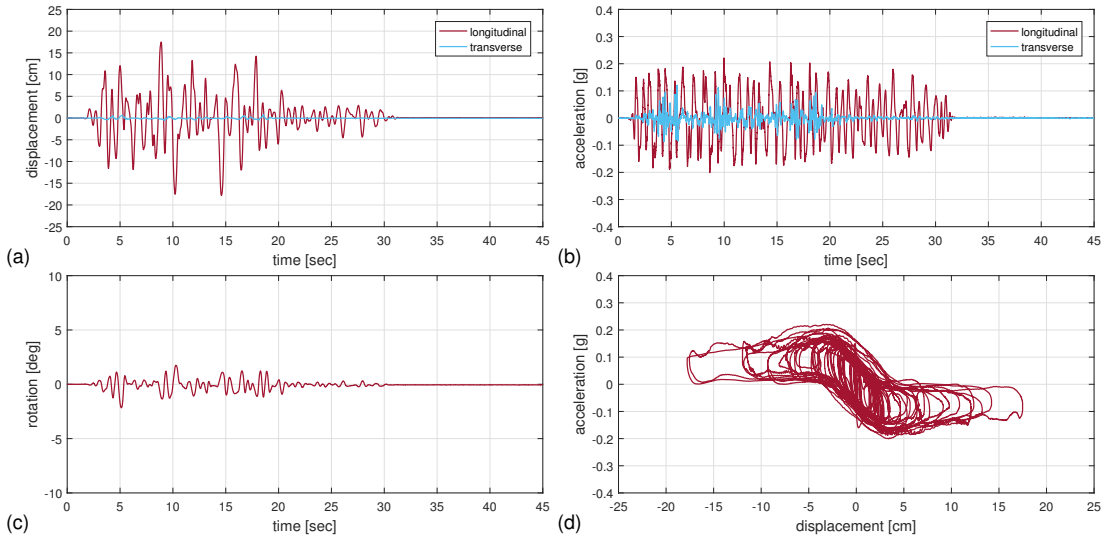

Figure 3.14: Forced response results for single cabinet with damped dishes in the front-to-back orientation at 100% ground motion scaling: (a) longitudinal and transverse displacements, (b) longitudinal and transverse accelerations, (c) rotation, (d) acceleration versus displacement.

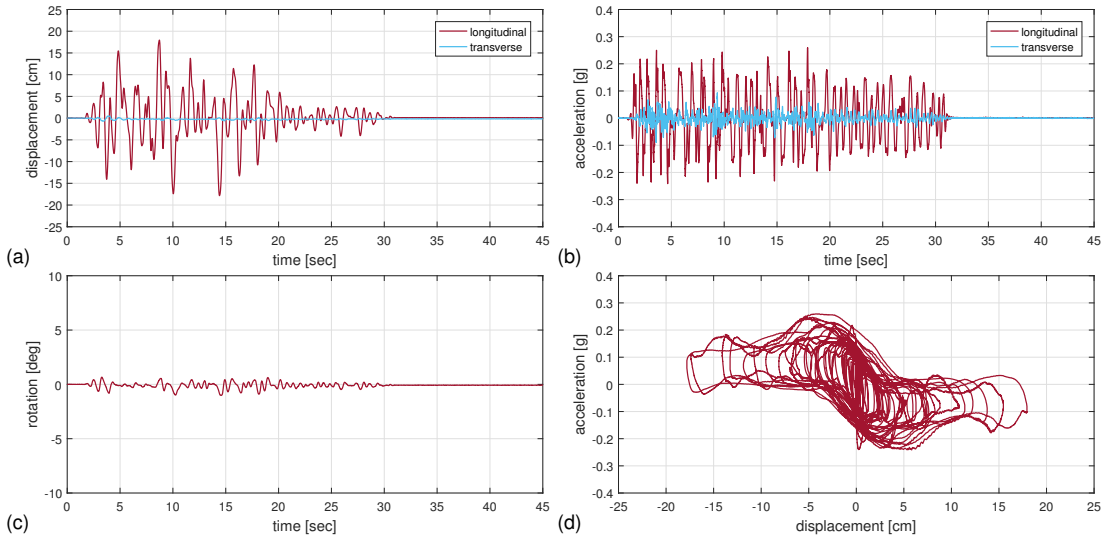

Figure 3.15: Forced response results for ganged cabinets with damped dishes in the front-to-back orientation at 100% ground motion scaling: (a) longitudinal and transverse displacements, (b) longitudinal and transverse accelerations, (c) rotation, (d) acceleration versus displacement.

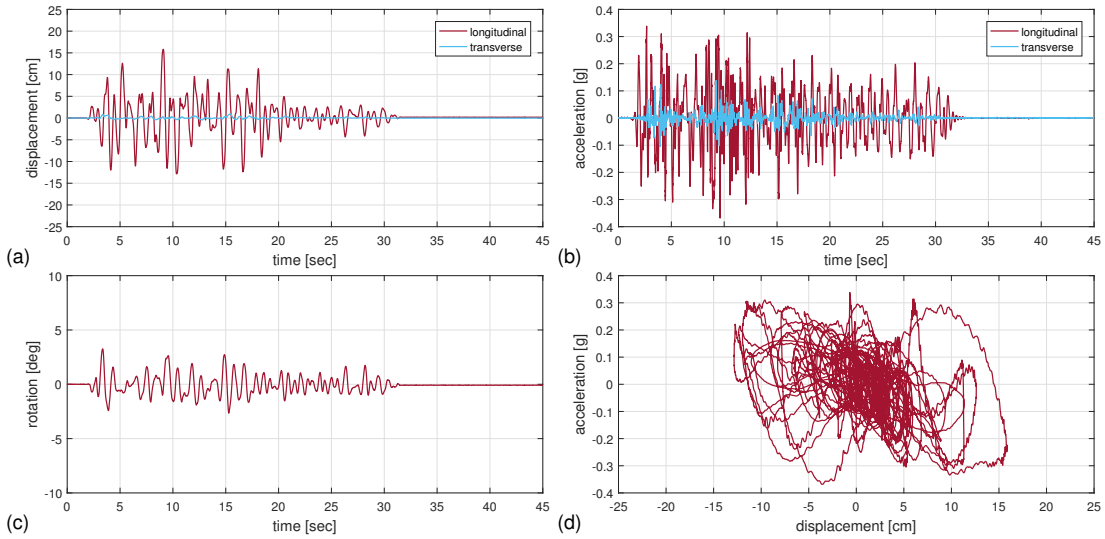

Figure 3.16: Forced response results for single cabinet with damped dishes in the side-to-side orientation at 100% ground motion scaling: (a) longitudinal and transverse displacements, (b) longitudinal and transverse accelerations, (c) rotation, (d) acceleration versus displacement.

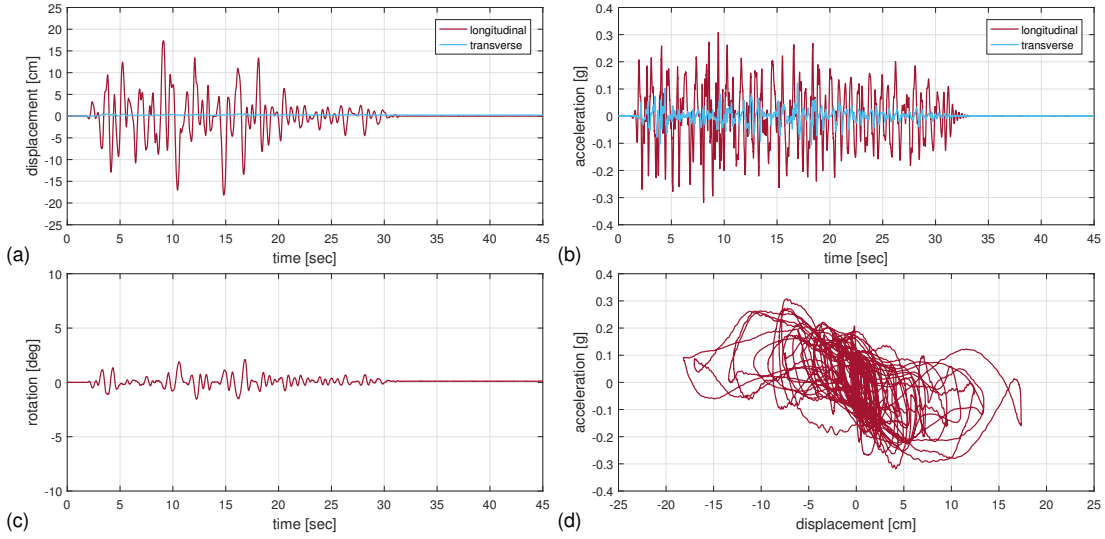

Figure 3.17: Forced response results for ganged cabinets with damped dishes in the side-to-side orientation at 100% ground motion scaling: (a) longitudinal and transverse displacements, (b) longitudinal and transverse accelerations, (c) rotation, (d) acceleration versus displacement.

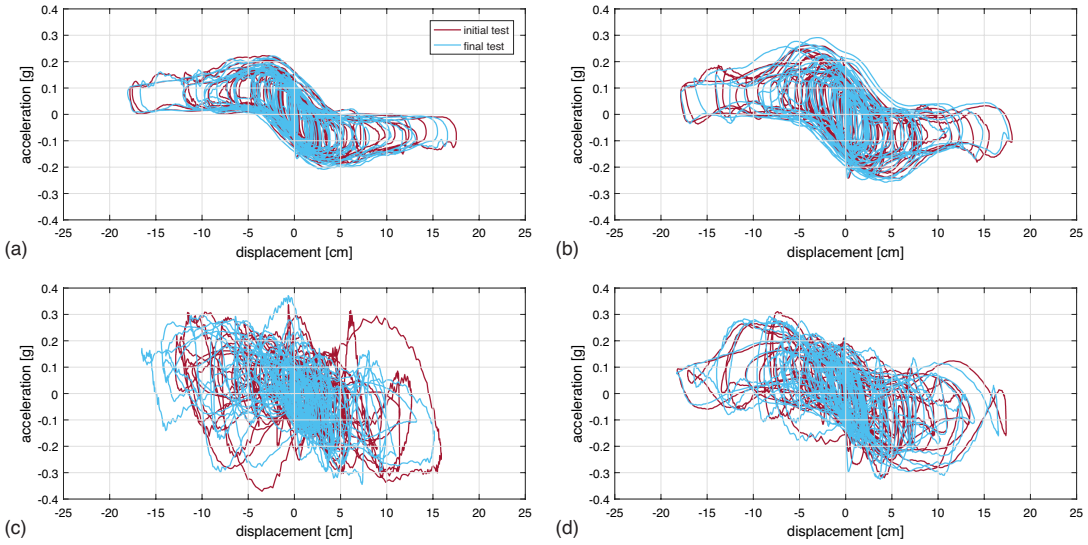

Figure 3.18: Initial and final acceleration displacement results: (a) single cabinet in the front-to-back orientation, (b) ganged cabinets in the front-to-back orientation, (c) single cabinet in the side-to-side orientation, and (d) ganged cabinets in the side-to-side orientation.

liner over repeat loading cycles.

3.4 Incremental Dynamic Analysis

3.4.1 Peak Responses

Figure 3.19 shows the peak responses — (a) longitudinal displacement, (b) transverse displacement, (c) longitudinal acceleration, (d) transverse acceleration, and (e) rotation — for all configurations with the damped dishes subjected to forced excitation. Figure 3.19(a) shows that the peak longitudinal displacements increase linearly with the ground motion scaling with the exception of the single cabinet in the side-to-side orientation at 125% scaling. Figure 3.19(b) shows a general trend of increasing transverse displacements with increasing ground motion scaling.

Figures 3.19(c) and 3.19(d) show only slight increases in longitudinal and transverse accelerations with increasing ground motion scaling. Peak longitudinal accelerations remained between $0.15g$ and $0.20g$ for cases without impact. This nearly constant peak

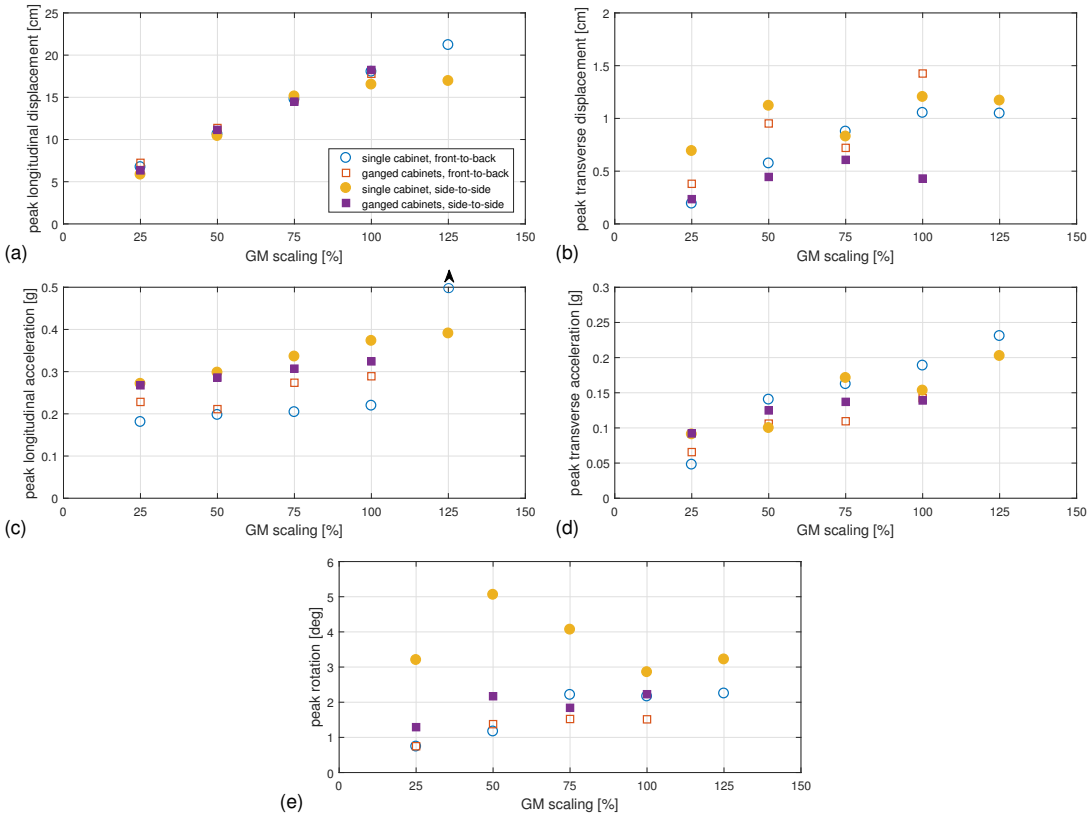

Figure 3.19: Peak responses for various ground motion scaling for the RIS with damped dishes: (a) longitudinal displacement, (b) transverse displacement, (c) longitudinal acceleration, (d) transverse acceleration, and (e) rotation.

acceleration is expected due to the constant slope of the rolling surfaces, as discussed in Section 2.2.2. The accelerations in the longitudinal and transverse directions for the single cabinet in the front-to-back orientation for the 125% ground motion scaling were adversely high as seen in Figure 3.19(c) by the point that was outside the range of the axes. Impact of the rolling balls and lip/edge of the dish occurred in this test.

Figure 3.19(e) shows only slight increases in rotation with increasing ground motion scaling. However, the plot shows much higher rotations for that of the single cabinet in the side-to-side orientation. This highlights the effects of mass eccentricity with respect to the loading direction. The single cabinet, having a smaller moment arm for restoring forces and a smaller mass moment of inertia, could not resist rotation.

3.4.2 Effects of Mass Eccentricity

The experimental case study for a RIS shows that mass eccentricity is a characteristic that considerably effects behavior. The free response tests for a system with supplemental damping (Figures 3.3 and 3.5) show a large increase in rotation with a mass eccentricity. The forced response tests for systems with supplemental damping (Figures 3.14 and 3.16) show similar results with increases in the peak rotational responses as well as overall longer sustained rotational responses under seismic excitation.

From the limited results for the systems without supplemental damping (Figures 3.7 and 3.9), effects of mass eccentricity appear to not be as correlated in dictating the system response for forced excitations. The reason for this is explained from the chaotic nature of lightly damped systems in which unpredictable behavior is seen despite specific loading conditions. When comparing the results for the front-to-back orientation and the side-to-side orientation, the plots show approximately the same peak values. For this reason, the effects of mass eccentricity are less pronounced for RISs with light damping.

3.4.3 Effects of Supplemental Damping

The characteristic that has the most influence on the system response is the damping applied to the rolling surfaces. The free response tests (Figures 3.3 and 3.5) show the high energy absorption ability of the elastomeric damping liner for the rolling surface as the system response decays away much quicker than that of the bare steel system.

For the forced response tests (Figures 3.14 and 3.16), the supplemental damping greatly reduces the displacement demand of the system. This is evident from the fact that none of the tests with the supplemental damping had impacts with the lip/edge of the dishes. The addition of supplemental damping causes slight increase in the accelerations. Also, considering the fact that for the lightly damped systems very high accel-

erations were experienced due the impacts of the rolling balls with the dish's lip/edge, the supplemental damping is beneficial for the system behavior and performance.

3.4.4 Effects of Ganged Cabinets

The effects of a larger platform and increased mass reduce the overall platform rotation as seen in Figure 3.19(e). The increase in moment arm length for the restoring force and the increase in the rotational inertia are the contributing factors.

This effect was highlighted when the rotation time histories for the ganged cabinet setup with bare steel dishes (not shown here) are compared to that of the single cabinet setup [Figures 3.7(d) and 3.9(d)]. For the single cabinet setup, rotations developed in the system in the first couple cycles of motion, whereas it took longer (8 – 10 cycles) for large rotations ($\sim$ 3 – 5°) to develop in the ganged system. This was even more pronounced in the front-to-back loading configuration, which should theoretically not rotate because the inertial load is aligned with the center of rigidity; however, due to imperfections in alignment, rotations ultimately did develop due to the sensitivity of these systems' behavior to slight imperfections (Harvey and Gavin, 2013).

3.4.5 Durability

A RIS is expected to experience repeated loading cycles throughout the lifetime of its use. For this reason durability is of great importance. As seen in Figure 3.11, durability issues were seen for the bare steel dishes due to high contact stresses. These stresses created localized yielding in the dishes creating "ruts" in which the steel balls then wanted to travel through. The modification of the balls' trajectories greatly affects the performance of the isolation system. In addition, the yielding of the dishes caused clearance issues for the platforms, and therefore contact between the upper and lower dished was experienced. This contact caused adverse affects for the acceleration and the displacement of the system.

3.5 Summary

An experimental case study for a RIS consisting of top and bottom steel frames and rolling bearings was performed. Typical computer network cabinets acted as the isolated objects, and the system was experimentally characterized using free and forced response tests. The mass eccentricity, number of cabinets, and damping were varied to determine their effects on the system's behavior. For the free response tests, the system was subjected to an abrupt displacement from the shake table to excite the system. For the forced response tests, the system was subjected to the VERTEQ-II waveform, which is representative of a typical floor motion. The system was tested with a single cabinet and ganged cabinet setups in both the front-to-back and side-to-side orientations.

The results show that a mass eccentricity contributes largely to the rotational response of the isolation system for heavily damped systems, but not for the lightly damped systems, as high rotations were present regardless. The supplemental damping decreased the overall displacement demand of the bearings but increased the acceleration response of the system slightly. Finally, durability issues were seen for the bare steel rolling bearings due to high contact stresses which created ruts in the dishes altering the trajectories and effecting the performance of the system. The damped dishes showed higher durability and repeatable performance over multiple excitations.

Chapter 4

Analytical Model

4.1 Overview

Chapters 2 and 3 detailed an experimental case study which aimed to quantify behavior and performance of rolling-type isolation systems (RISs) under varying system parameters. Often, computer network and telecommunication systems are placed in large data centers where multiple cabinet configurations are used. These configurations can be quite large, and for this reason, performance testing of such systems is not possible due to limitations in shake table size and load capacity. A model is needed to that can predict the performance of large scale systems with varying system parameters. This chapter outlines a mathematical model to predict the response of multi-cabinet array with varying eccentricity and ground motion scaling.

4.2 Model Development

Consider the multi-unit RIS array illustrated in Figure 4.1. Vibration-sensitive equipment, such as electrical cabinets, are rigidly connected to the top frame, and the top frame and equipment are mechanically isolated from the bottom frame via *rolling bearings*. Each rolling bearing is composed of a large, steel ball that rolls between a concave-up lower bowl and a concave-down upper bowl. The bearings are configured in pairs on planks that are connected together with steel bars. For a single isolated cabinet, only

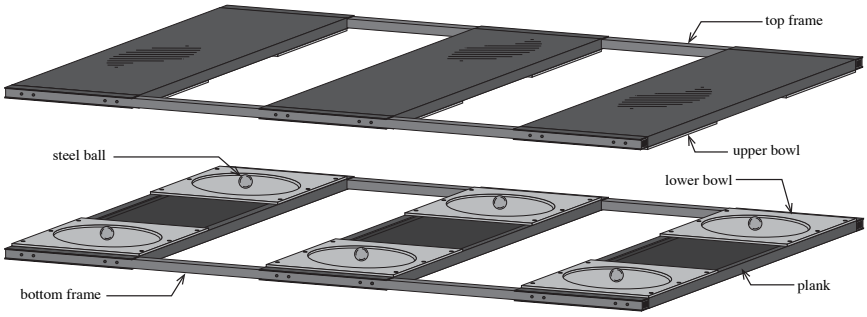

Figure 4.1: Configuration of an RIS array.

two planks (four bearings) are required (see Figure 1.5. For N pieces of equipment, $N + 1$ planks are required; e.g., three planks for two cabinets (Figure 4.1).

4.2.1 Geometry and Notation

Consider the displaced configuration of the RIS illustrated in Figure 4.2. The bearings are numbered $i = 1, \ldots, n$, where the number of bearings, n, depends on the number of isolated cabinets, N; i.e., $n = 2(N + 1)$. The X_t–Y_t coordinates of the ith bowl center are given by $\boldsymbol{\xi}_i = \{x_i, y_i\}_\mathrm{t}^\mathsf{T}$, which is dictated by the frame geometry.* The planks are spaced at l_x on centers, with the bearings spaced at l_y.

The N isolated cabinets are assumed to be identical, each having a mass m that is eccentrically located at (e_x, e_y) relative to centroid of the two supporting planks. The total mass of the isolated equipment $M = N \cdot m$, which is eccentrically located at $\boldsymbol{e} = \{e_x, e_y\}_\mathrm{t}^\mathsf{T}$ from the top-frame centroid O. The mass moment of inertia about the top-frame centroid is I_O. The top frame undergoes rotation $\theta(t)$ and translational displacement $\boldsymbol{u}(t) = \{u_x(t), u_y(t)\}_\mathrm{b}^\mathsf{T}$ relative to the bottom frame. The bottom frame is excited by translational disturbance $\boldsymbol{u}_\mathrm{g}(t) = \{u_{\mathrm{g}x}(t), u_{\mathrm{g}y}(t)\}_\mathrm{b}^\mathsf{T}$.

The gravitational restoring forces in the system are attributed to changes in the heights at the bearings, which depend on the top frame's displacement and rotation,

*In this chapter, vectors are represented by boldface minuscule letters, and matrices by majuscule letters; the superscript 'T' denotes the transpose; and the subscripts 't' and 'b' are used to indicate the coordinate system in which positions are measured, namely top $(X_\mathrm{t}, Y_\mathrm{t})$ and bottom $(X_\mathrm{b}, Y_\mathrm{b})$.

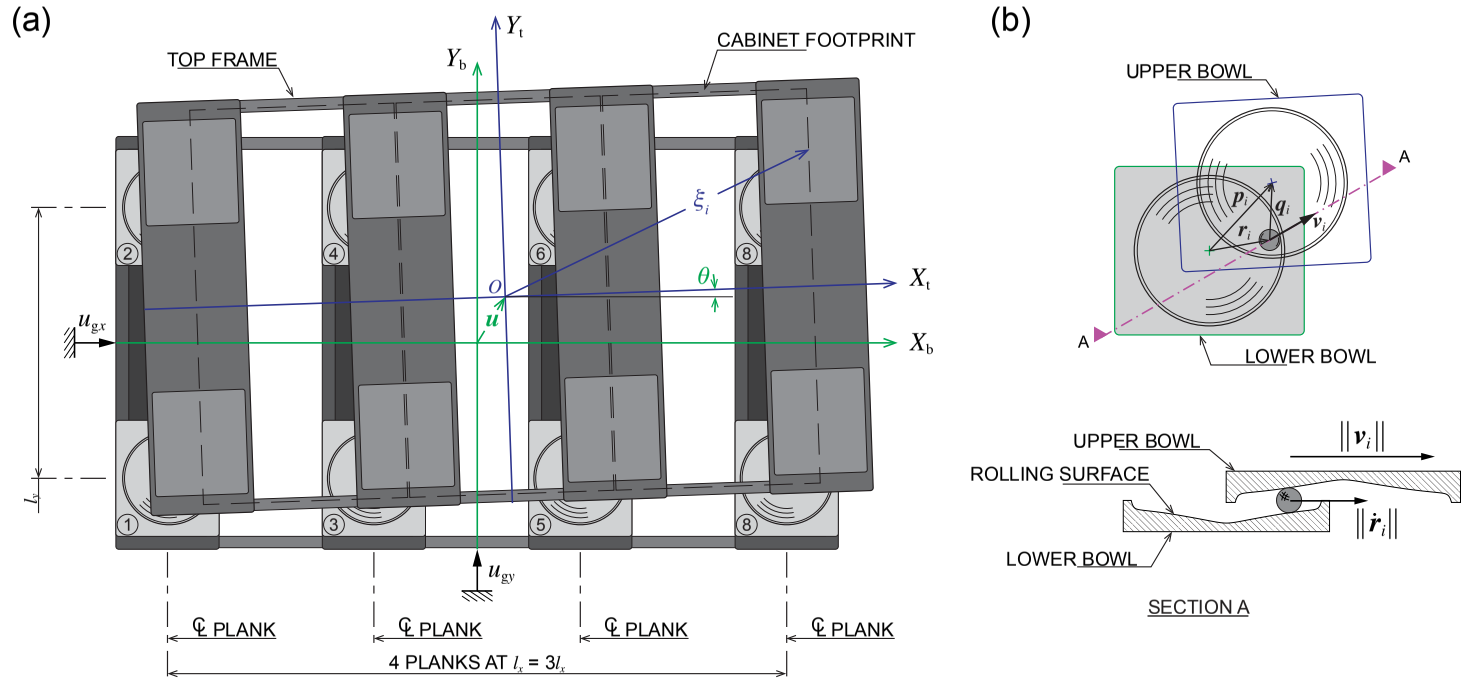

Figure 4.2: Geometry and notation of a rolling isolation system ($N = 3$): (a) displaced configuration; (b) kinematics of rolling balls.

as well as the balls' locations. As seen in Figure 4.2(b), the balls' locations with respect to the centers of the lower and upper bowls are $\boldsymbol{r}_i(t) = \{r_{xi}(t), r_{yi}(t)\}_{\mathrm{b}}^{\mathsf{T}}$ and $\boldsymbol{q}_i(t) = \{q_{xi}(t), q_{yi}(t)\}_{\mathrm{b}}^{\mathsf{T}}$, and the center-to-center displacement is $\boldsymbol{p}_i(t) = \{p_{xi}(t), p_{yi}(t)\}_{\mathrm{b}}^{\mathsf{T}} \equiv \boldsymbol{u}(t) + (\mathbf{R}_{\theta(t)} - \mathbf{I})\,\boldsymbol{\xi}_i$ where $\mathbf{I}$ is the identity matrix and

$$\mathbf{R}_{\theta(t)} = \begin{bmatrix} \cos\theta(t) & -\sin\theta(t) \\ \sin\theta(t) & \cos\theta(t) \end{bmatrix}$$

All the bowls are assumed axisymmetric with radius-dependent bowl-shape function $\eta(r)$. The height of the top frame at the center of the ith upper bowl is the sum of contributions from the lower and upper bowls, given by

$$h_i \equiv h_i(u_x, u_y, \theta, \boldsymbol{r}_i; t) = \eta\big(r_i(t)\big) + \eta\big(q_i(t)\big) \tag{4.1}$$

where $r_i(t) = \|\boldsymbol{r}_i(t)\|$ and $q_i(t) = \|\boldsymbol{q}_i(t)\|$.

4.2.2 Kinematics of Rolling Balls

The ball coordinates $\boldsymbol{r}_i(t)$ evolve according to a set of nonholonomic constraints prescribed by the condition of rolling without slipping between non-parallel surfaces (Harvey and Gavin, 2013). The kinematic constraint, relating the the ball velocities $\dot{\boldsymbol{r}}_i(t)$ to the relative velocities of the upper bowls at the ball locations, depends upon the slopes of the upper and lower bowls. For shallow bowls (i.e., small $\eta'(r)$), the nonholonomic constraint can be approximated by the condition that the velocity of the ball center is half of the relative velocity across the isolation system (Harvey et al., 2014). The ball velocity is in the direction of this relative velocity,

$$\dot{\boldsymbol{r}}_i(t) = \tfrac{1}{2}\Big\{\dot{\boldsymbol{u}}(t) + \dot{\theta}(t)\,\mathbf{D}\,[\boldsymbol{\xi}_i + \boldsymbol{r}_i(t) - \boldsymbol{u}(t)]\Big\}, \qquad (i = 1, ..., n) \tag{4.2}$$

where the cross product $\dot{\theta}\mathbf{k} \times (\boldsymbol{\xi}_i + \boldsymbol{r}_i - \boldsymbol{u})$ is performed using the matrix

$$\mathbf{D} = \begin{bmatrix} 0 & -1 \\ 1 & 0 \end{bmatrix}$$

The $2n$ non-linear first-order ordinary differential equations (4.2) prescribe the evolution of the n balls in the X_b–Y_b plane. Initial conditions $\boldsymbol{r}_i(0)$ must be specified.

4.2.3 Equations of Motion

Approaching this problem by using Lagrange's equation, expressions for the kinetic energy $\mathcal{T}$ and potential energy $\mathcal{V}$ need to be found. The kinetic energy $\mathcal{T}$ is given by

$$\mathcal{T}(\dot{u}_x, \dot{u}_y, \theta, \dot{\theta}; t) = \tfrac{1}{2} M \mathbf{v}_G^\mathsf{T} \mathbf{v}_G + \tfrac{1}{2} I_G \dot{\theta}^2 \tag{4.3}$$

in which $\mathbf{v}_G$ is the absolute (horizontal) velocity of the center of gravity G given by

$$\mathbf{v}_G(t) = \dot{\boldsymbol{u}}_\mathrm{g}(t) + \dot{\boldsymbol{u}}(t) + \dot{\theta}(t) \mathbf{R}'_{\theta(t)} \boldsymbol{e} \tag{4.4}$$

where $\mathbf{R}'_\theta = \frac{\partial}{\partial \theta} \mathbf{R}_\theta$, and $I_G = I_O + M(e_x^2 + e_y^2)$. The potential energy $\mathcal{V}$ is due to the change in height of the isolated cabinets' centers of mass. The change in height of a cabinet's center of mass can be interpolated from the heights h_i [Equation (4.1)] of the four bowls on the supporting planks (Harvey and Gavin, 2013). The interpolated height at the center of mass is given by

$$\hat{h}_j = a_1 h_{2j-1} + a_2 h_{2j} + a_3 h_{2j+1} + a_4 h_{2j+2} \tag{4.5}$$

where, in terms of the nondimensional eccentricities $\varepsilon_x = e_x \div l_x$ and $\varepsilon_y = e_y \div l_y$,

$$\begin{Bmatrix} a_1 \\ a_2 \\ a_3 \\ a_4 \end{Bmatrix} = \frac{1}{4} \begin{bmatrix} 1 & -2 & -2 & 4 \\ 1 & -2 & 2 & -4 \\ 1 & 2 & -2 & -4 \\ 1 & 2 & 2 & 4 \end{bmatrix} \begin{Bmatrix} 1 \\ \varepsilon_x \\ \varepsilon_y \\ \varepsilon_x \varepsilon_y \end{Bmatrix} \tag{4.6}$$

which is then used to express the potential energy,

$$\mathcal{V}(u_x, u_y, \theta, \boldsymbol{r}_i, \ldots, \boldsymbol{r}_n; t) = \sum_{j=1}^{N} mg\hat{h}_j \tag{4.7}$$

where g is gravitational acceleration. For $N = 1$ (single cabinet) the contribution from the four bearings is the same, but for $N > 1$ (multiple cabinets) the contribution from

the bearings on the exterior planks ($i = 1, 2, n-1, n$) is less than that from the bearings on the interior planks ($i = 3, 4, ..., n-2$), as the interior planks have twice the tributary area. Equation (4.7) can hence be written in the form

$$\mathcal{V} = \sum_{i=1}^{n} mgb_i h_i \tag{4.8}$$

where the weighting coefficients for the exterior bearings are $b_1 = a_1$, $b_2 = a_2$, $b_{n-1} = a_3$, $b_n = a_4$ and for the interior bearings are

$$b_i = \begin{cases} a_1 + a_3 : & 3 \le i \le n-3,\ i \text{ odd} \\ a_2 + a_4 : & 4 \le i \le n-2,\ i \text{ even} \end{cases}$$

Applying the fundamental nonholonomic form of Lagrange's equation (Greenwood, 2006, Eq. (2.48)), the equations of motion of the platform coordinates (u_x, u_y, θ), taking into account the constraint (4.2), are as follows:

$$M\left[\ddot{\boldsymbol{u}}_{\mathrm{g}}(t) + \ddot{\boldsymbol{u}}(t) + \ddot{\theta}(t)\,\mathbf{R}'_{\theta(t)}\boldsymbol{e} - \left(\dot{\theta}(t)\right)^2 \mathbf{R}_{\theta(t)}\boldsymbol{e}\right] + \sum_{i=1}^{n} mgb_i\eta'\!\left(q_i(t)\right)\hat{\boldsymbol{q}}_i(t) + \sum_{i=1}^{n}\tfrac{1}{2}\boldsymbol{\lambda}_i = \mathbf{0} \tag{4.9a}$$

$$M\left[\ddot{\boldsymbol{u}}_{\mathrm{g}}(t) + \ddot{\boldsymbol{u}}(t)\right]^{\mathsf{T}}\mathbf{R}'_{\theta(t)}\boldsymbol{e} + I_O\,\ddot{\theta}(t) + \sum_{i=1}^{n} mgb_i\eta'\!\left(q_i(t)\right)\hat{\boldsymbol{q}}_i^{\mathsf{T}}(t)\mathbf{R}'_{\theta(t)}\boldsymbol{\xi}_i + \sum_{i=1}^{n}\tfrac{1}{2}\boldsymbol{\lambda}_i^{\mathsf{T}}\mathbf{D}\left[\boldsymbol{\xi}_i + \boldsymbol{r}_i(t) - \boldsymbol{u}(t)\right] = 0 \tag{4.9b}$$

where $\boldsymbol{q}_i(t) = \boldsymbol{p}_i(t) - \boldsymbol{r}_i(t)$, as in Figure 4.2; the over-hat indicates the unit vector, e.g., $\hat{\boldsymbol{r}}_i \equiv \boldsymbol{r}_i/\|\boldsymbol{r}_i\|$; and $\boldsymbol{\lambda}_i$ are the Lagrange multipliers enforcing Equation (4.2). The multipliers are found by applying Lagrange's equation to the ball coordinates $\boldsymbol{r}_i$:

$$\boldsymbol{\lambda}_i = \mathbf{f}_i^{\mathrm{d}} + mgb_i\left[\eta'\!\left(r_i(t)\right)\hat{\boldsymbol{r}}_i(t) - \eta'\!\left(q_i(t)\right)\hat{\boldsymbol{q}}_i(t)\right] \tag{4.10}$$

where the damping forces $\mathbf{f}_i^{\mathrm{d}}$ counteract the balls' motion. The form of $\mathbf{f}_i^{\mathrm{d}}$ depends on the ball–bowl interface, which can range from lightly damped (steel-on-steel (Harvey and Gavin, 2013)) to heavily damped (rubber coated balls (Tsai et al., 2010) or rubber coated bowls (Harvey et al., 2014; Foti et al., 2013; Zéhil and Gavin, 2013; Qiu, 2006)).

Substituting Equation (4.10) into Equation (4.9) and combining terms,[†] the equations of motion of the platform coordinates can be rewritten in matrix form:

$$\begin{bmatrix} M\mathbf{I} & M\mathbf{D}\mathbf{R}_{\theta(t)}\boldsymbol{e} \\ M(\mathbf{D}\mathbf{R}_{\theta(t)}\boldsymbol{e})^{\mathsf{T}} & I_O \end{bmatrix} \begin{Bmatrix} \ddot{\boldsymbol{u}}(t) \\ \ddot{\theta}(t) \end{Bmatrix} + \begin{Bmatrix} -M(\dot{\theta}(t))^2\,\mathbf{R}_{\theta(t)}\boldsymbol{e} \\ 0 \end{Bmatrix} + \frac{1}{2}\sum_{i=1}^{n} \begin{bmatrix} \mathbf{I} \\ (\boldsymbol{\xi}_i + \boldsymbol{r}_i(t) - \boldsymbol{u}(t))^{\mathsf{T}}\mathbf{D}^{\mathsf{T}} \end{bmatrix} \left(\mathbf{f}_i^{\mathrm{d}} + \mathbf{f}_i^{\mathrm{L}} + \mathbf{f}_i^{\mathrm{U}}\right) = -\begin{bmatrix} M\mathbf{I} \\ M(\mathbf{D}\mathbf{R}_{\theta(t)}\boldsymbol{e})^{\mathsf{T}} \end{bmatrix} \ddot{\boldsymbol{u}}_{\mathrm{g}}(t) \quad (4.11)$$

where the lower and upper gravitational restoring forces are defined respectively by

$$\mathbf{f}_i^{\mathrm{L}} = mgb_i\eta'(r_i(t))\,\hat{\boldsymbol{r}}_i(t) \quad (4.12a)$$

$$\mathbf{f}_i^{\mathrm{U}} = mgb_i\eta'(q_i(t))\,\hat{\boldsymbol{q}}_i(t) \quad (4.12b)$$

Equations (4.2) and (4.11) comprise the full set of system dynamics, which must be integrated simultaneously. The equations of motion for the platform coordinates [Equation (4.11)] represent an extension of a previously developed model that was valid only for the case of $N = 1$ ($n = 4$) (Harvey and Gavin, 2013; Harvey et al., 2014) to be able to accommodate an arbitrary number of isolated cabinets ($N > 1$). Upon closer inspection, Equation (4.11) reduces to those previous models if N is taken to be 1.

4.2.4 Considered Geometries

The mathematical model developed in the preceding section is used to assess the performance of multi-unit RIS arrays under parametric variation. The cabinet and RIS geometries considered in the numerical simulations are described below. These geometries correspond to actual network cabinets and RISs tested in the lab, which are representative of a typical installation that would be seen in the field.

A typical bowl-shape function $\eta(r)$ is conical with a spherical central region and lip at the edge (Vargas and Bruneau, 2009; Harvey and Kelly, 2016). For the numerical simulations, the following bowl gradient, which was calibrated in a previous study

[†]Note that $\mathbf{R}'_\theta \equiv \mathbf{D}\mathbf{R}_\theta$, $\mathbf{R}_\theta\boldsymbol{\xi}_i \equiv \boldsymbol{\xi}_i + \boldsymbol{r}_i - \boldsymbol{u} - \boldsymbol{q}_i$, and $\hat{\boldsymbol{q}}_i^{\mathsf{T}}\mathbf{D}\boldsymbol{q}_i \equiv 0$.

(Harvey, 2015), was used:

$$\eta'(r) = \begin{cases} \dfrac{r}{\sqrt{R^2 - r^2}} & \text{if } r \leq r^* \\ s & \text{if } r^* < r \leq r_{max} \\ s_1(r - r_{max}) + s & \text{if } r > r_{max} \end{cases} \tag{4.13}$$

where r is the location of the ball relative to the center of the bowl and r_{max} is the radius of the bowl; R is the radius of the spherical region in the center of the bowl and r^* represents the location where the spherical region becomes conical; s is the slope of the conical section of the bowl, and s_1 is the slope of the lip/edge of the bowl. Specific values for these variables are given in Chapter 5.

4.2.5 Considered Damping

Commonly, the bowls and balls are both made of stainless steel, i.e., *lightly damped*, which is considered here. For a lightly damped RIS (Harvey and Gavin, 2013), linear viscous damping is appropriate: $\mathbf{f}_i^{\mathrm{d}} = c_i \dot{\boldsymbol{r}}_i$ where c_i is the mass-dependent damping coefficient. The damping coefficient c_i depends on the normal force carried by each ball. Assuming the mass of each piece of equipment is the same (m), then the balls on the interior planks ($i = 3, \ldots, n-2$) carry twice the weight as the balls on the exterior planks ($1 = 1, 2, n-1, n$), hence

$$c_i = \begin{cases} 0.000229m^2 + 0.02884m, & i = 1, 2, n-1, n \\ 0.000229(2m)^2 + 0.02884(2m), & i = 3, \ldots, n-2 \end{cases} \tag{4.14}$$

4.3 Summary

An analytical model for a multi-unit RIS has been developed, extending previous models for a single platform and mass system. The model was derived using Lagrange's equation, which required relationships for the kinematics of the upper platform relative to the lower platform and kinematics of the ball relative to the upper and lower

bowls. The kinetic energy of the system was found using the translation and rotation of the platform and attached mass, and the potential energy was derived using the vertical change in height of the top platform relative to the bottom platform, which is a function of the ball locations in the bowls. The change in height of the center of the cabinet was interpolated from the change in height across the supporting bearings. The bowl shape dictates the relationship between horizontal displacement and changes in vertical position, which results in restoring forces that depend on the slope of the bowl shape. Using Lagrange's equation the state variables and equations of motion were derived and the bowl profile and damping were proposed. The equations of motion are used in Chapter 5 to perform a parametric study of RISs to quantify the performance over a range of operating conditions.

Chapter 5

Numerical Results

5.1 Overview

Chapter 4 detailed a mathematical model which predicts the dynamics of the rolling-type isolation system (RIS) of various size and mass. The model requires specific geometric, inertial, and damping values. This chapter outlines the considered RIS geometries, including the platform dimensions and the bowl profile geometry, as well as the isolated cabinet properties. Then, the results of an extensive parametric study utilizing the calibrated model are presented.

5.2 Model Simulation

The mathematical model developed in Chapter 4 is nonlinear with coupled equations of motion with no explicit solution. The model is therefore numerically solved. The model is implemented into Matlab and the complete set of equations that describe the evolution of the system are solved simultaneously using the ode45 solver in Matlab. This requires representing the equations of motion [Equations (4.2) and (4.9)] in state-space form:

$$\frac{d}{dt}\mathbf{x}(t) = \mathbf{f}(\mathbf{x}, \ddot{u}_{gx}, \ddot{u}_{gy}; t) \tag{5.1}$$

where the inputs are the ground accelerations $\ddot{u}_{gx}(t)$ and $\ddot{u}_{gy}(t)$. The states of the system are the platform translational and rotational displacements and velocities and the ball

translational displacements:

$$\mathbf{x}(t) = \left[u_x(t) \;\; u_y(t) \;\; \theta(t) \;\; \dot{u}_x(t) \;\; \dot{u}_y(t) \;\; \dot{\theta}(t) \;\; r_{1x}(t) \;\; r_{1y}(t) \;\; \cdots \;\; r_{nx}(t) \;\; r_{ny}(t)\right]^{\mathsf{T}} \tag{5.2}$$

The states are initialized to zero for all cases, i.e., $\mathbf{x}(0) = \mathbf{0}$. The ode45 solver uses a 4th-order Runge-Kutta method with an adaptive time step. Tight error tolerances, both relative and absolute, were used to ensure numerical accuracy.

5.3 Considered Setup

The considered setup is modeled after the experimental setup discussed in Chapters 2 and 3. The necessary dimensions and other properties of the network cabinets and isolation platform are given here.

Network cabinet The dimensions of each isolated network cabinet are 2026-mm (H) × 1200-mm (D) × 700-mm (W), with a mass m of 680 kg. The center of mass (G) of the experimental cabinets was concentric about the width ($e_x = 0$) and 122 mm forward-of-center in the cabinet depth ($e_y = 122$ mm); G was 740 mm from the base. The mass moment of inertia about the cabinet's centroid is assumed to be

$$I_O = m(W^2 + D^2)/12 + m(e_x^2 + e_y^2) \tag{5.3}$$

which gives 119.5 kg-m^2 for the experimental system and 109.4 kg-m^2 for no mass eccentricity. Varying numbers of isolated cabinets are considered: $N = 1$, 2, 4, and 8.* The determination of I_O for the ganged system must consider the spacing of the cabinets and their position relative to the top-frame centroid O (i.e., parallel axis theorem must be used). For the number of cabinets considered, the moments of inertia are 126.5, 455.5, 2531.1, and 18022 kg-m^2, respectively.

*For more than 8 isolated cabinets, ganged rolling isolation systems are impractical, and an isolated raised floor would be better suited (Lambrou and Constantinou, 1994).

Isolation platform The bowl spacing, as denoted in Figure 4.2(a), are taken to be $l_x = 75$ cm and $l_y = 100$ cm.

5.4 Free Response Calibration

The mathematical model [Equation (4.9)] requires the bowl geometry $\eta(r)$ and the damping model to be specified. The former dictates the stiffness of the RIS, and the latter can be assumed to be linear viscous. The stiffness and damping properties of the RIS are calibrated to the experimental data presented in Chapter 3, which is described below.

5.4.1 Bowl Geometry

The mathematical model for a RIS with N cabinets was calibrated to the experimental free response tests described in Chapter 3. Experimental free response was achieved by exciting the RIS and cabinets with an abrupt motion from the shake table at a velocity of 75 cm/s and a total displacement of 15 cm. The longitudinal displacement and acceleration responses from these tests (Figures 3.1 and 3.2) are used to calibrate the bowl geometry. The experimentally measured ground accelerations from the pulse tests are applied to the mathematical model from Chapter 4 and the response was simulated in Matlab.

The gravitational restoring forces given by Equation (4.12) depend explicitly on the bowl gradient $\eta'(r)$. The form of the gradient is taken to be Equation (4.13). Nominal values for the radius R, slope s, and maximum radius r_{max} are 12.7 cm, 0.1, and 9 cm, respectively (Vargas and Bruneau, 2009). The nominal acceleration in the horizontal direction of the conical section of the rolling surface is approximately $0.1g$ (Harvey, 2015). However, after initial numerical trials, the stiffness was found to be high and therefore the periods of the numerical results were lower than that of the experimental trials. The slope of the conical section of the bowl was modified in order to match

the periods of the systems. A slope of 0.095 provided good agreement with the period of the experimental results; the nominal radius $R = 12.7$ cm gave good agreement with the acceleration-displacement at small displacements. The following expresses the calibrated slope of the bowl profile:

$$\eta'(r) = \begin{cases} \dfrac{r}{\sqrt{12.7^2 - r^2}} & \text{if } r \leq 1.201 \\ 0.095 & \text{if } 1.201 < r \leq 9 \\ 100(r - 9) + 0.095 & \text{if } r > 9 \end{cases} \tag{5.4}$$

where r is measured in cm. At a ball displacement $r > 9$ cm (i.e, a bearing displacement $u > 18$ cm), impact occurs with the lip/edge of the bowl. In order to simulate the impact, a high stiffness is used. A value of $s_1 = 100$ produced the acceleration spikes needed for impact, but also preserved model stability for grazing impacts of the lip/edge.

5.4.2 Damping

Next, the damping coefficient c_i for the theoretical damping model is determined. The expression for the damping coefficient given by Equation (4.14) was fit to experimental data (Harvey and Gavin, 2013), but only considered a peak mass of 635.45 kg, of which one fourth is assigned to each bowl. For an expanded array of cabinets, the interior bowls receive one half the mass, which is higher than the range of mass for which the model was calibrated. Using the model, the damping in the system was found to be excessive producing unrealistic dissipation. For this reason, the damping coefficient was fit to the free response tests, matching peaks and decay rate, and validated against the forced response tests. For the tested case, the following was found produce results that match the experimental responses:

$$c_i = \begin{cases} 0.000229m^2 + 0.02884m, & i = 1, 2, n-1, n \\ 2.5(0.000229m^2 + 0.02884m), & i = 3, \ldots, n-2 \end{cases} \tag{5.5}$$

where m is measured in kg. The exterior bowls had a damping of 139.5 N-s/m which

matches the value given by Eq. (4.14), whereas and interior bowls had a damping of 348.7 N-s/m[†].

5.4.3 Results

Figures 5.1 and 5.2 show the responses for the single ($N = 1$) and ganged ($N = 2$) cabinet setups, respectively. The numerical results for the single cabinet show good agreement until approximately 5 cycles at which point the experimental energy in the longitudinal direction transitioned into the transverse and rotational modes, which the numerical model does not account for. The numerical results for the ganged cabinets show good agreement with the experimental results for the entirety of the test as very little of the longitudinal energy transitioned into the transverse and rotational modes.

5.5 Forced Response Results

5.5.1 Model Validation

The calibrated model from the free response tests was validated against forced response tests using the VERTEQ-II Zone-4 waveform. Figure 2.6 shows the input acceleration, velocity, displacement, and spectrum the VERTEQ-II record as well as the required response spectrum (RSS) to meet the Zone-4 criteria and the actual shaker table spectrum. For the experimental results, the VERTEQ-II record was input into the shake table and inherently does not produce the exact input record. For the parametric study, the VERTEQ-II record was used due to the necessary scaling of the ground motions.

Four different configurations were experimentally tested and used for the model validation:

- single cabinet with ground motions in the front-to-back direction

[†]This value would vary depending on the system used, and it is recommended that the theoretical model from Section 4.2.5 be used if no experimental data is available.

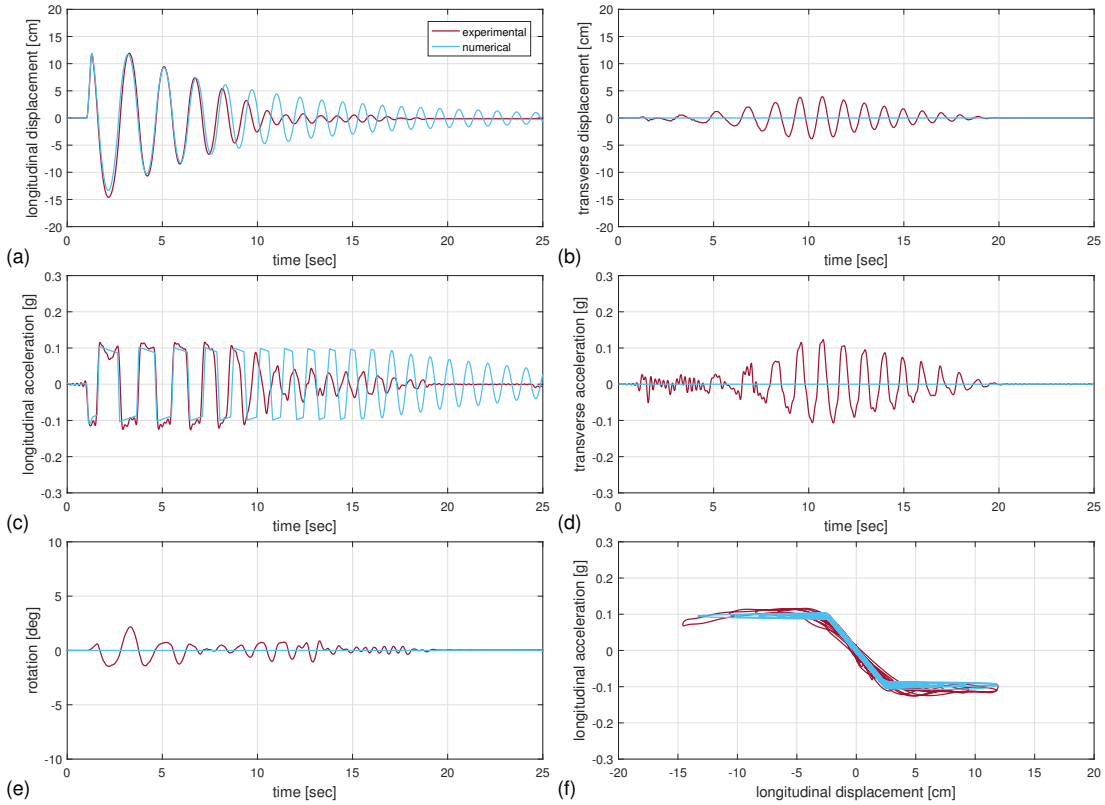

Figure 5.1: Experimental and numerical free response results for single cabinet with bare steel dishes in the front-to-back orientation: (a) longitudinal displacement, (b) transverse displacement, (c) longitudinal acceleration, (d) transverse acceleration, (e) rotation, and (f) acceleration versus displacement.

- two ganged cabinets with ground motions in the front-to-back direction
- single cabinet with ground motions in the side-to-side direction
- two ganged cabinets with ground motions in the side-to-side direction

Figures 5.3, 5.4, 5.5, and 5.6 show the time histories of the experimental and numerical results for these cases. It can be seen that the model has good agreement with the experimental results, predicting peak responses and frequencies, up until the point of impact at which point the criteria for failure is met. The results for the numerical model after impact are considered invalid as the model does not account for the energy loss of the impact and produces high restoring forces due to the elastic action of the stiffness

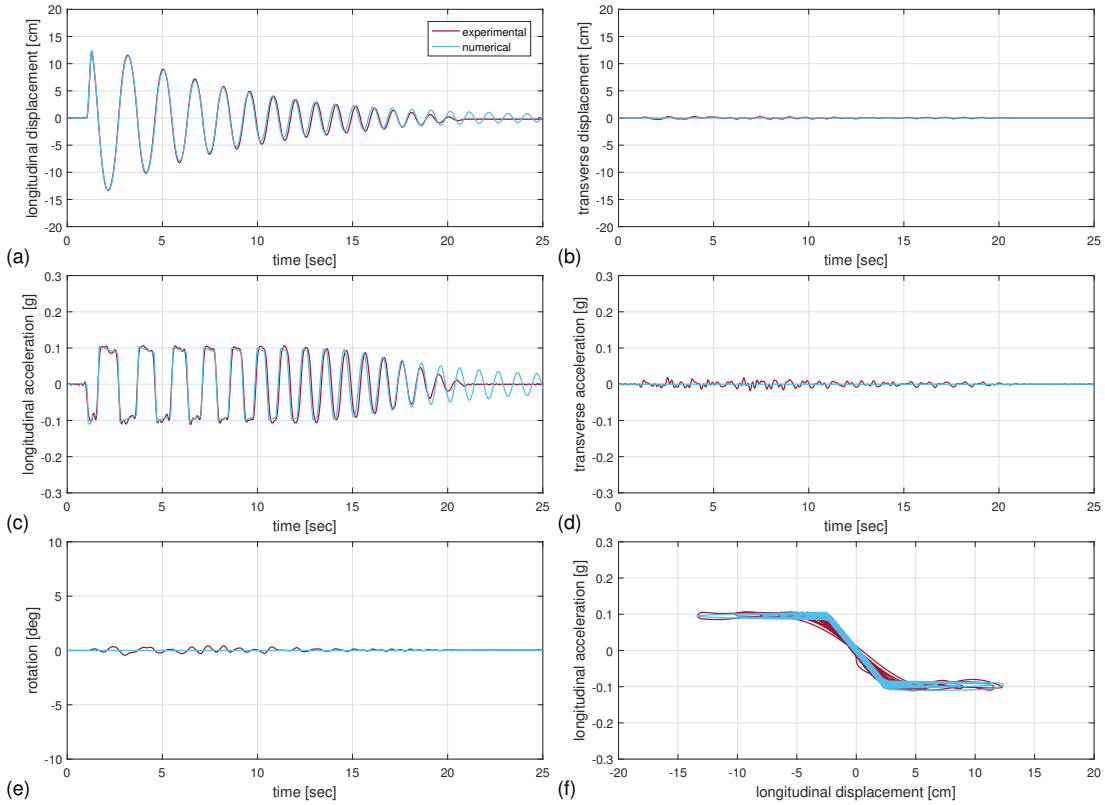

Figure 5.2: Experimental and numerical free response results for ganged cabinets with bare steel dishes in the front-to-back orientation: (a) longitudinal displacement, (b) transverse displacement, (c) longitudinal acceleration, (d) transverse acceleration, (e) rotation, and (f) acceleration versus displacement.

which acts at the edge/lip of the bowl [see Equation (4.13)]. In actuality, these forces are not elastic and would not be behave as seen in the model. However, the purpose of the model is to capture when impacts occur, as opposed to the exact value of the high accelerations sustained at impact.

5.5.2 Performance Criteria

Vibration-sensitive equipment such as electrical cabinets are typically rated according to peak accelerations they can sustain and remain operational. Cabinets holding sensitive electronics nominally remain operational at $0.25g$ shaking and $0.33g$ impact load. Hence, the performance of the multi-unit RIS arrays will be assessed in terms of peak total acceleration sustained by the isolated equipment.

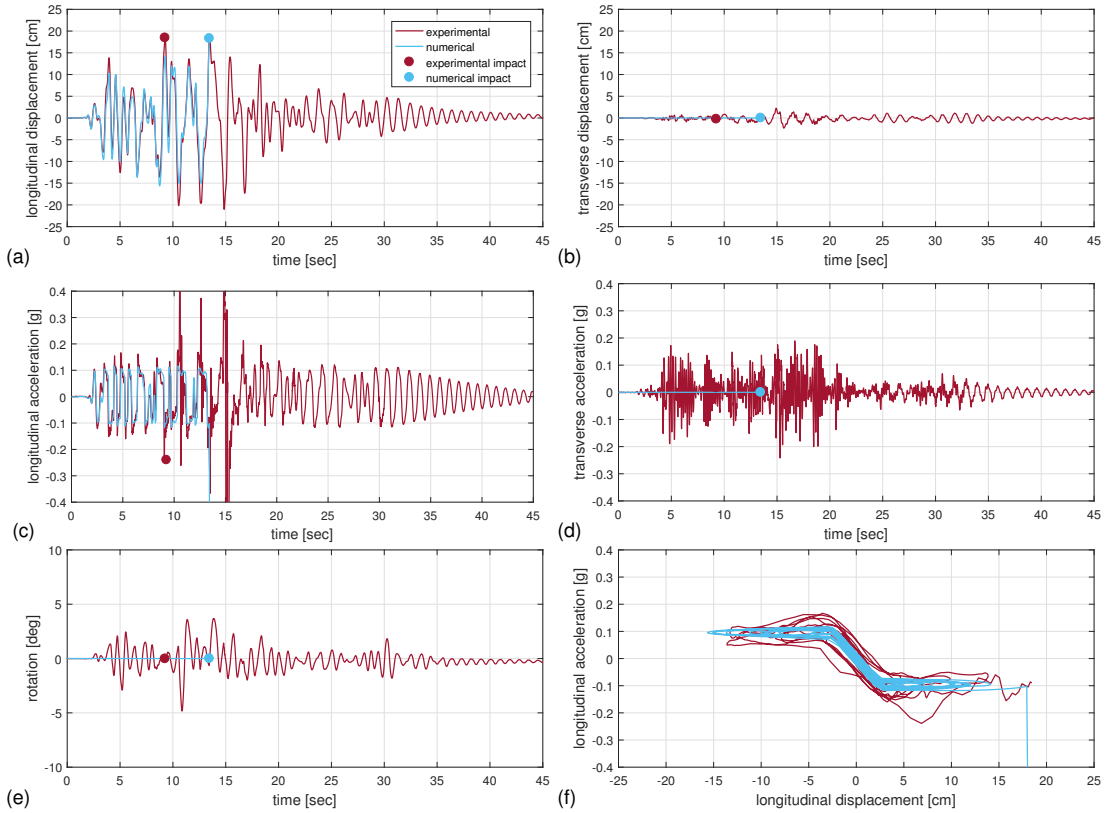

Figure 5.3: Experimental and numerical forced response results for single cabinet with bare steel dishes in the front-to-back orientation: (a) longitudinal displacement, (b) transverse displacement, (c) longitudinal acceleration, (d) transverse acceleration, (e) rotation, and (f) acceleration versus displacement.

The total acceleration at the centroid of each cabinet is calculated as follows:

$$\boldsymbol{a}_j^{\mathrm{t}}(t) = \ddot{\boldsymbol{u}}_g(t) + \ddot{\boldsymbol{u}}(t) + \ddot{\theta}(t)\mathbf{R}'_{\theta(t)}\boldsymbol{\xi}_j + \dot{\theta}^2(t)\mathbf{R}''_{\theta(t)}\boldsymbol{\xi}_j, \quad (j = 1, \ldots, N) \tag{5.6}$$

where $\boldsymbol{\xi}_j$ is the X_{t}–Y_{t} position of the jth cabinet's centroid. The largest peak total acceleration experienced by any of the cabinets is given by

$$a_{\max}^{\mathrm{t}} = \max_{j\in\{1,\ldots,N\}} \max_{t} \left\| \boldsymbol{a}_j^{\mathrm{t}}(t) \right\| \tag{5.7}$$

The allowable limit on $a_{\max}^{\mathrm{t}}$ is taken to be $0.3g$, which if exceeded constitutes a failure of the isolation system to perform adequately.

Even though the bowl parameterization [Equation (4.13)] effectively governs the

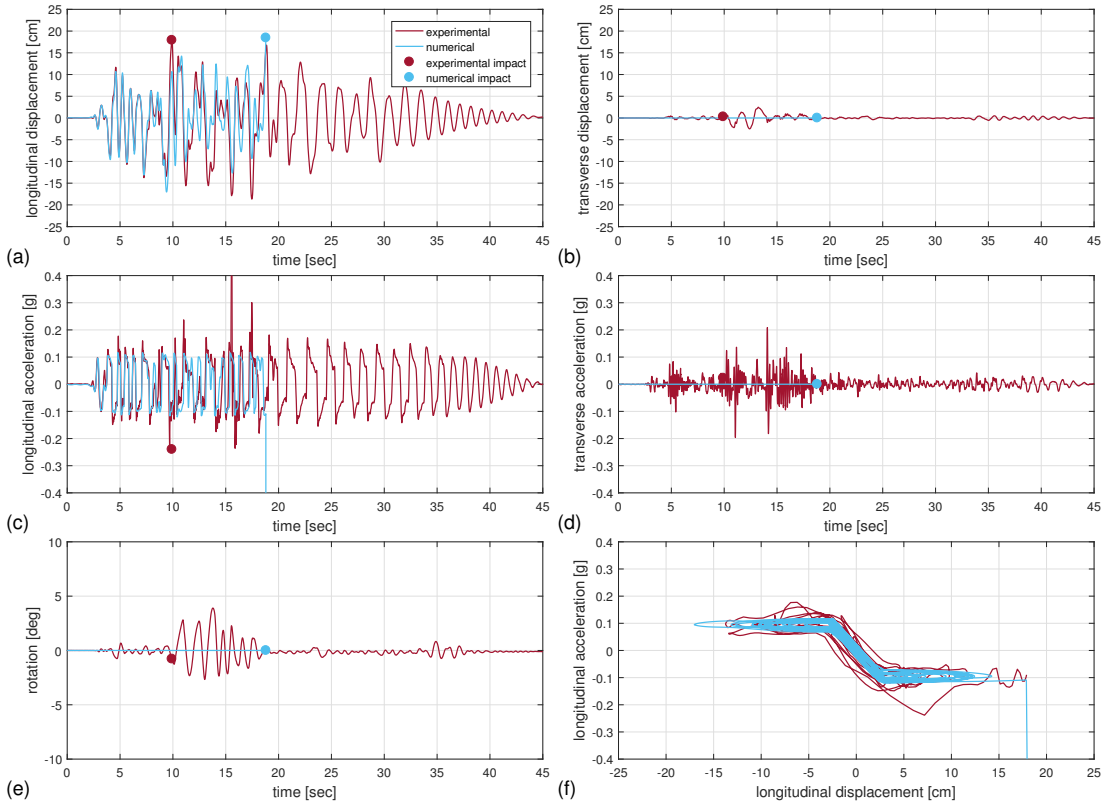

Figure 5.4: Experimental and numerical forced response results for ganged cabinets with bare steel dishes in the front-to-back orientation: (a) longitudinal displacement, (b) transverse displacement, (c) longitudinal acceleration, (d) transverse acceleration, (e) rotation, and (f) acceleration versus displacement.

accelerations sustained by the equipment, RISs are prone to failure because of excessive relative displacements resulting in impacts with the bowl lip resulting in acceleration spikes (Harvey, 2015). While this limit state will be captured by the response quantity $a^{\mathrm{t}}_{\mathrm{max}}$, the relative displacement across the bearings also serves as a response quantity of interest. The largest peak relative bearing deflection is given by

$$d_{\mathrm{max}} = \max_{i \in \{1,\ldots,n\}} \max_{t} \left\| \boldsymbol{p}_i(t) \right\| \tag{5.8}$$

The allowable limit on d_{max} is taken to be 18 cm (2× the bowl radius), beyond which an impact occurs degrading the system's performance.

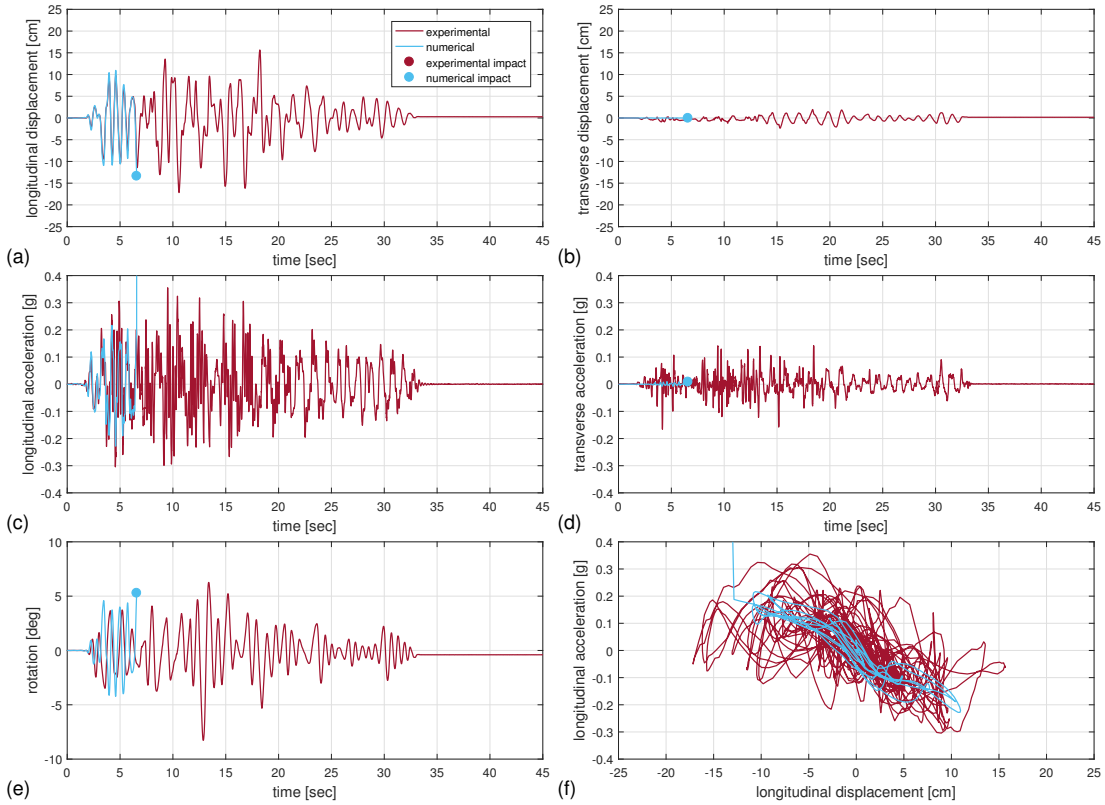

Figure 5.5: Experimental and numerical forced response results for single cabinet with bare steel dishes in the side-to-side orientation: (a) longitudinal displacement, (b) transverse displacement, (c) longitudinal acceleration, (d) transverse acceleration, (e) rotation, and (f) acceleration versus displacement.

5.5.3 Parametric Study

A parametric study, varying the ground motion scaling, number of cabinets, eccentricity, and ground motion direction, was performed. The ground motion utilized was VERTEQ-II waveform and the motions were scaled from 0 to 100% at increments of 5%. Single ($N = 1$) and ganged ($N = 2$, 4, and 8) cabinet configurations were considered. The mass eccentricity was varied from 0 to 36 cm at increments of 12 cm. Finally, two loading directions were used: 0° (front-to-back) and 90° (side-to-side). The simulations were preformed in Matlab and the total number of trials was 640. The peak response values from the displacement time histories, acceleration time histories, and rotation time histories were obtained for each parametric combination, and the results

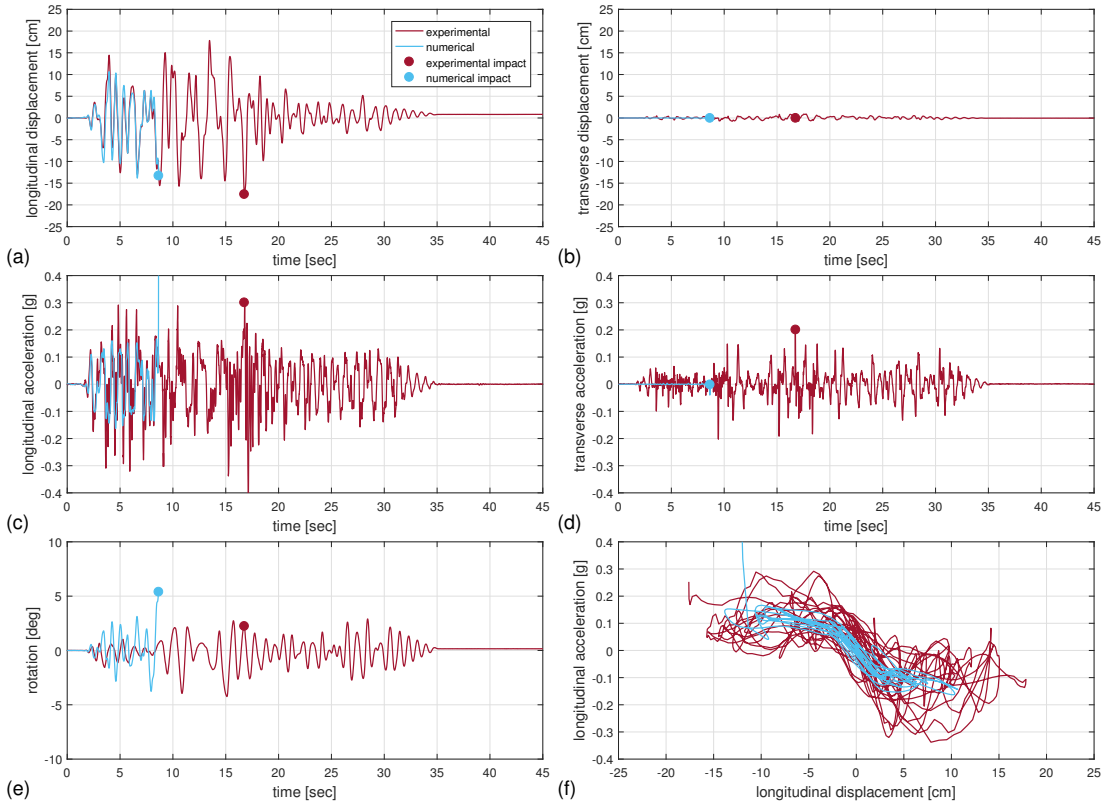

Figure 5.6: Experimental and numerical forced response results for ganged cabinets with bare steel dishes in the side-to-side orientation: (a) longitudinal displacement, (b) transverse displacement, (c) longitudinal acceleration, (d) transverse acceleration, (e) rotation, and (f) acceleration versus displacement.

are plotted to assess the sensitivity of the system behavior to each parameter.

Figures 5.7, 5.8, 5.9, and 5.10 show the peak response values for the systems subject to ground motion in the side-to-side orientation. Figure 5.7 shows the results when no mass eccentricity exists in the system setup, which is identical to the case of loading in the front-to-back orientation due to the location of the center of mass (i.e., along the centerline of the cabinet); therefore, the results for the front-to-back orientation are not shown. The results show a "break point" in the plots for each system configuration at which point impact occurred and displacements were stunted, accelerations spiked, and rotations maxed out. The plots are color coded with red indicating the maximum displacement capacity of 18 cm was reached and impacts with the bearing lip/edge

occurred, yellow indicating the acceleration limit of $0.3g$ was reached, and white indicating the system would remain operational.

Figures 5.7, 5.8, 5.9, and 5.10 show peak bearing displacements beyond the theoretical limit of 18 cm. The numerical model predicts these large displacements for the cases in which impacts occur. As previously discussed, the numerical model does not explicitly model impacts, but instead a very stiff region is included in the assumed bowl profile [Equation (4.13)] to simulate impacts. While the predicted excessive displacements are not observed in experimental bearings at impact, these displacements may be interpreted as body deformations in the isolated cabinet or rocking of the cabinet. For an experimental case, upon impact of the balls with the bearing lip/edge, energy transitions from the horizontal motion of the rolling bearing into strain energy through the high inertial load acting through the deflection of the cabinet. This transition of energy pulls energy away from the fundamental mode of horizontal motion through the bearing displacement and distributes it along the cabinet height. Additionally the high inertial load of the system at a distance h from the top of the platform causes tipping, resulting in larger displacements at the top of the cabinet. Therefore, these large displacements predicted by the model can be thought of as the total displacement of the top of the cabinet relative to the ground as opposed to just the displacement across the bearing. With that said, the quantitative accuracy of these predications are suspect, but may be improved through a fitting of the secondary slope s_1 in the bowl geometry [Equation (4.13)].

5.6 Discussion of Numerical Results

5.6.1 Bearing Displacement Response

The peak bearing displacement responses were captured for numerical simulations performed over a parameter space of ground motion scaling, number of cabinets, mass

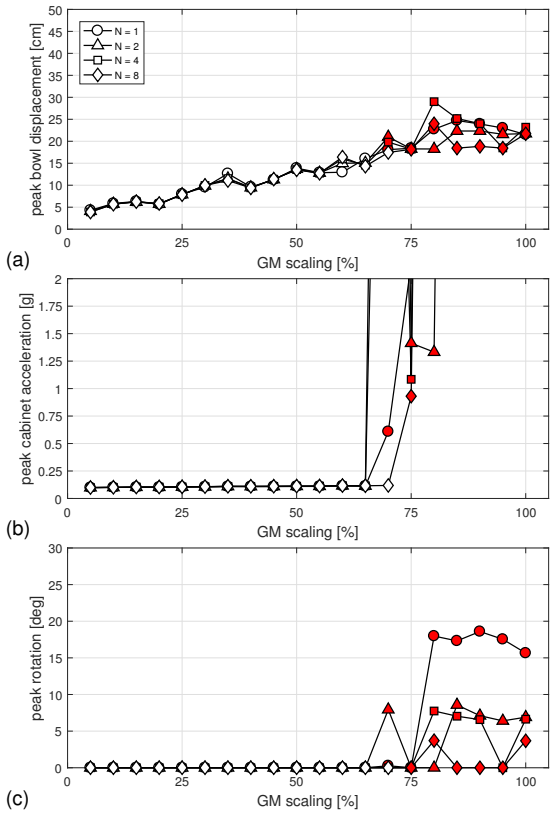

Figure 5.7: Peak responses for numerical forced excitation for 0 cm eccentricity in the side-to-side orientation: (a) bearing displacement, (b) cabinet acceleration, and (c) system rotation.

eccentricity, and direction of loading. Figures 5.7(a), 5.8(a), 5.9(a), and 5.10(a) shows linear trends with an increase in peak displacement with an increase in ground motion scaling up until 18 cm at which point impacts occurred and the peak ground motion was "stunted". Local minimum and maximum are seen in trend which can be attributed to the nonlinearities in the system.

The peak bearing displacement responses for the front-to-back direction (not shown) exhibit no correlation with the number of cabinets up until the point of impact. This is expected because both the inertial forces and restoring forces increase linearly with mass, and there is no eccentricity in the front-to-back direction. However, for side-to-side orientation the number of cabinets has an effect when an eccentricity is present. Higher peak displacements are seen for lower number of cabinets than for higher num-

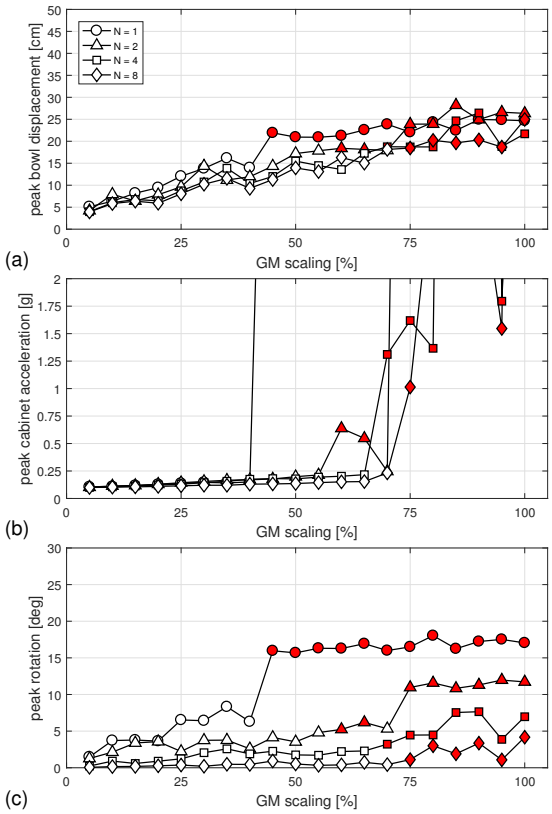

Figure 5.8: Peak responses for numerical forced excitation for 12 cm eccentricity in the side-to-side orientation: (a) bearing displacement, (b) cabinet acceleration, and (c) system rotation.

ber of cabinet for all ground motion scalings. Peak bearing displacements are largely effected by the amount of rotation in the global system. Configurations with more cabinets resist rotations more than those with fewer cabinets due to an increase in the mass moment of inertia and larger moment arm for the restoring forces.

The peak bearing displacements are highly sensitive to the level of eccentricity within the cabinets. With a high level of eccentricity the peak displacement is reached at low levels of ground motion scaling. Trials with higher number of cabinets show more resistance to the peak displacement with high values of eccentricity, but still eventually produce high displacements with higher levels of ground motion scaling.

The direction of loading has significant effects on the response of the system due to the eccentricity within a system. Trials with no eccentricity show the exact same

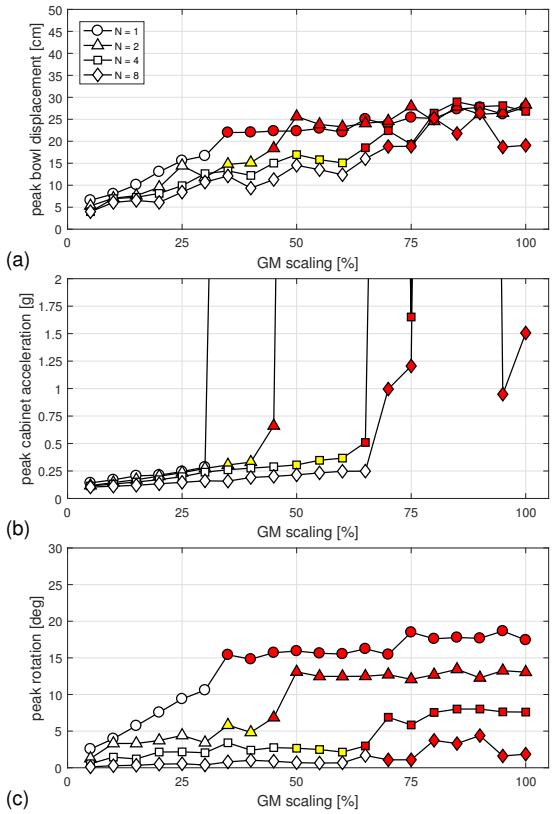

Figure 5.9: Peak responses for numerical forced excitation for 24 cm eccentricity in the side-to-side orientation: (a) bearing displacement, (b) cabinet acceleration, and (c) system rotation.

response independent of the loading direction. As the eccentricity increases, the peak displacement response increases when the system is loaded side-to-side.

5.6.2 Equipment Acceleration Response

The peak cabinet acceleration responses were also captured for the numerical simulations performed over a parameter space of ground motion scaling, number of cabinets, mass eccentricity, and direction of loading. Figures 5.7(b), 5.8(b), 5.9(b), and 5.10(b) show the peak cabinet acceleration for each setup. For the front-to-back orientation the ground motion scaling caused no increase in the peak acceleration due to the constant slope of the rolling bearing. A "breaking point" is reached at approximately 70% ground motion scaling when the peak displacements reach the maximum of 18 cm causing impact with the bearing edge causing excessive spikes in acceleration. For the side-to-side

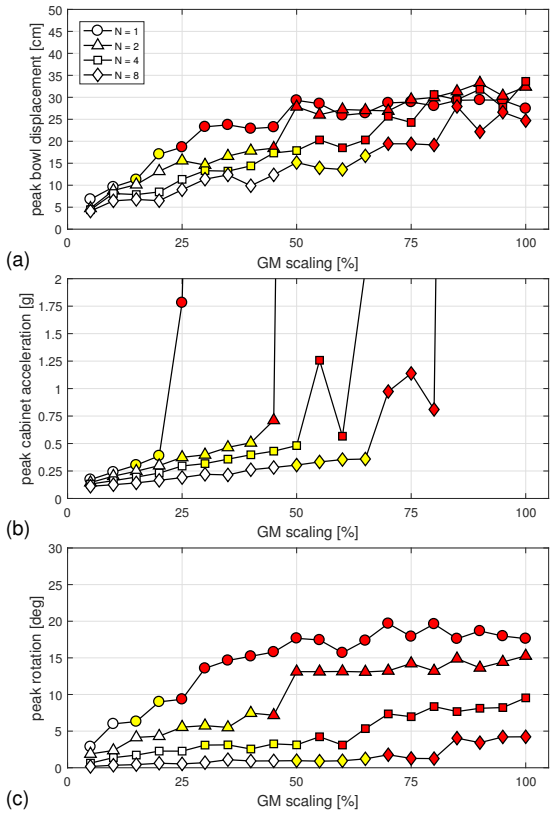

Figure 5.10: Peak responses for numerical forced excitation for 36 cm eccentricity in the side-to-side orientation: (a) bearing displacement, (b) cabinet acceleration, and (c) system rotation.

orientation, increases in the ground motion scaling cause linear increases in the peak acceleration due to the mass eccentricity in the system which creates rotations in the global system and therefore radial and tangential accelerations at the centroids of the cabinets. The "breaking points" for different number of cabinets in the side-to-side orientation also occur at different ground motion scales.

The number of cabinets has little effect on the peak acceleration responses in the front-to-back orientation. The ganged setup with eight cabinets ($N = 8$) does not hit the breaking point until 75% versus the other cabinet setups which occur at 70%. Higher number of cabinets shows more resistance to accelerations at set ground motions due to higher moments inertia and therefore lower rotational accelerations of which the components are the radial and transverse acceleration of the centroids of the cabinets.

5.6.3 System Rotation Response

The peak system rotation responses over the parameter space were also captured. Figures 5.7(c), 5.8(c), 5.9(c), and 5.10(c) show the peak system rotation for each setup. Cases with eccentricity show an increase in the rotation up until the point of impact at which point the maximum value for rotation is achieved. For single ($N = 1$) and ganged ($N = 2$, 4, and 8) cabinet setups the maximum possible rotations are 19.80°, 7.69°, 3.86°, and 1.93°, respectively. The numerical results show rotations increasing approximately linearly up until the point of impact. For some cases, the rotations jump up to the maximum value for which the rotations had less influence on the displacement across the bearings. The elastic impact produced high restoring forces which induced large rotations. For other cases, the rotations are stunted at the maximum possible value, for which the rotations were more responsible for the displacement across the bearings. The elastic impact still produced high restoring forces, but the peak rotations were already being achieved.

5.6.4 Performance Curves

Isolation of typical building contents and nonstructural components would ideally be designed using basic charts for determining performance. From the incremental dynamic analysis results (Figures 5.7 – 5.10), there is a distinct ground motion scaling at which isolation performance is degraded (i.e., the "breaking point" where impacts are observed). Figure 5.11 shows *performance curves* based on number of cabinets and eccentricity. The curves show the limiting ground motion scaling for which the system configurations meet the displacement capacity criteria. Figure 5.11(a) shows increasing performance with increasing number of cabinets for a constant value of eccentricity. Figure 5.11(b) shows decreasing performance with increasing eccentricity for a constant number of cabinets. The sensitivity of this trend decreases with increasing number

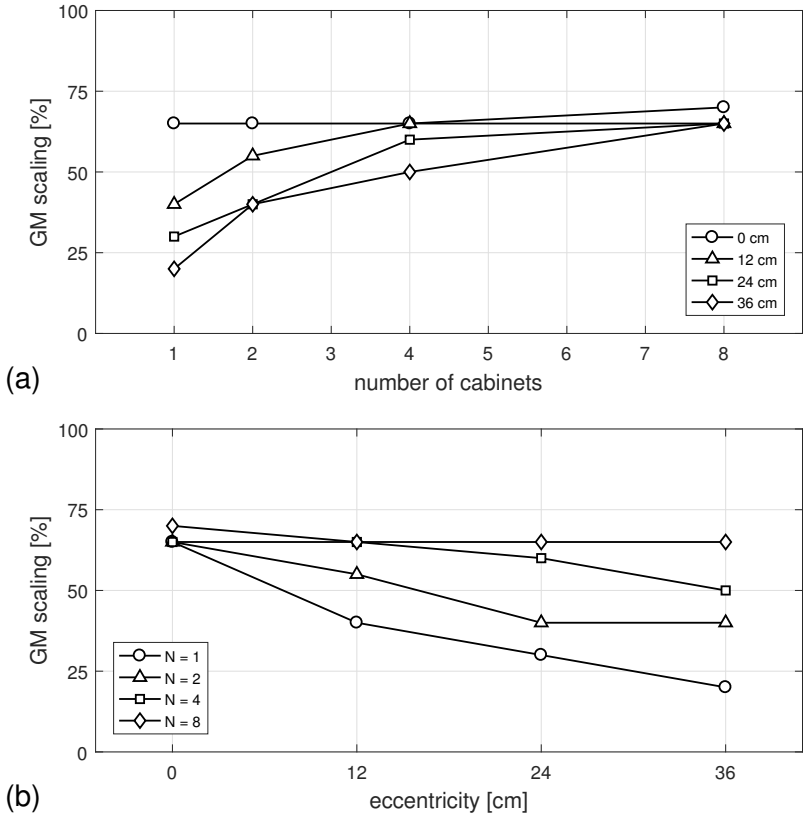

Figure 5.11: Performance curves showing the largest ground motion (GM) scaling without experiencing an impact for a lightly-damped RIS for varying eccentricity and number of cabinets: (a) constant lines for eccentricity, and (b) constant lines for number of cabinets.

of cabinets. A designer could use these curves to establish the required configuration (number of cabinets and eccentricity) for a given ground motion intensity.

5.7 Summary

The mathematical model derived in Chapter 4 was used to predict the time histories and peak responses for a rolling isolation platform with N cabinets. The model was calibrated using a single ($N = 1$) and ganged ($N = 2$) cabinet setups to experimental free response tests in the front-to-back orientation which used a 15 cm impulse from the shake table to induce the response. The model was then validated against experimental forced response tests in both the front-to-back orientation and the side-to-side orienta-

tion using the VERTEQ-II Zone-4 waveform at 100% scaling. The numerical results show good agreement with the experimental tests, predicting the peak responses accurately up until the point of impact, which is one of the failing criteria for such systems. The calibrated model was then used to explore the parameter space of ground motion scaling, number of cabinets, mass eccentricity, and loading direction. Ground motions were scaled from 0 to 100% by increments of 5%. The cabinet setups used 1, 2, 4, and 8 cabinets. The eccentricity was varied from 0 to 36 cm at increments of 12 cm. Finally, two different loading directions were used: front-to-back and side-to-side.

The results show that the number of cabinets do not influence the maximum displacements and accelerations of the system. The peak results for the longitudinal direction show that the acceleration response is also nearly independent of the number of cabinets used in the simulation and depends almost entirely on the ground motion scaling. The accelerations drastically increase at ground motion scaling of 75% which indicates the point at which impacts occurred for the system.

Chapter 6

Summary, Conclusions, and Future Work

6.1 Summary and Conclusions

Earthquakes throughout history have produced devastating results with loss of life, damage to critical facilities, and economic damage. A growing concern in seismic mitigation is that of nonstructural components. Case studies have shown the enormous risk that building contents and nonstructural components pose to the resilience of critical facilities and communication centers. A promising approach to protect such components is that of isolation. Rolling-type isolation systems (RISs) have the advantage of providing isolation in orthogonal directions without the need of complex components and are easy implement with their low profile.

An experimental case study for a RIS which consisted of top and bottom platforms that are decoupled from each other through rolling bearings was presented. The test configurations were designed to simulate realistic operating conditions, including actual computer server cabinets with eccentric mass distributions, loading in two directions, and two rolling surface treatments (bare steel and supplementally damped dishes). The various system setups were subjected to free response tests using an abrupt shake table displacement (pulse) as well as forced response tests using the VERTEQ-II synthesized waveform for the seismic input motion. An array of sensors was deployed in order to capture the response of the configurations.

The results show increased rotational response for heavily damped systems when mass eccentricity is present with respect to the loading directions, but not for the lightly damped systems as rotational response remains consistent for such systems. The study also showed that supplemental damping decreases the overall displacement demand of the system but increases the accelerations slightly. Finally, durability issues were seen with the lightly damped systems due to high contact stresses which caused yielding of the rolling surfaces creating ruts which altered the bearing trajectories. The durability in the supplementally damped systems showed repeatable performance even after excessive testing.

Mathematical models have previously been developed to predict the behavior of single rolling platforms with concentric mass. The models were extended to include any number of isolated masses and includes eccentricities. The analytical model was derived using the kinematics of the top platform with respect to the bottom through the interaction of the balls with the rolling surfaces. The kinetic energy of the system was found using the translational velocities in the orthogonal directions as well as the rotational velocity. The potential energy of the system was derived using the change in relative displacement between the upper and lower platforms through the shape of rolling surfaces. Using Lagrange's equation, the equations of motion were found.

The analytical model was calibrated to experimental free response tests. The model was then validated using experimental forced response tests; the results showed good agreement. A numerical parametric parametric study was performed varying the eccentricity, number of cabinets, ground motion scaling, and loading direction. The peak responses for the accelerations and displacements were found and compared to set performance criteria in order to determine validity of configuration. First, the systems with seismic excitation in the front-to-back orientation show the exact same results as that of the side-to-side orientation with no mass eccentricity. For the systems with seismic

excitation in the side-to-side orientation, the results show the "break point" decreasing with respect to ground motion scaling with increase in eccentricity. The results also show increasing rotational response with increase in mass eccentricity. Further, the results show the "break point" increasing with respect to ground motion scaling with increase in the number of cabinets. Finally, the results show decreasing rotational response with increase in number of cabinets. Performance curves were formulated to show the limit based on performance criteria with respect to eccentricity, number of cabinets, and ground motion scaling.

6.2 Future Work

This thesis outlined experimental and numerical tests that characterized and modeled the rolling dynamics of RISs. In all cases, the isolation system used was only as large as needed for the objects (computer network cabinets) to be isolated. Despite the promising results of such methods of isolation, modeling of systems with isolation platforms of various size and location of objects (i.e., isolated floor systems) would allow better prediction of placement for optimization of performance of large scale network centers.

Research on RISs has primarily looked at supplemental damping through even application on the entire rolling surfaces. Damping applied in this manner varies only through velocity of the rolling device and is independent of the location. A method of patterned damping through varying application over the rolling surface could provide better performance over various ranges of excitation.

The numerical model showed good results for the prediction of the displacement, acceleration, and rotations of a system considering ground motion scale, number of cabinets, eccentricity, and loading direction. The model could predict the point at which impact occurred. However, after impact occurred, the model broke down due to high restoring forces that acted elastically with no energy absorption through the impacting

mechanism. Future work should look at modeling of the impact in order to achieve accurate results from the model both pre- and post-impact. The ability of a model to capture such results would allow for reliability models for equipment and components that rest on RISs to be evaluated for performance of excessively high seismic events and repeat events such as aftershock and high fault zones.

Bibliography

C. Alhan, F. Sahin, Protecting vibration-sensitive contents: An investigation of floor accelerations in seismically isolated buildings, Bulletin of Earthquake Engineering 9 (4) (2011) 1203–1226, doi:10.1007/s10518-010-9236-0.

F. Arima, H. Tanaka, N. Takase, H. Egasira, R. Nakamura, Development of three-dimensional isolated floor systems, Technical Rep. of Sumitomo Construction .

ASCE, ASCE 7-10 Minimum Design Loads for Buildings and Other Structures, American Society of Civil Engineers, Reston, VA, 2010.

J. F. J. Bakker, Balance Block For Buildings, US Patents No 2,014,643, 1933.

B. R. W. Boulanger, C. J. Curras, S. Member, B. L. Kutter, D. W. Wilson, A. Member, A. Abghari, Seismic soil-pile-structure interaction experiments and analysis, Journal of Geotechnical and Geoenvironmental Engineering 125 (9) (1999) 750–759.

I. Caliò, M. Marletta, F. Vinciprova, Seismic response of multi-storey buildings base-isolated by friction devices with restoring properties, Computers and Structures 81 (28-29) (2003) 2589–2599, doi:10.1016/S0045-7949(03)00327-4.

S. E. Chang, Disasters and transport systems: Loss, recovery and competition at the Port of Kobe after the 1995 earthquake, Journal of Transport Geography 8 (1) (2000) 53–65, doi:10.1016/S0966-6923(99)00023-X.

A. K. Chopra, Dynamics of Structures: Theory and Applications to Earthquake Engineering, Prentice Hall, Englewood Cliffs, New Jersey, 4th edn., 2012.

G. P. Cimellaro, A. M. Reinhorn, M. Bruneau, Seismic resilience of a hospital system, Structure and Infrastructure Engineering 6 (1-2) (2010) 127–144, doi:10.1080/15732470802663847.

S. Cui, M. Bruneau, A. Kasalanati, Behavior of bidirectional spring unit in isolated floor systems, Journal of Structural Engineering 136 (8) (2010) 944–952, doi:10.1061/(ASCE)ST.1943-541X.0000187.

S. Cui, M. Bruneau, A. Kasalanati, Seismic Response Case Study of Isolated Floor System Having Special Biaxial Spring Units, Journal of Structural Engineering 3 (12) (2016) 05016002, doi:10.1061/(ASCE)ST.1943-541X.0001596.

European Committee for Standardization, Eurocode 8: Design of structures for earthquake resistance, British Standards, 2004.

FEMA, HAZUS MH Estimated Annualized Earthquake Losses for the United States, Tech. Rep. 366, Federal Emergency Management Agency, Washington, D.C., 2008.

A. Filiatrault, T. Sullivan, Performance-based seismic design of nonstructural building components: The next frontier of earthquake engineering, Earthquake Engineering and Engineering Vibration 13 (1) (2014) 17–46, doi:10.1007/s11803-014-0238-9.

A. Fiore, G. C. Marano, M. G. Natale, Theoretical prediction of the dynamic behavior of rolling-ball rubber-layer isolation systems, Structural Control and Health Monitoring 23 (2016) 1150–1167, doi:10.1002/stc.1830.

D. Foti, A. Catalan Goni, S. Vacca, On the dynamic response of rolling base isolation systems, Structural Control and Health Monitoring 20 (2013) 639–648, doi:10.1002/stc.1538.

S. Furukawa, E. Sato, Y. Shi, T. C. Becker, M. Nakashima, Full-scale shaking table test of a base-isolated medical facility subjected to vertical motions, Earthquake Engineering and Structural Dynamics 42 (2013) 1931–1949, doi:10.1002/eqe.2305.

H. P. Gavin, A. Zaicenco, Performance and reliability of semi-active equipment isolation, Journal of Sound and Vibration 306 (1-2) (2007) 74–90, doi:10.1016/j.jsv.2007.05.039.

D. T. Greenwood, Advanced Dynamics, Cambridge University Press, Cambridge, United Kingdom, 2006.

P. S. Harvey, Jr., Vertical accelerations in rolling isolation systems: Experiments and simulations, Journal of Engineering Mechanics (2015) 04015091doi:10.1061/(ASCE)EM.1943-7889.0001017.

P. S. Harvey, Jr., H. P. Gavin, The nonholonomic and chaotic nature of a rolling isolation system, Journal of Sound and Vibration 332 (2013) 3535–3551, doi:10.1016/j.jsv.2013.01.036.

P. S. Harvey, Jr., H. P. Gavin, Double rolling isolation systems: A mathematical model and experimental validation, International Journal of Non-Linear Mechanics 61 (2014) 80–92, doi:10.1016/j.ijnonlinmec.2014.01.011.

P. S. Harvey, Jr., K. C. Kelly, A review of rolling-type seismic isolation: Historical development and future directions, Engineering Structures 125 (2016) 521–531, doi:10.1016/j.engstruct.2016.07.031.

P. S. Harvey, Jr., G.-P. Zéhil, H. P. Gavin, Experimental validation of simplified models for rolling isolation systems, Earthquake Engineering and Structural Dynamics 43 (2014) 1067–1088, doi:10.1002/eqe.2387.

W. P. Irwin, I. Barnes, Effect of geologic structure and metamorphic fluids on seismic behavior of the San Andreas fault system in central and northern California, Geology 3 (12) (1975) 713–716, doi:10.1130/0091-7613(1975)3⟨713:EOGSAM⟩2.0.CO;2.

W. D. Iwan, The earthquake design and analysis of equipment isolation systems, Earthquake Engineering and Structural Dynamics 6 (1978) 523–534, doi:10.1002/eqe.4290060602.

R. S. Jangid, Y. B. Londhe, Effectiveness of elliptical rolling rods for base isolation, Journal of Structural Engineering 124 (4) (1998) 469–472, doi:10.1061/(ASCE)0733-9445(1998)124:4(469).

P. C. Jennings, G. W. Housner, The San Fernando, California, Earthquake of February 9, 1971, in: Proceedings of the Fifth. Rome: World Conference on Earthquake Engineering, 1973.

G. Jia, I. Gidaris, A. A. Taflanidis, G. P. Mavroeidis, Reliability-based assessment/design of floor isolation systems, Engineering Structures 78 (2014) 41–56, doi:10.1016/j.engstruct.2014.07.031.

M. Kaneko, Y. Yasui, Y. Okuda, Simultaneous horizontal and vertical vibration tests of three-dimensional floor isolation systems, AIJ Journal of Technology and Design 1 (1995) 186–190, doi:10.3130/aijt.1.186.

J. M. Kelly, Earthquake-Resistant Design with Rubber, Springer-Verlag London Limited, London, United Kingdom, doi:10.1007/978-1-4471-0971-6, 1997.

Z. A. Kemeny, Ball-In-Cone Seismic Isolation Bearing, US Patents No 5,599,106, 1997.

H. Khechfe, M. Noori, Z. Hou, J. M. Kelly, G. Ahmadi, An experimental study on the seismic response of base-isolated secondary systems, Journal of Pressure Vessel Technology-Transactions of the ASME 124 (1) (2002) 81–88, doi:10.1115/1.1445795.

V. Lambrou, M. C. Constantinou, Study of seismic isolation systems for computer floors, Tech. Rep. NCEER-94-0020, National Center for Earthquake Engineering Research, Buffalo, New York, 1994.

F. Légeron, P. Paultre, J. Mazars, Damage mechanics modeling of nonlinear seismic behavior of concrete structures, Journal of Structural Engineering 131 (2005) 946–955, doi:10.1061/(ASCE)0733-9445(2005)131:6(946).

B. C. Lin, I. G. Tadjbakhsh, A. S. Papageorgiou, G. Ahmadi, Performance of Earthquake Isolation Systems, Journal of Engineering Mechanics 116 (2) (1990) 446–461, doi:10.1061/(ASCE)0733-9399(1990)116:2(446).

S. Liu, G. P. Warn, Seismic performance and sensitivity of floor isolation systems in steel plate shear wall structures, Engineering Structures 42 (2012) 115–126, doi: 10.1016/j.engstruct.2012.04.015.

L. Y. Lu, T. Y. Lee, S. Y. Juang, S. W. Yeh, Polynomial friction pendulum isolators (PFPIs) for building floor isolation: An experimental and theoretical study, Engineering Structures 56 (2013) 970–982, doi:10.1016/j.engstruct.2013.06.016.

W. E. McKevitt, P. A. M. Timler, K. K. Lo, Nonstructural damage from the Northridge earthquake, Canadian Journal of Civil Engineering 22 (2) (1995) 428–437, doi:10. 1139/l95-051.

P. A. Merriman, M. S. Williams, The magnitude 6.7 Northridge, California, earthquake of 17 January 1994, Science 266 (5184) (1994) 389–397, doi:10.1126/science.266. 5184.389.

F. Nikfar, D. Konstantinidis, Shake table investigation on the seismic performance of hospital equipment supported on wheels/casters, Earthquake Engineering and Structural Dynamics 46 (2) (2017) 243–266, doi:10.1002/eqe.2789.

B. D. Notohardjono, J. Wilcoski, J. B. Gambill, Design of earthquake resistant server computer structures, Journal of Pressure Vessel Technology-Transactions of the Asme 126 (1) (2004) 66–74, doi:10.1115/1.1638389.

A. L. K. Penkuhn, Three Point Foundation for Building Structures, US Patents No 3,347,002, 1967.

X. Qiu, Full Two-Dimensional Model for Rolling Resistance: Hard Cylinder on Viscoelastic Foundation of Finite Thickness, Journal of Engineering Mechanics 132 (11) (2006) 1241–1251, doi:10.1061/(ASCE)0733-9399(2006)132:11(1241).

F. Schär, Foundation for Buildings, US Patents No 951028, 1910.

P. Seiler, Foundation for Buildings, US Patents No 846249, 1907.

Y. Shi, M. Kurata, M. Nakashima, Disorder and damage of base-isolated medical facilities when subjected to near-fault and long-period ground motions, Earthquake Engineering and Structural Dynamics 43 (3) (2014) 1683–1701, doi:10.1002/eqe.2417.

M. P. Singh, L. M. Moreschi, L. E. Suarez, E. E. Matheu, Seismic design forces. I: Rigid nonstructural components, Journal of Structural Engineering 132(10) (2006a) 1524–1532, doi:10.1061/(ASCE)0733-9445(2006)132:10(1524).

M. P. Singh, L. M. Moreschi, L. E. Suárez, E. E. Matheu, Seismic Design Forces. II: Flexible Nonstructural Components, Journal of Structural Engineering 132 (10) (2006b) 1533–1542, doi:10.1061/(ASCE)0733-9445(2006)132:10(1533).

M. D. Symans, W. F. Cofer, K. J. Fridley, Base isolation and supplemental damping systems for seismic protection of wood structures: Literature review, Earthquake Spectra 18 (3) (2002) 549–572, doi:10.1193/1.1503342.

Telcordia Technologies (Ed.), Network Equipment-Building System NEBS Requirements: Physical Protection, GR-63-CORE, Piscataway, NJ, 2012.

A. Tena-Colunga, D. Abrams, Seismic behavior of structures with flexible diaphragms, Journal of Structural Engineering 122 (4) (1996) 439–445, doi:10.1061/(ASCE) 0733-9445(1996)122:4(439).

J. Touaillon, Improvement In Buildings, US Patents No 99973, 1870.

C.-S. Tsai, Advanced Base Isolation Systems for Light Weight Equipments, Earthquake-Resistant Structures - Design, Assessment and Rehabilitation, InTech, 2012.

C. S. Tsai, Seismic Isolation Devices: History and Recent Developments, in: ASME 2015 Pressure Vessels and Piping Conference, Boston, Massachusetts, USA, 2015.

C. S. Tsai, Y. C. Lin, W. S. Chen, H. C. Su, Tri-directional shaking table tests of vibration sensitive equipment with static dynamics interchangeable-ball pendulum system, Earthquake Engineering and Engineering Vibration 9 (1) (2010) 103–112, doi: 10.1007/s11803-010-9009-4.

R. Vargas, M. Bruneau, Experimental Response of Buildings Designed with Metallic Structural Fuses. II, Journal of Structural Engineering 135 (4) (2009) 394–403, doi: 10.1061/ASCE0733-94452009135:4394.

G. P. Warn, K. L. Ryan, A Review of Seismic Isolation for Buildings: Historical Development and Research Needs, Buildings 2 (4) (2012) 300–325, doi:10.3390/ buildings2030300.

WorkSafe Technologies, Inc., ISO-Base platform, URL `http://www.worksafetech.com/`, 2011.

C.-Y. Yang, C.-H. Hsieh, L.-L. Chung, H.-M. Chen, L.-Y. Wu, Effectiveness of an eccentric rolling isolation system with friction damping, Journal of Vibration and Control 18 (14), doi:10.1177/1077546311428633.

V. Zayas, Earthquake protective column support, US Patent 4,644,714, 1987.

G. P. Zéhil, H. P. Gavin, Simplified approaches to viscoelastic rolling resistance, International Journal of Solids and Structures 50 (6) (2013) 853–862, doi:10.1016/j.ijsolstr. 2012.09.025.

Q. Zhou, X. Lu, Q. Wang, D. Feng, Q. Yao, Dynamic analysis on structures base-isolated by a ball system with restoring property, Earthquake Engineering and Structural Dynamics 27 (8) (1998) 773–791, doi:10.1002/(SICI)1096-9845(199808)27:8⟨773::AID-EQE749⟩3.0.CO;2-A.